

# Distance Measurements between Paramagnetic Centers by High-Field EPR Relaxation Experiments

Dissertation  
zur Erlangerung des Doktorgrades  
der Naturwissenschaften

vorgelegt beim Fachbereich  
Chemische und Pharmazeutische Wissenschaften  
der Johann Wolfgang Goethe-Universität  
in Frankfurt am Main

von  
Marloes Penning de Vries  
aus Wageningen, die Niederlande

Frankfurt am Main 2007  
D30

vom Fachbereich  
Chemische und Pharmazeutische Wissenschaften der  
Johann Wolfgang Goethe-Universität  
als Dissertation angenommen.

Dekan: Prof. Dr. H. Schwalbe

1. Gutachter: Prof. Dr. T.F. Prisner

2. Gutachter: Prof. Dr. H. Schwalbe

Datum der Disputation:

To my family

Especially to my big brother,  
who missed out on the best part



## Kurzfassung

In dieser Dissertation wird von Untersuchungen der dipolaren Kopplung mit Hilfe von G-Band (180 GHz, 6.4 T) Elektron Paramagnetischen Resonanz (EPR) Relaxationsmessungen berichtet. Die Doktorarbeit besteht aus drei Teilen.

Das Ziel des ersten Teils war die Ermittlung der Geometrie des Protein-Protein Komplexes, das von den zwei Elektronentransferpartnern Cytochrom c und Cytochrom c Oxidase (CcO) gebildet wird. Dazu wurden Mischungen von CcO mit drei verschiedenen Cytochromen für die EPR Messungen verwendet.

In dem zweiten Teil wurde das Simulationsprogramm, das zur Interpretation der dipolaren Relaxationsergebnissen angewendet wurde, getestet, in dem Messungen an Modellsystemen durchgeführt wurden. Diese Modellsysteme sind lineare Moleküle mit jeweils einem Nitroxidradikal und einem paramagnetischen Metallion ( $\text{Cu}^{2+}$ ,  $\text{Mn}^{2+}$ ).

Zuletzt werden  $T_1$  Messungen an paramagnetischen Metallionen, ebenfalls im Hochfeld, präsentiert. Diese wurden durchgeführt um zu zeigen, dass die  $T_1$  Relaxation der untersuchten Metallionen bei tiefer Temperatur stark vom Magnetfeld abhängig ist.

### K.1. Theorie

Das Messen von Abständen zwischen ungepaarten Elektronen ist ein Thema in der EPR das in den letzten Jahren wesentlich an Bedeutung gewonnen hat. Die am meisten angewandte Methode ist DEER, auch PELDOR genannt, was eine englische Abkürzung für „gepulste Elektron-Elektron Doppel Resonanz“ ist. Diese Methode wird angewandt zu der Bestimmung des Abstands zwischen zwei, oder mehreren, paramagnetischen Zentren, oft organischen (Nitroxid-) Radikalen. Eine wichtige Voraussetzung für das PELDOR Experiment ist, daß die Spektren der beteiligten Elektronenspins nicht zu breit sind, da genügend Spins angeregt werden müssen damit ein PELDOR Effekt sichtbar ist.

Für paramagnetische Zentren mit großer g-Anisotropie, wie z.B. low-spin Eisen(III), ist allerdings die dipolare Relaxationsmessung eine bessere Methode zur Abstandsbestimmung. Diese Methode beruht auf dem Prinzip daß die schnelle  $T_1$  Relaxation eines Spins (B) dazu führen kann, dass die  $T_2$  Relaxationsrate eines gekoppelten Spins (A) erhöht wird. Die Stärke dieses Effekts hängt von den folgenden Strukturparametern ab: dem Abstand  $r$  zwischen den gekoppelten Spins; den Winkeln  $\theta_D$  und  $\phi_D$  die der Vektor zwischen den Spins in bezug auf den g-Tensor des A Spins bildet; den Euler Winkeln  $\alpha$ ,  $\beta$  und  $\gamma$ , die die relative Orientierung der Spins A und B kennzeichnen (Abbildung K.1). Außerdem ist die dipolare Relaxationsrate  $1/T_2^{\text{dip}}$  abhängig von der Relaxation des B Spins,  $T_{1f}$ . Da  $T_{1f}$  stark temperaturabhängig ist, ist die dipolare Relaxation somit auch von der Temperatur abhängig.

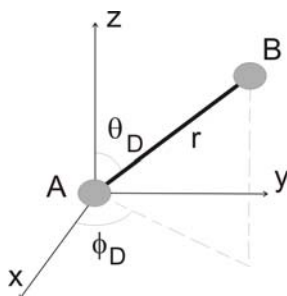
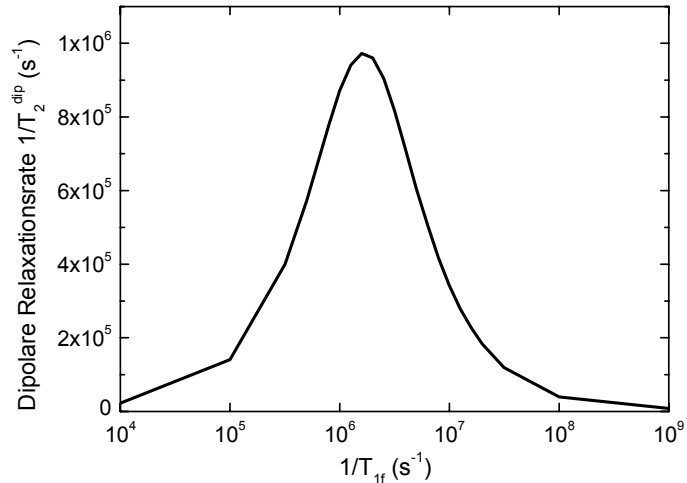


Abbildung K.1. Parameter, die wichtig für die Berechnung der dipolaren Kopplung sind. Die z-Achse des Spins A ist parallel zu dem Magnetfeld angeordnet. A und B, resonanter bzw. nicht-resonanter gekoppelter Spin;  $r$ , Abstand zwischen den beiden paramagnetischen Zentren;  $\theta_D$  und  $\phi_D$  sind die dipolaren Winkel.

Die Temperaturabhängigkeit der dipolaren Relaxationszeit ist sehr charakteristisch:  $T_2^{\text{dip}}$  nimmt zunächst mit der Temperatur ab, bis die  $T_1$  Relaxationsrate des B Spins gleich groß ist wie die dipolare Kopplung (in  $\text{rad s}^{-1}$ ). Eine weitere Abnahme des  $T_{1f}$  (durch Zunahme der Temperatur) führt zu einer Zunahme der  $T_2^{\text{dip}}$ . Die Temperaturabhängigkeit ist in Abbildung K.2 dargestellt.

Näherungen für die dipolare Relaxationszeit in den Grenzfällen sind wie folgt:  
 Für niedrige Temperatur ( $R^2 \ll 1$ ):  $T_2^{\text{dip}} = T_{1f}$   
 Für hohe Temperatur ( $R^2 \gg 1$ ):  $T_2^{\text{dip}} = 1/2 \Delta^2 T_{1f}$   
 mit  $R^2 = T_{1f}^{-2} - \Delta^2$  und  $\Delta$  als die Hälfte der dipolaren Kopplung in  $\text{rads}^{-1}$ .

Abbildung K.2. Dipolare Relaxationsraten ( $1/T_2^{\text{dip}}$ ) des Spins A, der mit einer dipolaren Kopplung von  $\Delta = 39 \text{ rads}^{-1}$  (6.2 MHz) mit einem Spin B gekoppelt ist. Bei niedriger Temperatur, wo  $1/T_{1f} \gg \Delta$ , ist  $T_2^{\text{dip}} = T_{1f}$ ; ein Maximum der dipolaren Relaxationsrate befindet sich bei  $1/T_{1f} = \Delta$ ; bei hoher Temperatur, wo  $1/T_{1f} \ll \Delta$ , gilt:  $T_2^{\text{dip}} = 2/\Delta^2 T_{1f}$ .



Bei niedriger Temperatur ist die dipolare Relaxation also unabhängig von dem genauen Wert der dipolaren Kopplung  $\Delta$ . Die dipolare Relaxation ist dann isotrop und das Signal zerfällt mono-exponentiell mit einer Zeitkonstante gleich  $T_{1f}$ . Bei hoher Temperatur hängt die dipolare Relaxation sehr stark von der dipolaren Kopplung ab und sie ist anisotrop. Das heisst, dass verschiedene Positionen im EPR Spektrum mit unterschiedlichen  $T_2^{\text{dip}}$  Zeiten relaxieren, da Spins die unterschiedlich angeordnet sind wegen der Winkelabhängigkeit des  $\Delta$  unterschiedlich starke dipolare Kopplung erfahren. An einer Position im Spektrum wo viele Spins mit unterschiedlichen Orientierungen zu dem Signal beitragen, ist die dipolare Relaxation nicht exponentiell, weil sie aus der Summe von vielen dipolaren Relaxationskurven entsteht. Wenn man diese unterschiedlichen Beiträge spektral trennen könnte, könnte man die Orientierung der zwei Spins zu einander, und die des dipolaren Vektors zu dem g-Tensor des A Spins bestimmen.

Eine bessere Auflösung des EPR Spektrums bekommt man, wenn man bei höheren Mikrowellenfrequenzen, und somit bei höheren Magnetfeldern misst. Die EPR Spektren vieler paramagnetischen Zentren können erst von Spektrometern aufgelöst werden, die eine Frequenz von mindestens 90 GHz haben. Eine gute Auflösung eines Spektrums ist die Voraussetzung für die Bestimmung der Orientierung zweier gekoppelter Spins.

## K.2. Cytochrom c und Cytochrom c Oxidase

Die Elektronentransportkette, oder Atmungskette, besteht aus fünf Proteinen: Komplex I bis Komplex V. Die Atmungskette ist der letzte Schritt des Glukose-Abbaus, und hat die Funktion einen Protonengradienten über die Membran zu bilden. Komplex IV der Atmungskette, die CcO, ist ein Protein, das die Oxidation von Cytochrom c katalysiert und die Elektronen für die Reduktion von Sauerstoff zu Wasser verwendet. Dabei transportiert die CcO Protonen durch die Membran, von der inneren zur äusseren Membranseite, und baut damit einen elektrochemischen Gradienten auf. Dieser Gradient wird von Komplex V, der ATP Synthase, für die Bildung von ATP aus ADP und Phosphat benutzt.

Cytochrom c ist ein kleines Protein dessen Funktion der Elektronentransfer ist. In der Atmungskette pendelt es zwischen den Komplexen III und IV, mit denen es jeweils einen kurzlebigen Komplex bildet, damit es zu Elektronenübertragungen kommen kann.

Die Proteine der mitochondrialen Atmungskette bestehen aus vielen Subunits und sind daher sehr groß und komplex. Die Atmungskette in aeroben Bakterien ist sehr ähnlich, allerdings sind hier die Proteine fast nur auf die für die primäre Funktion wichtigen Bestandteile beschränkt. Deshalb werden viele Studien mit bakteriellen Proteinen durchgeführt. Für diese Arbeit wurden Proteine des Bakteriums *Paracoccus denitrificans* (*P.d.*) gemessen.

Obwohl die 3D Strukturen der Proteine CcO und Cytochrom  $c_{552}$  des *P.d.* bekannt sind [Iwata et al. 1995; Reincke et al. 2001], gibt es noch viele offene Fragen, die nicht mit den bekannten Strukturen beantwortet werden können. Eine davon ist, wie der Protein-Proteinkomplex aussieht, der von Cytochrom c und CcO gebildet wird, bevor es zur Elektronenübertragung kommt. Da beide Proteine in ihrer oxidierten Form paramagnetische Zentren haben (u.a.  $Cu_A$  in CcO und  $Fe^{3+}$  in Cytochrom c), ist EPR eine geeignete Methode diese Frage zu beantworten.

Wir haben EPR dipolare Relaxationsmessungen bei hohem Magnetfeld durchgeführt, mit der Absicht den Abstand zwischen den paramagnetischen Zentren des Cytochrom c, bzw. CcO, und zusätzlich die Orientierung von Cytochrom c zu CcO zu bestimmen. Zu diesem Zweck haben wir die dipolare Relaxation von Gemischen von CcO mit verschiedenen Cytochromen, in Abhängigkeit der Temperatur studiert. Diese Experimente wurden auch mit X-Band EPR durchgeführt [Lyubenova et al.], und die Hochfeld EPR Ergebnisse wurden mit den X-Band Daten und mit Simulationen verglichen. Für die Messungen wurde nur Subunit II von *P.d.* CcO ( $CcO_{II}$ ) verwendet, weil die ganze CcO zusätzliche Metallzentren enthält, die die Interpretation der dipolaren Relaxationsmessungen erschweren würde.  $CcO_{II}$  enthält nur paramagnetisches  $Cu_A$ .

Es wurde die Relaxation des  $Cu_A$  vor und nach Zugabe von drei verschiedenen Cytochromen zu  $CcO_{II}$  gemessen (Abbildung K.3). Die reine dipolare Relaxation wurde durch Division der Relaxationskurve von  $Cu_A$  in der Mischung aus  $CcO_{II}$  und Cytochrom c durch die Relaxationskurve von  $Cu_A$  in einer Lösung mit nur  $CcO_{II}$  erhalten.

*P.d.* Cytochrom  $c_1$  ( $c_1$ ) kann keinen Elektronentransferkomplex mit  $CcO_{II}$  bilden, da die Bindungsfläche des  $c_1$  sowie die Bindungsfläche des  $CcO_{II}$  negativ geladen sind. Trotzdem wurde ein dipolarer Relaxationseffekt festgestellt. Dieser Effekt kann damit erklärt werden, dass auch sich frei in Lösung befindliche paramagnetische Teilchen einen

gewissen dipolaren Relaxationsbeitrag liefern. Der Beitrag der willkürlich verteilten Proteine ist aber wesentlich kleiner als der Beitrag eines Proteins, das einen Komplex mit  $\text{CcO}_{\text{II}}$  gebildet hat. Der durchschnittliche Abstand zwischen freien Proteinen und  $\text{CcO}_{\text{II}}$  ist viel größer als der Abstand zwischen einem gebundenen Protein und  $\text{CcO}_{\text{II}}$ .

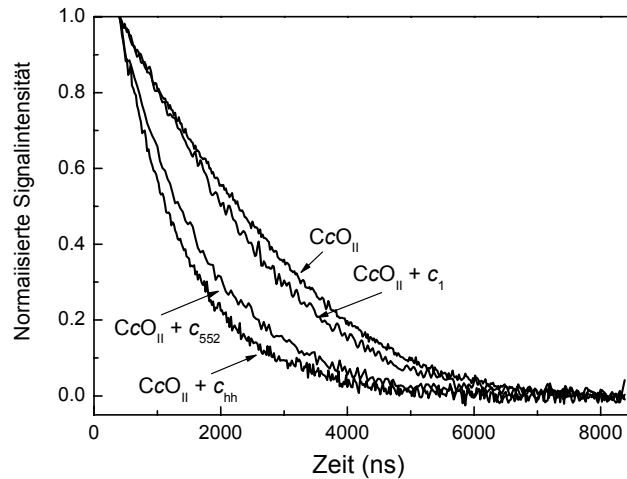


Abbildung K.3. Zerfallkurven des  $\text{Cu}_A$  Signals in  $0.2 \text{ mM CcO}_{\text{II}}$  in An- oder Abwesenheit von  $0.2 \text{ mM c}_1$ ,  $0.2 \text{ mM c}_{552}$  oder  $0.2 \text{ mM c}_{hh}$ . Temperatur:  $15 \text{ K}$ , die Messungen wurden bei G-Band Frequenz, auf dem Maximum des  $\text{Cu}_A$  Signals ( $g_{yy}$  Position) durchgeführt.

Der dipolare Relaxationseffekt, gemessen an Gemischen von  $\text{CcO}_{\text{II}}$  mit entweder *P.d.* Cytochrom  $c_{552}$  ( $c_{552}$ , natürliches Substrat zu *P.d.*  $\text{CcO}$ ) oder Cytochrom *c* isoliert aus Pferdeherzen ( $c_{hh}$ ), war viel größer als für das Gemisch mit  $c_1$ . Im Gegensatz zu  $c_1$  sind diese Cytochrome dazu fähig  $\text{CcO}_{\text{II}}$  Elektronen zu übertragen [Reincke et al. 1999], und bilden dazu Komplexe mit  $\text{CcO}_{\text{II}}$ . Für die Gemische von  $\text{CcO}_{\text{II}}$  mit  $c_{hh}$  oder  $c_{552}$  wurde eine charakteristische Temperaturabhängigkeit der dipolaren Relaxation gemessen. Um die Struktur des Komplexes aufzuklären, wurden die X-Band Messungen mit Hilfe eines Programmes, das speziell für diese Messungen im Haus geschrieben wurde angefitet. Die  $T_1$  Werte für Cytochrom *c* waren zwar für X-Band Bedingungen vorhanden [Scholes et al. 1984], aber nicht für höhere Magnetfelder bekannt. Da  $T_1$  ein sehr wichtiger Parameter in der Berechnung der dipolaren Relaxation ist, konnten die G-Band Messungen nicht angefitet werden.

Die X-Band Daten konnten mit verschiedenen Parametersätzen angefitet werden. Die Parameter aus den X-Band Fits wurden deswegen für Simulationen der G-Band Ergebnisse eingesetzt. Keiner der Parametersätze aus den X-Band Fits hat mit den experimentellen G-Band Ergebnissen übereingestimmt: wo bei den Simulationen in allen Fällen Relaxationsanisotropie zu sehen war, wurde experimentell keine Anisotropie festgestellt. Daraus folgt, dass der Protein-Protein Komplex nicht in einer festen Geometrie vorliegt, sondern dass mehrere Konformationen möglich sind.

Als Annäherung an eine solche Situation wurden die X-Band Fits anschließend mit zwei Parametersätzen wiederholt, die jeweils eine Komplexgeometrie darstellen. Die X-Band Daten konnten mit diesem stark vereinfachten zwei-Geometrien-Modell gut simuliert werden. Die Relaxationsanisotropie in dem Modell war auch wesentlich kleiner und dadurch in höherer Übereinstimmung mit den Hochfelddaten.

Aus den experimentellen X-Band und G-Band Ergebnissen und den Simulationen wurde die Schlussfolgerung gezogen, daß der Protein-Protein Komplex, der von  $c_{hh}$  und von  $c_{552}$  mit  $\text{CcO}_{\text{II}}$  gebildet wird, keine einzigartige Geometrie hat, sondern daß sich viele verschiedene Komplexe bilden. Eine Erklärung für dieses Verhalten findet man in den

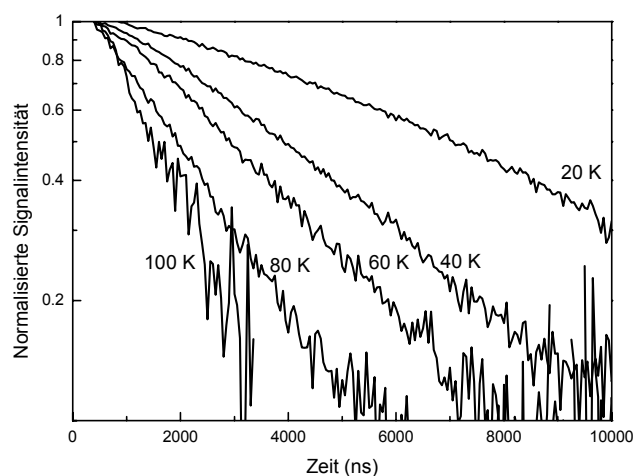


verschiedenen Bindungsmodellen, die für Elektronentransferproteine entwickelt wurden. Erstens das Zweischnittmodell („Two-step model“): Cytochrom *c* wird von CcO durch elektrostatische Wechselwirkungen angezogen und bindet unspezifisch an CcO. In einem weiteren Schritt bewegt sich das Cytochrom ein wenig, damit es genau auf die komplementäre Bindungsfläche des CcO passt, wie ein Schlüssel in ein Schloss. Zweitens das Verteilungsmodell („Distribution model“): es kommt zunächst auch zu Anziehung durch elektrostatische Wechselwirkungen und Bildung eines unspezifischen Komplexes. In dem nächsten Schritt wird aber kein spezifischer Komplex gebildet. Das Cytochrom gleitet über die Bindungsfläche des CcO und überträgt ein Elektron wenn der Elektronendonator (die Hämgruppe des Cytochroms) dem Elektronenakzeptor ( $\text{Cu}_A$ ) nahe genug ist. Auf Grund unserer Ergebnisse kann keines von den beiden Modellen bevorzugt oder ausgeschlossen werden.

### K.3. Dipolare Relaxation in Modellsystemen

Als Test unseres Simulationsprogrammes sind Messungen an Modellsystemen durchgeführt worden. Diese Modellsysteme sind starre, stabförmige Moleküle mit einem paramagnetischen Metallion auf der einen Seite, einem Nitroxidradikal auf der anderen Seite. Die Messungen wurden jeweils mit folgenden Molekülen durchgeführt:  $\text{Cu}^{2+}$ -Orthoethylporphyrin-TPA ( $\text{Cu}^{2+}$ -NO $\cdot$ ) und  $\text{Ni}^{2+}$ -Orthoethylporphyrin-TPA ( $\text{Ni}^{2+}$ -NO $\cdot$ ) zum Vergleich;  $\text{Mn}^{2+}$ -Terpyridin-TPA ( $\text{Mn}^{2+}$ -NO $\cdot$ ) und Terpyridin-TPA (Terpy-NO $\cdot$ ) zum Vergleich.

Die Anwesenheit des  $\text{Cu}^{2+}$  ( $S = 1/2$ ) Ions verursacht dipolare Relaxation bei dem Nitroxidradikal.  $\text{Ni}^{2+}$  ( $S = 1$ ) verursacht ebenfalls dipolare Relaxation, aber weil  $\text{Ni}^{2+}$  in G-Band eine sehr hohe  $T_1$  Relaxationsrate aufweist, war bei Temperaturen über 20 K kein dipolarer Relaxationseffekt zu sehen. Die dipolare Relaxation des Nitroxids durch  $\text{Cu}^{2+}$  wurde bei Temperaturen zwischen 20 und 120 K gemessen. Die Ergebnisse sind in Abbildung K.4 gezeigt. Bei Temperaturen über 120 K war kein Signal zu sehen wegen der schnellen  $T_2$  Relaxation des Nitroxidradikals.



In dem Temperaturbereich zwischen 20 und 120 K war die  $T_1$  Relaxationsrate des  $\text{Cu}^{2+}$  kleiner als die dipolare Kopplung, was bedeutet, daß die Messungen in dem Temperaturbereich wo  $T_2^{\text{dip}} = T_{1f}$  durchgeführt wurden. Aus diesen Messungen konnten keine Strukturparameter bestimmt werden. Der dipolare Zerfall des Signals, der auf der  $g_{yy}$  Position des Nitroxidspektrums gemessen wurde, war für jede

Abbildung K.4. Temperaturabhängigkeit der dipolaren Relaxation des Nitroxidradikals in  $\text{Cu}^{2+}$ -NO $\cdot$ . Die Zerfallkurven sind auf dem Maximum des Nitroxidsignals ( $g_{yy}$  Position) gemessen. Alle dipolaren Relaxationskurven zeigen einen mono-exponentiellen Zerfall.

Temperatur mono-exponentiell, und  $T_{1f}$  konnte einfach aus den dipolaren Relaxationskurven bestimmt werden. Diese  $T_1$  Werte stimmten sehr gut überein mit  $T_1$  Werten die direkt aus Inversion Recovery (IR) Experimenten bestimmt wurden.

Die Anwesenheit von Relaxationsanisotropie wurde überprüft, obwohl diese laut Simulationen auch bei 110 K sehr klein sein müsste. Es wurde keine dipolare Anisotropie detektiert, was zum Teil an dem kleinen Signal und der intrinsischen Relaxationsanisotropie des Nitroxidradikals liegt.

Die  $T_1$  Relaxation von  $Mn^{2+}$  war sehr ähnlich. Auch für  $Mn^{2+}$ -NO $\cdot$  war für den Temperaturbereich, in dem die dipolare Relaxation direkt von der dipolaren Kopplung abhängig ist, die intrinsische  $T_2$  Relaxation des Nitroxids zu schnell. Es konnten deshalb dort keine Messungen durchgeführt werden. In dem Temperaturbereich von 60 bis 80 K konnte die dipolare Relaxation bestimmt werden. Der dipolare Zerfall des Signals war mono-exponentiell und die ermittelten  $T_1$  Werte waren denen sehr ähnlich, die für  $Cu^{2+}$  bestimmt worden sind. Auch hier konnten keine Strukturparameter ermittelt werden.

#### K.4. Magnetfeldabhängigkeit der $T_1$ Relaxation

Die  $T_1$  oder Spin-Gitter Relaxation wird bei tiefer Temperatur (im X-Band:  $T \ll 10$  K) von dem direkten Prozess verursacht: ein Phonon (gequantelte Gitterschwingung) mit einer bestimmten Energie wird von einem angeregten Spinsystem aufgenommen, wodurch der Spin in den Grundzustand zerfällt. Der direkte Prozess ist als  $1/T_1 \sim B_0^4$  vom Magnetfeld  $B_0$  abhängig [Orbach 1961]. Die Temperaturabhängigkeit des direkten Prozesses ist linear. Bei höheren Temperaturen überwiegt deswegen der Raman Prozess: ein Phonon mit einer bestimmten Energie wird von einem angeregten Spinsystem aufgenommen, wodurch das System auf ein virtuelles Energieniveau angeregt wird. Es folgt Zerfall in den Grundzustand und eine gleichzeitige Emission eines Phonons mit niedrigerer Energie als die des ersten Phonons. Der Raman Prozess hat eine Temperaturabhängigkeit von  $T^6$  bis  $T^9$ , und ist meistens magnetfeldunabhängig.

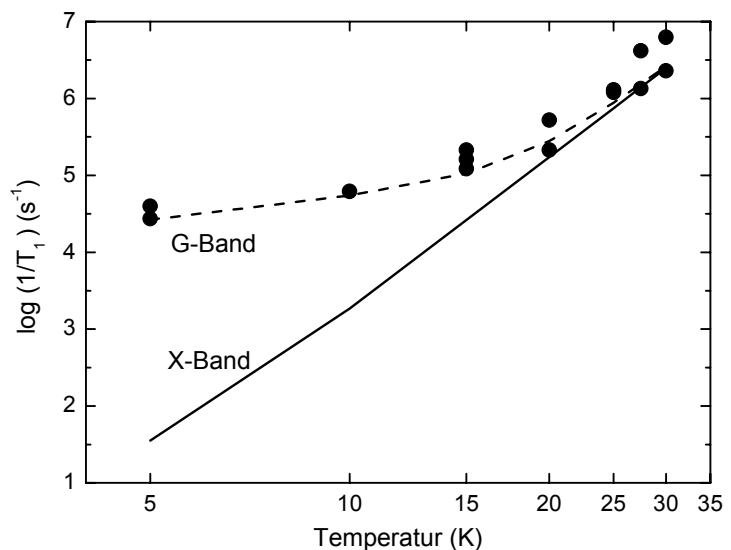
Aus den dipolaren Relaxationsmessungen ist deutlich geworden, dass die  $T_1$  Relaxation von low-spin Häm Eisen in Cytochrom *c* und von  $Cu^{2+}$  in  $Cu^{2+}$ -NO $\cdot$  sich im Hochfeld von der  $T_1$  Relaxation im X-Band unterscheidet. Die  $T_1$  Relaxation von  $Cu_A$  und  $Cu^{2+}$  in G-Band wurde daher mit Hilfe des IR Experiments näher untersucht.

Die  $T_1$  Werte von  $Cu_A$ , die bei Temperaturen zwischen 5 K und 30 K gemessen wurden, wurden erfolgreich laut:  $1/T_1 = A \cdot T^n + B \cdot T$  angefitet (Abbildung K.5).  $A$  und  $n$  sind dabei die Ramankoeffizienten und  $B$  der Koeffizient des direkten Prozesses. Die Ramankoeffizienten  $A$  und  $n$  waren für X-Band [Scholes et al. 1984] und für G-Band gleich,  $B$  war aber im Hochfeld um einen Faktor  $2 \cdot 10^3$  größer.

Die Temperaturabhängigkeit der  $T_1$  Relaxation von  $Cu^{2+}$  in  $Cu^{2+}$ -NO $\cdot$  wurde zwischen 20 K und 120 K direkt gemessen, dem gleichen Temperaturbereich wie für die dipolare Relaxationsmessungen. Die mit IR gemessenen Werte stimmten bis zu 100 K mit den  $T_1$  Werten aus dipolaren Relaxationsmessungen überein, was bedeutet, dass reines  $T_1$ -Verhalten gemessen wurde, und der Beitrag von spektraler Diffusion vernachlässigbar war. Die Relaxation von  $Cu^{2+}$ -NO $\cdot$  wurde nicht im X-Band gemessen. Der Vergleich mit Werten die für ähnliche  $Cu^{2+}$  Verbindungen bestimmt worden sind [Fielding et al. 2006] zeigte, dass auch hier der direkte Prozess eine viel grössere Rolle

spielt bei der  $T_1$  Relaxation im G-Band als im X-Band. Auch hier ist der Koeffizient des direkten Prozesses um etwa  $10^3$  grösser. Der Raman Prozess wurde in diesem Temperaturbereich im Hochfeld nicht wahrgenommen.

Abbildung K.5.  $T_1$  Relaxation von  $Cu_A$  in  $CcO_{II}$  im G-Band und im X-Band [Scholes et al. 1984]. Die Konzentration des  $CcO_{II}$  Proteins ist im Graphen angegeben, die X-Band Messungen sind von  $Cu_A$  in  $CcO$ . Die X-Band Kurve wird gegeben durch  $1/T_1 = 4.9 \cdot 10^{-4} T^{6.57} + 3.3T$ , die G-Band Simulation wird gegeben durch:  $1/T_1 = 4.9 \cdot 10^{-4} T^{6.57} + 5280T$ .



Die Feldabhängigkeit der  $T_1$  Relaxation erklärt, warum für low-spin Häm Eisen in Cytochrom c eine viel grössere Relaxationsrate bei den dipolaren Relaxationsmessungen bestimmt wurde. Nur zwei  $T_1$  Werte wurden in dem Temperaturbereich wo  $T_2^{\text{dip}} = T_{1f}$  bestimmt, sie lagen aber auf einer Gerade mit  $1/T_1 = B \cdot T$  und es konnte abgeschätzt werden, dass B um einen Faktor  $2 \cdot 10^4$  grösser war im Vergleich zu X-Band [Scholes et al. 1984].

Wir haben eine Zunahme der Effizienz des direkten Prozesses mit einem Faktor  $10^3$ - $10^4$  bei zunehmendem Magnetfeld wahrgenommen. Laut Relaxationstheorie [Orbach 1961] müsste dieser Faktor  $B_0^4$  sein, also in unserem Fall  $10^5$ .

## K.5. Schlussfolgerungen

Die dipolare Relaxationsmessung kann eine nützliche Unterstützung zur Strukturbestimmung sein. Allerdings muss die Probe folgende Bedingungen erfüllen: es muss die Möglichkeit bestehen, die intrinsische Relaxation des langsam relaxierenden Spins A getrennt zu messen von der Relaxation des dipolar gekoppelten A, damit die Division der beiden Messungen die reine dipolare Relaxation liefern kann. Die zwei gekoppelten Spins A und B müssen einen festen Abstand und eine feste Orientierung zu einander haben. Außerdem muss die  $T_1$  Relaxationsrate des schnell relaxierenden Spins B innerhalb des messbaren Temperaturbereichs kleiner sein als die dipolaren Kopplung in  $\text{rad s}^{-1}$ .

Eine andere Anwendung von dipolaren Relaxationsmessungen ist die Messung der  $T_1$  Relaxationszeiten von extrem schnell relaxierenden paramagnetischen Zentren, oder von paramagnetischen Zentren, die aus anderen Gründen schwer direkt zu messen sind.





## Abbreviations

ADP	Adenosine-diphosphate
ATP	Adenosine-triphosphate
CcO	Cytochrome <i>c</i> oxidase
CcO <sub>II</sub>	Subunit II from <i>Paracoccus denitrificans</i> cytochrome <i>c</i> oxidase
CT	3:7 chloroform: toluene mixture
Cu <sub>A</sub>	Binuclear copper center in CcO
Cu <sub>B</sub>	Mononuclear copper center in CcO
Cu <sup>2+</sup> -NO·	Cu <sup>2+</sup> -octoethylporphyrin-TPA
CW	Continuous wave
DMF	Dimethylformamide
ENDOR	Electron Nuclear DOuble Resonance
EPR	Electron Paramagnetic Resonance
ET	Electron Transfer
EXAFS	Extended X-ray Absorption Fine-Structure
HEPES	N-(2-hydroxyethyl)-piperazine-N'-2-ethanesulfonic acid
HF-EPR	High-Field/Frequency EPR
IR	Inversion Recovery
MeIm	Methylimidazole
NAD <sup>+</sup> /NADH	Nicotinamide Adenine Dinucleotide
Ni <sup>2+</sup> -NO·	Ni <sup>2+</sup> -octoethylporphyrin-TPA
NMR	Nuclear Magnetic Resonance
OEP	Orthoethylporphyrin
<i>P.d.</i>	<i>Paracoccus denitrificans</i>
PELDOR	Pulsed Electron DOuble Resonance (also called Double Electron-Electron Resonance, or DEER)
RIDME	Relaxation-Induced Dipolar Modulation Enhancement
SR	Saturation Recovery
SU	Subunit
THF	Tetrahydrofuran
TPA	12-O-tetradecanoylphorbol-13-acetate
UV-vis	Ultraviolet to visible light
ZFS	Zero-field splitting
<i>c</i> <sub>1</sub>	<i>Paracoccus denitrificans</i> cytochrome <i>c</i> <sub>1</sub>
<i>c</i> <sub>552</sub>	<i>Paracoccus denitrificans</i> cytochrome <i>c</i> <sub>552</sub>
<i>c</i> <sub>hh</sub>	Horse heart cytochrome <i>c</i>
cyt	Cytochrome
mw	Microwave
otp	Ortho-terphenyl
terpy	Terpyridine

## Symbols

$\Delta$	Dipolar coupling (in $\text{rad s}^{-1}$ )
$\alpha$	First Euler angle of rotation
$\beta$	Second Euler angle of rotation
$\beta_e$	Electronic $\beta$ factor
$\gamma$	Third Euler angle of rotation
$\theta_D$	First dipolar angle
$\lambda$	Wavelength (in nm)
$\nu$	Frequency (in Hz)
$\nu_{\text{dip}}$	Dipolar splitting (in Hz)
$\tau$	time between pulses in the Hahn echo sequence
$\tau_c$	Correlation time
$\varphi_D$	Second dipolar angle
$\omega$	Frequency (in $\text{rad s}^{-1}$ )
$\omega_0$	Larmor frequency (in $\text{rad s}^{-1}$ )
$B_0$	Static magnetic field (in T)
$B_1$	Excitation field (in T)
$H$	Hamilton operator
$J$	Exchange coupling (in $\text{rad s}^{-1}$ or in Hz)
$M_s$	Spin quantum number
$T$	Absolute temperature (in K)
$T$	Time between inversion pulse and detection sequence (IR and SR)
$T_1$	Longitudinal relaxation time
$T_{1f}$	Longitudinal relaxation time of the fast-relaxing spin
$T_2$	Transverse relaxation time
$T_2^{\text{dip}}$	Dipolar enhancement of $T_2$ relaxation time
$h$	Planck's constant
$\hbar$	Planck's constant/ $2\pi$
$r$	Distance between two paramagnetic centers (in nm)
$t_{\text{rep}}$	Repetition time





# Contents

Kurzfassung	VI
Abbreviations	XV
Symbols	XVI
1. Introduction	1
2. Theory	4
3. Methods	31
4. Cytochrome <i>c</i> and Cytochrome <i>c</i> Oxidase	46
5. Distance Measurements on Model Systems	65
6. $T_1$ Relaxation Measurements	81
7. Concluding Remarks	90
Appendices	92
Literature	110
Acknowledgments	115
Summary	117
Curriculum Vitae	120



## Chapter 1. Introduction

One central dogma of biology is that knowledge of the structure of a protein leads to (some) knowledge of its function. Since most proteins are too small to be studied in detail by microscopy, many indirect techniques to elucidate protein structures have been developed. X-ray spectroscopy is a frequently used technique that may provide accurate structural information on protein crystals. Structures of proteins in solution can be obtained by NMR spectroscopy, but there are limitations to the size of the proteins that can be measured. From optical and EPR spectroscopy more local information can be obtained about the direct surroundings of a chromophore (in optical spectroscopy) or of an unpaired electron (in EPR).

Whole protein structures cannot be obtained from EPR measurements, yet useful information can be obtained by studying the interaction of an unpaired electron with its environment, i.e. surrounding nuclei (from the protein or the solvent) and nearby unpaired electrons. The latter is exploited in the measuring of distances in EPR.

There are several techniques available for determining distances between two paramagnetic centers. The most commonly used, and probably the most straightforward experiment both in application and analysis, is PELDOR (pulsed electron-electron double resonance, also called DEER). One limitation of PELDOR is that a significant amount of both coupled spins needs to be excited in order to observe the PELDOR effect. For systems with very large line width, or for very fast-relaxing spins, dipolar relaxation measurements are more suitable.

Dipolar relaxation measurements are based on the fact that the presence of a fast-relaxing electron spin may cause faster relaxation of a dipolar-coupled, slower-relaxing spin. This effect depends strongly on the distance between the two spins, on the orientation of the interspin vector with respect to the spins, and of the two spins with respect to each other. The distance and, to some degree, the orientation can be obtained by dipolar relaxation measurements at X-band (9 GHz) frequency, but for more accurate determination of the orientation of the two spins high-frequency EPR measurements are necessary. Only at high frequency the EPR spectrum of many paramagnetic centers are fully resolved; this is a requirement for orientation-selective measurements.

This PhD thesis discusses the application of high-frequency EPR dipolar relaxation measurements. It is divided into three parts, of which the first two deal with dipolar relaxation measurements on biological and organic model systems, respectively, and the third deals with relaxation processes.

The first part describes the experiments we have performed to investigate the binding geometry of two electron-transfer proteins, cytochrome *c* and cytochrome *c* oxidase. These proteins are part of the respiratory, or electron-transfer chain, that completes the process of forming high-energy molecules (ATP) from energy sources such as sugar. The 3D structures of these proteins are well known, but nevertheless many questions remain unanswered. One of them is how electrons are transferred from cytochrome *c* to cytochrome *c* oxidase. As both of these electron-transfer proteins contain a paramagnetic center, their binding could be studied by EPR dipolar relaxation

measurements. In order to resolve the orientation dependence of dipolar relaxation, we performed the experiments at high microwave frequency (G-band, 180 GHz).

In the second part dipolar relaxation of model systems is described. The model systems studied were organic molecules with two paramagnetic centers, of which one was a nitroxide radical, and the other a metal ion. The molecules were designed especially to test EPR distance measurement methods. These tests were necessary, because the interpretation of dipolar relaxation data is not straightforward. A simulation program to aid the analysis was written and its applicability needed to be verified.

The third part investigates the magnetic field dependence of longitudinal relaxation processes. These were studied because it is essential for the analysis of dipolar relaxation data to have accurate knowledge of the relaxation of the dipolar-coupled partner spin. We had observed that the relaxation at high magnetic field was different from that at conventional X-band EPR, and therefore studied this dependence in more detail.

The purpose of this thesis is to discuss the applicability of dipolar relaxation studies –in particular those performed at high magnetic field- to problems in biology.



## Chapter 2. Theory

In this chapter the theoretical basis upon which this thesis rests will be explained. Sections 2.1 to 2.4 cover EPR theory, whereas section 2.5 is dedicated to the respiratory chain and cytochrome c oxidase. The theory is kept brief and for the greater part was taken from textbooks and review articles; only in special cases the original literature is cited. A complete treatise of magnetic resonance theory can be found in textbooks (e.g. [Abragam 1961; Carrington et al. 1967; Poole et al. 1971; Ernst et al. 1987; Berliner et al. 2000; Schweiger et al. 2001; Grinberg et al. 2004]) and will not be discussed in detail here. Literature on the respiratory chain is cited in section 2.5.

### 2.1. The Hamilton Operator

The total energy of a (spin) system is described by the full Hamilton operator of the system in question. To simplify calculations of properties of the spin system relevant to magnetic resonance, only energetically significant terms are taken into account. The terms of the resulting static Hamiltonian that are of interest to this thesis for  $i$  electrons and  $j$  nuclei are given by:

$$\hat{H} = \sum_i \hat{H}_i^Z + \sum_j \hat{H}_j^{nZ} + \sum_{i,j} \hat{H}_{i,j}^{hf} + \sum_{(i-1)!} \hat{H}_i^{\text{dip}} + \sum_{(i-1)!} \hat{H}_i^{\text{ex}} \quad \{2.1\}$$

which stand for the electron Zeeman interaction, the nuclear Zeeman interaction, hyperfine interaction, dipolar interaction and exchange interaction, respectively. The individual terms will be described in detail in the following sections.

#### 2.1.1. Electron Zeeman Interaction

The interaction between the magnetic moment of an electron spin  $S$  and the external magnetic field  $B_0$  is given by the electron Zeeman term:

$$\hat{H}^Z = \beta_e \hat{S} \cdot \hat{g} \cdot \vec{B}_0 \quad \{2.2\}$$

with  $\hat{S}$  the spin vector operator. For a spin system with  $S = 1/2$ , the dominant term in the Hamiltonian is generally this electron Zeeman term. The tensor  $\hat{g}$  is described by its eigenvalues  $g_{xx}$ ,  $g_{yy}$  and  $g_{zz}$ . It contains the orientation dependence of the electron spin density distribution on the atom or atoms under study, with respect to a certain molecular axis system. Deviation of the  $g$ -values from the free electron value (2.0023...) is caused by coupling of the spin angular momentum to the orbital angular momentum (spin-orbit coupling), and as such is dependent on the electronic properties of its surroundings and of the molecule. The  $g$ -anisotropy found in paramagnetic metals is usually much larger than that of organic radicals, due to the significantly larger spin-orbit coupling constant of metals with respect to atoms mostly found in organic radicals (H, C, N, O). Often, the  $g$ -anisotropy of organic radicals is so small that it cannot be resolved at the conventional X-band frequency (9 GHz) and measurements have to be performed at higher magnetic fields (see section 2.2).

For spin systems with cubic symmetry,  $g$  is isotropic, so  $g_{xx} = g_{yy} = g_{zz}$ . Axially symmetric systems are described with two  $g$ -values  $g_{\perp} = g_{xx} = g_{yy}$  and  $g_{\parallel} = g_{zz}$ , systems with rhombic symmetry have  $g_{xx} \neq g_{yy} \neq g_{zz}$ .

### 2.1.2. Nuclear Zeeman Interaction

The interaction between the magnetic moment of a nucleus  $I$  and the external magnetic field is given by the nuclear Zeeman term:

$$\hat{H}^{\text{nZ}} = \beta_n \hat{I} \cdot \hat{g}_n \cdot \vec{B}_0 \quad \{2.3\}$$

The spin quantum operator  $\hat{I}$  and the nuclear  $g$ -tensor  $\hat{g}_n$  are properties inherent to a specific nucleus; in most cases  $\hat{g}_n$  can be treated as a scalar. The gyromagnetic ratio  $\beta_n g_n$  of nuclei is at least a factor of 658 (as in the case of hydrogen nuclei) smaller than that of electrons.

### 2.1.3. Hyperfine Coupling

The hyperfine coupling follows from the interaction between an electron and one or more nuclei. It consists of an isotropic part, which reflects the finite probability of the electron to be found at a certain nucleus, and of an anisotropic part given by the dipole-dipole coupling between the nuclear and electronic magnetic moments:

$$\hat{H}^{\text{hf}} = a_{\text{iso}} \hat{S} \cdot \hat{I} + \hat{S} \cdot \hat{A}_{\text{dip}} \cdot \hat{I} \quad \{2.4\}$$

with  $a_{\text{iso}}$  the isotropic hyperfine coupling constant and  $\hat{A}_{\text{dip}}$  the dipolar term of the hyperfine coupling. From the hyperfine interaction information can be obtained about the local environment of the unpaired electron.

### 2.1.4. Dipolar Coupling

Nuclear and electron spins are magnetic dipoles and the interaction between two spins is thus termed dipole-dipole or dipolar interaction. This interaction depends strongly on the distance between the two spins,  $r$ , and on the orientation of the  $r$ -vector with respect to the magnetic field.

$$\hat{H}^{\text{dip}} = \gamma_A \gamma_B \left[ \frac{\hat{S}_A \cdot \hat{S}_B}{r^3} - \frac{3(\hat{S}_A \cdot \vec{r})(\hat{S}_B \cdot \vec{r})}{r^5} \right] \quad \{2.5\}$$

Where  $\gamma_A$  and  $\gamma_B$ ,  $\hat{S}_A$  and  $\hat{S}_B$  are the gyromagnetic ratios and the spin operators of spin A and spin B, respectively. When the scalar products in equation 2.5 are expanded and the expression converted into polar coordinates, six distinct terms are obtained that are arranged according to the change in the magnetic quantum number  $m_S$ . Replacing  $\gamma_i$  by  $\beta_e g_i^{\text{eff}}$  (with  $i = A$  or  $B$ ), the dipolar Hamiltonian can be written as [Bloembergen et al. 1948]:

$$\hat{H}^{\text{dip}} = \frac{g_A^{\text{eff}} g_B^{\text{eff}} \beta_e^2}{r^3} (A + B + C + D + E + F) \quad \{2.6\}$$

with:

$$\begin{aligned}
 A &= (3\cos^2(\theta_D) - 1)S_Z^A S_Z^B \\
 B &= -\frac{1}{4}(3\cos^2(\theta_D) - 1)(S_+^A S_-^B + S_-^A S_+^B) \\
 C &= -\frac{3}{2}\sin(\theta_D)\cos(\theta_D)\exp(-i\phi_D)(S_Z^A S_+^B + S_+^A S_Z^B) \\
 D &= -\frac{3}{2}\sin(\theta_D)\cos(\theta_D)\exp(+i\phi_D)(S_Z^A S_-^B + S_-^A S_Z^B) \\
 E &= -\frac{3}{4}\sin^2(\theta_D)\exp(-2i\phi_D)S_+^A S_+^B \\
 F &= -\frac{3}{4}\sin^2(\theta_D)\exp(+2i\phi_D)S_-^A S_-^B
 \end{aligned}$$

Where  $\theta_D$  is the angle between the r-vector and the z-axis of the magnetic field,  $\phi_D$  is the angle between the projection of the r-vector on the xy-plane of the magnetic field and the x-axis (see figure 2.1),  $S_+^k$  and  $S_-^k$  ( $k = A, B$ ) are the spin raising and spin lowering operators of spin  $k$  respectively, given by  $S_+ = S_x + iS_y$  and  $S_- = S_x - iS_y$ .

The terms A and B cover the zero-quantum transitions ( $\Delta m_{S,\text{total}} = 0$ ), C and D the single-quantum transitions ( $\Delta m_{S,\text{total}} = 1$ ), E and F the double-quantum transitions ( $\Delta m_{S,\text{total}} = 2$ ), where  $\Delta m_{S,\text{total}}$  is the sum of the change in magnetic quantum numbers of spin A and spin B.

In many cases the high-field approximation is valid, meaning the spins are quantized along the magnetic field, so that all the terms containing  $S_x$  or  $S_y$  in Hamiltonian 2.6 vanish, leaving only the A term:

$$\hat{H}^{\text{dip}} = \frac{g_A^{\text{eff}} g_B^{\text{eff}} \beta_e^2}{r^3} (3\cos^2(\theta_D) - 1) \quad \{2.7\}$$

$g_A^{\text{eff}}$  and  $g_B^{\text{eff}}$  the effective g-values of spin A and spin B, respectively.

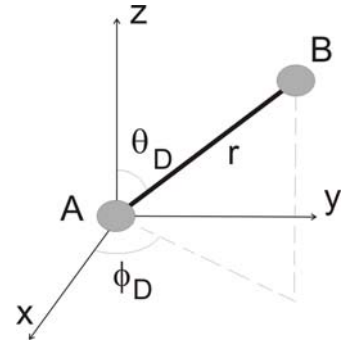


Figure 2.1. Parameters relevant to dipolar interaction with the z-axis of spin A oriented along  $B_0$ . A and B, the resonant and non-resonant coupled spin respectively;  $r$ , distance between the two paramagnetic centers;  $\theta_D$  and  $\phi_D$  the dipolar angles.

### 2.1.5. Exchange Interaction

Another type of interaction that occurs between two electrons is the exchange interaction  $J$ . Assuming an isotropic  $J$ , the exchange Hamiltonian is given by:

$$\hat{H}^{\text{ex}} = JS^A \cdot S^B = JS_Z^A \cdot S_Z^B + 2J(S_+^A \cdot S_-^B + S_-^A \cdot S_+^B) \quad \{2.8\}$$

and becomes relevant whenever there is significant overlap of the orbitals of spins A and B. The exchange interaction has no classical analogue; it is based on the Pauli principle which says that particles with half-integer spin (such as electrons) must have anti-symmetric wave functions, i.e. it is impossible for two electrons in the same orbital to occupy the same spin state.



## 2.2. High-Field EPR

In general, the criterion for high-field or high-frequency EPR (HF-EPR) is the ability to resolve the  $g$ -tensor of the spin under study, and is therefore not universally defined. However, EPR spectroscopy at fields higher than 3 T (and corresponding frequencies higher than ca. 90 GHz) is commonly referred to as HF-EPR, irrespective of the system under study.

There are several advantages to high-field spectroscopy, of which the most exploited is the higher spectral resolution due to the linear field dependence of the Zeeman interaction (equation 2.2). At W-band frequency (70-110 GHz) the  $g$ -tensor of most organic radicals can be resolved. This allows not only accurate determination of  $g$ -tensor values and separation of EPR spectra with slightly differing  $g$ -values, but also opens a door to orientation-selective measurements. The latter is a great advantage to pulse EPR experiments (see section 2.4). The combination of larger pulse lengths (leading to a smaller excitation bandwidth) and broader spectra makes a pulse experiment at high field very orientation selective, as only spins in a narrow distribution of orientations are excited. Pulse experiments performed at the edges of the spectra ( $g_{xx}$  and  $g_{zz}$ ) resemble experiments on single crystals, as only spins with one certain orientation with respect to the magnetic field are excited.

HF-EPR has a higher sensitivity than EPR at lower magnetic fields. This is both caused inherently by the higher Boltzmann polarization due to the larger Zeeman splitting, as well as by the experimental setup<sup>1</sup>. The bandwidth in HF-EPR is large enough to allow short mw pulses while sustaining a high quality factor  $Q$  due to the proportionality of the resonator bandwidth to the microwave frequency. This has advantages such as: good conversion factors for the microwave  $B_1$  field, a high sensitivity (which is proportional to  $Q$ ) and, in the case of pulse EPR, short ringing and dead time after the pulses [Prisner 1997; Prisner et al. 2001].

Another reason for doing HF-EPR measurements is that samples with very large zero-field splitting (ZFS) that are EPR silent at conventional X-band (9 GHz) frequency can become visible at high magnetic fields. In such cases the splitting between the energy levels due to ZFS is greater than the Zeeman splitting at X-band, and no spins are excited by the applied microwaves. Only at higher frequencies spins can be excited and then an EPR signal is observed.

Other advantages of HF-EPR are the suppression of forbidden transitions due to the well-fulfilled high-field approximation, and the different time window observed because of the change in Larmor frequency.

Some EPR-related questions may only be answered by the combination of experiments at different frequencies. This work is not the only example of multi-frequency EPR (see, e.g., [Un et al. 1994; Lakshmi et al. 2000; Weber et al. 2002; Jung et al. 2005; Kirilina et al. 2005] ). Performing measurements at different magnetic field strengths may be used to distinguish field-dependent from field-independent effects, or to determine which relaxation processes play a role by studying the frequency dependence of  $T_1$  relaxation.

---

<sup>1</sup> The second argument is only valid for spectrometers supplied with a microwave resonator, which includes many CW HF-EPR spectrometers and all pulse HF-EPR spectrometers.

HF-EPR also has its disadvantages. The high magnetic field requires the use of a helium-cooled superconducting magnet, which is more demanding in cost and maintenance than the electromagnets used at X-band frequency. Furthermore, many microwave components increase in cost and noise figure and decrease in power and sensitivity for higher microwave frequencies. At very high microwave frequencies the small wavelength ( $< 2\text{mm}$ ) does not permit the use of rectangular waveguides so that at frequencies above 140 GHz the implementation of quasi-optical components becomes necessary.

Besides these technical disadvantages there are problems that arise from having to use sample tubes on the same scale as the wavelength, which at G-band (180 GHz) amounts to capillaries with an inner diameter of 0.4 mm. This, on the other hand, can be seen as an advantage, especially in the case of protein samples, as only very little sample is required for HF-EPR measurements.

## 2.3. Relaxation

The processes by which a spin system returns to its equilibrium state after excitation are called relaxation processes. They are divided into longitudinal relaxation, also called spin-lattice relaxation, with the characteristic time  $T_1$ , and transverse relaxation, or spin-spin relaxation, with time constant  $T_2$ . Both processes, their mechanisms and methods by which  $T_1$  and  $T_2$  can be determined will be discussed in detail in the following sections. A rigorous explanation of relaxation theory can be found in some of the textbooks quoted at the beginning of this chapter and in [Murphy 1966; Poole et al. 1971; Orbach et al. 1972].

Longitudinal relaxation processes induce a change in the magnetic quantum number  $m_s$  and thus change the energy of the spin system. Energy conservation requires that the same energy quantum is absorbed or provided by the environment.

In general,  $T_1$  is the time constant associated with processes that restore the spin system to equilibrium.  $T_1$  is therefore defined as:

$$\frac{dn}{dt} = -\frac{n - n_0}{T_1} \quad \{2.9\}$$

where  $n$  is the population difference between the upper energy level ( $m_s = +1/2$ ) and the lower level ( $m_s = -1/2$ ), and  $n_0$  is  $n$  under equilibrium conditions. When microwave radiation is applied, the spin system builds up magnetization and when the radiation is switched off the system returns to equilibrium as  $\exp(-t/T_1)$ .

$T_1$  relaxation is also called spin-lattice relaxation because it is caused by the coupling of the spin to vibrations of the "lattice", or environment of the spin. This can be a crystal lattice, the surrounding solvent, or even the protein in which the spin is embedded. A lattice vibration of frequency  $\omega$  can only induce transitions between spin states separated by an energy interval  $\Delta E = \hbar\omega_0$  if  $\omega$  is in the range of the Larmor frequency  $\omega_0$ . The efficiency of a certain relaxation process therefore depends on the spectral density, which is to say the distribution of frequencies, around  $\omega_0$ . A typical vibration with correlation time  $\tau_c$  has a spectral density function given by a Lorentzian line shape:

$$J(\omega_0) = \frac{\tau_c}{1 + \omega_0^2 \tau_c^2} \quad \{2.10\}$$

The maximum in spectral density –and thus a maximum in relaxation rate– is found for  $\omega_0 \tau_c = 1$ .

In contrast to  $T_1$  relaxation,  $T_2$  relaxation does not cause the spin system to lose energy. Whereas spin-lattice relaxation causes loss of magnetization, spin-spin relaxation causes a loss of coherence. One process causing transverse relaxation is an energy-conserving flip-flop<sup>2</sup> process of two spins. Figure 2.2 shows a situation where such a flip-flop process (nearly) conserves energy. A spin flip that leads to longitudinal relaxation also destroys coherence, so that  $T_1$  relaxation contributes to  $T_2$  relaxation. This means that  $T_2$  can be smaller than or equal to  $T_1$ , but never larger. In solids the network of coupled spins is virtually infinite, so that  $T_2$  is often not well defined.

---

<sup>2</sup> "Flip" meaning a transition of  $\Delta m_s = \pm 1$ , "flop" a transition with  $\Delta m_s = \mp 1$

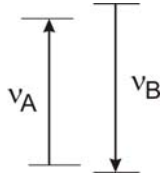


Figure 2.2. A double (flip-flop) transition in which the energy is nearly conserved. The transitions take place on neighboring spins A and B, and are marked by their respective frequencies  $\nu_A$  and  $\nu_B$ . Adapted from [Bloembergen et al. 1959].

### 2.3.1. Processes Causing Spin-Lattice Relaxation

There are three main processes that transfer energy from a spin to the lattice: the direct process, the Raman process, and the Orbach process.

The direct process involves the absorption of a phonon<sup>3</sup> that has a frequency equal to the Zeeman frequency of the spin system. This process depends linearly on temperature, and (for  $S = 1/2$  systems) depends on the magnetic field to the fourth power [Orbach 1961]. The direct process is often the most efficient relaxation process at low temperatures ( $T < 10$  K), but at higher temperatures the phonon density is maximum for frequencies that are much higher than  $\omega_0$ . It then becomes more efficient for the spin system to absorb a phonon with a higher frequency  $\omega_{\text{abs}}$  and emit a phonon with a difference frequency  $\omega_{\text{em}} = \omega_{\text{abs}} \pm \omega_0$ . Such two-phonon processes are the Raman process and the Orbach process. They can contribute significantly to  $T_1$  relaxation.

The Raman process is the inelastic scattering of phonons. One phonon excites the spin to a virtual excited state and a second phonon is released, thereby decreasing the overall energy of the spin system. The temperature dependence of the Raman process varies as a high power of the temperature. For spin  $S = 1/2$  systems, it is proportional to  $T^9 J_8(\theta_{\text{Deb}}/T)$ , where the transport integral  $J_n$  is defined as:

$$J_n\left(\frac{\theta_{\text{Deb}}}{T}\right) = \int_0^{\theta_{\text{Deb}}/T} x^n \frac{e^x}{(e^x - 1)^2} dx \quad \{2.11\}$$

with  $\theta_{\text{Deb}}$  the Debye temperature of the lattice, which is a certain temperature in the Debye model above which there are no more phonons. The function  $J_n(\theta_{\text{Deb}}/T)$  is a constant for small  $T$  and is proportional to  $T^{1-n}$  for large  $T$  ( $n > 1$ ), so that the relaxation caused by the Raman process increases as  $T^2$  at high temperatures. In the temperature region where the transition from the direct to the Raman process takes place  $T_1$  can vary as  $T^{-5}$ . The common Raman process for systems with  $S = 1/2$  is field-independent.

Paramagnetic systems with lower-lying excited states may also relax via the Orbach process. Just as the Raman process, the Orbach process is a two-phonon process, but in this case a real excited state is involved, instead of the "virtual" excited state in the Raman process. If present, the Orbach process is more efficient than the Raman process and has a characteristic temperature dependence:

$$\frac{1}{T_1} = \frac{\Delta_{\text{Orb}}^3}{\exp(\Delta_{\text{Orb}}/k_B T) - 1} \quad \{2.12\}$$

in which  $\Delta_{\text{Orb}}$  is the energy difference between the ground state and the involved excited state, and  $k_B$  is the Boltzmann constant. Aside from a possible dependence of the energy of the excited state on the external magnetic field, the Orbach process is independent of magnetic field.

<sup>3</sup> Phonons are quantized lattice vibrations

Spin-lattice relaxation times span the range of tens of femtoseconds (lanthanides in liquid solution) and nanoseconds (metal ions) to microseconds and even milliseconds (organic radicals).

### 2.3.2. Processes Contributing to Transverse Relaxation

In practice,  $T_2$  is usually not the dominating process of spin-echo dephasing: many other processes can contribute. In some cases competing relaxation processes can cause a non-exponential echo decay so that the spin-spin relaxation can no longer be described by a single time constant. The relaxation time is then described by the time it takes for the echo to decay to  $1/e$  of its starting intensity. In this thesis, the term  $T_2$  will be applied to both exponential and non-exponential echo decays.

One of the major processes that contribute to signal decay is spectral diffusion. These are processes that move magnetization through the EPR spectrum. If the EPR spectrum is only partly excited, the magnetization can be shifted out of the detection window, causing a decrease in echo intensity. Spectral diffusion can be caused by flip-flop processes involving spins that are excited (A spins) and spins that are not (B spins). Another source of spectral diffusion is reorientation of the molecule on the time scale of the experiment, causing changes in the Larmor frequency of the excited species. The reorientation of a molecule may cause anisotropic relaxation in the spectrum (see, e.g. [Prisner 1997; Grimaldi 2002; Schnegg et al. 2002; Kirilina et al. 2005]). Cross relaxation is another process that causes transverse relaxation and is closely related to spectral diffusion, although in this case mutual spin flips between unlike spins, such as electrons and nuclei, are involved.

Instantaneous diffusion is observed in spin echo experiments when the concentration of spins per mT is sufficiently high that the mw pulse flips both the observed spin and a neighboring B spin. Coupling of the observed spin to the B spin changes the Larmor frequency of the observed spin and therefore contributes to dephasing of the magnetization.

A process that can strongly enhance the transverse relaxation is relaxation caused by dipolar coupling between two paramagnetic species. This special case of spectral diffusion will be treated explicitly in the next section.

The total echo decay is given by the product of the independent relaxation processes. If the relaxation processes are single exponentials, the total transverse relaxation time  $T_2$  is therefore given as the inverse of the sum of the reciprocal relaxation times of the involved processes (sd, spectral diffusion; id, instantaneous diffusion; dip, dipolar relaxation) :

$$\frac{1}{T_m} = \frac{1}{T_2} + \frac{1}{T_2^{sd}} + \frac{1}{T_2^{id}} + \frac{1}{T_2^{dip}} + \dots \quad \{2.13\}$$

The timescale of transverse relaxation times ranges from femtoseconds (systems with  $S > 1/2$ ) to microseconds (organic radicals).

### 2.3.3. Dipolar Relaxation Enhancement

Dipolar relaxation enhancement by a fast-relaxing spin can be observed on  $T_1$  and on  $T_2$  of the slow-relaxing species, providing that the intrinsic  $T_1$  or  $T_2$  relaxation rate is small enough. It can be deduced that a minimum in longitudinal relaxation enhancement time  $T_1^{\text{dip}}$  appears when  $1/T_{1f} = \omega_A$ , with  $T_{1f}$  the  $T_1$  of the fast relaxing spin B and  $\omega_A$  the Larmor frequency of the observed spin A.  $T_1$  relaxation enhancement measurements are extremely sensitive to distances between paramagnetic centers due to a  $r^{-6}$  dependence of  $\Delta$ . However, for experimental reasons (undetectable signal caused by very short  $T_1$  and  $T_2$  of spin A at temperatures where  $1/T_{1f} = \omega_A$ ) in this study the focus has been on transverse relaxation enhancement.  $T_1$  relaxation enhancement will, therefore, not be treated in further detail.

The transverse relaxation enhancement of an observed spin caused by dipolar coupling to a fast-relaxing spin is [Salikhov et al. 1981]:

$$\Phi_{\text{dip}}(2\tau) = R^{-2} \left[ \exp(-2\tau T_{1f}^{-1}) (\sinh^2 R\tau T_{1f}^{-2} + R^2 \cosh^2 R\tau + R \sinh 2R\tau T_{1f}^{-1} + \Delta^2 \sinh^2 R\tau) \right] \quad \{2.14\}$$

with  $R^2 = (T_{1f})^{-2} - \Delta^2$  and  $\Delta$  is one half of the dipolar splitting in  $\text{rads}^{-1}$ . This formula can be greatly simplified in the fast or slow motion (with respect to  $\Delta$ ) limits, i.e.  $R^2 \gg 1$  or  $R^2 \ll 1$  respectively. In the fast motion limit:

$$\Phi_{\text{dip}}(2\tau) = \exp\left(-2\tau \frac{\Delta^2 T_{1f}}{2}\right) \quad \{2.15a\}$$

and in the slow motion limit:

$$\Phi_{\text{dip}}(2\tau) = \exp\left(\frac{-2\tau}{T_{1f}}\right) \quad \{2.15b\}$$

(see [Kispert et al. 1982] for derivation)

Equations 2.15 demonstrate that the dipolar relaxation enhancement has a very specific dependence on  $T_{1f}$  of the fast-relaxing spin. As  $T_1$  is strongly temperature dependent, dipolar relaxation also depends strongly on temperature. This is illustrated in figure 2.3, where simulations were performed for two dipolar coupled paramagnetic species with an interspin distance of 2 nm at different temperatures. At low temperature (i.e., in the range where  $1/T_{1f} \ll \Delta$ ), the dipolar relaxation is independent of  $\Delta$  and only depends on  $T_{1f}$  (equation 2.15b). At high temperature ( $1/T_{1f} \gg \Delta$ ), the dipolar relaxation depends both on  $T_{1f}$  and on the dipolar coupling strength  $\Delta$  (equation 2.15a). A maximum in transverse dipolar relaxation enhancement is found for  $1/T_{1f} = \Delta$ .

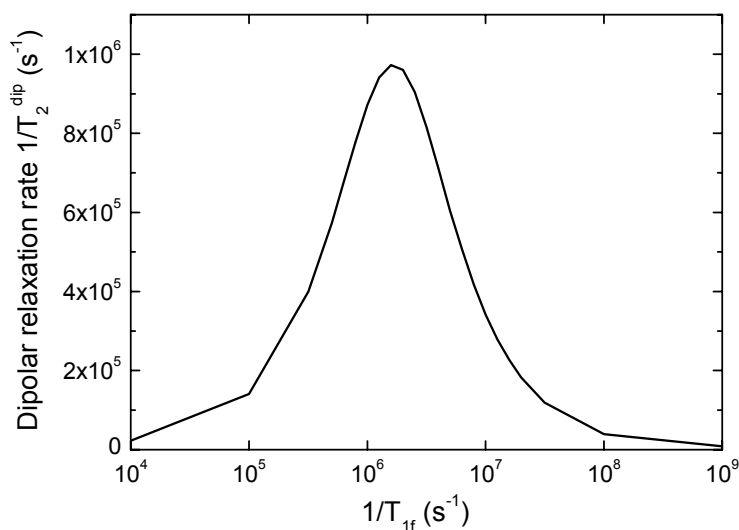
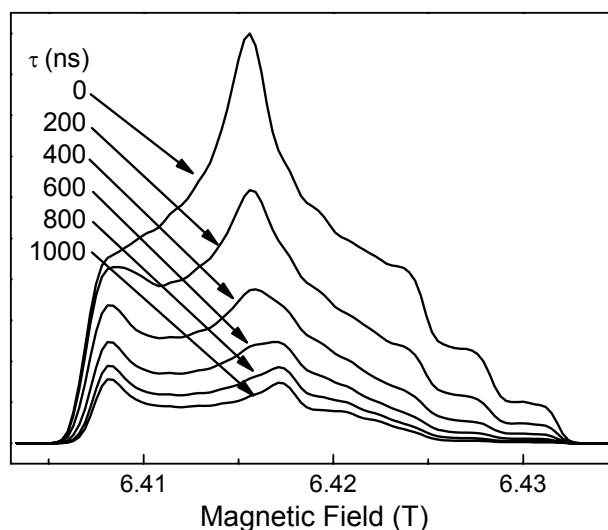


Figure 2.3. Dipolar relaxation rates ( $1/T_2^{dip}$ ) of spin A coupled to spin B with a coupling strength  $\Delta = 39 \cdot 10^6 \text{ rads}^{-1}$  (6.2 MHz). At low temperatures where  $1/T_{1f} \gg \Delta$ ,  $T_2^{dip} = T_{1f}$ ; a maximum in dipolar relaxation rate is found where  $1/T_{1f} = \Delta$ ; at high  $T_{1f}$  rates where  $1/T_{1f} \ll \Delta$ ,  $T_2^{dip} = 2/\Delta^2 T_{1f}$ .

The dipolar coupling strength strongly depends on the orientation of  $\theta_D$ , the angle between the external magnetic field and the vector connecting the two dipolar coupled spins (see equations 2.6 and 2.7). In a spin system with two dipolar coupled spins that exists in one specific geometry, the dipolar relaxation is expected to vary over the spectrum. At some positions in the spectrum the dipolar relaxation will be maximal (where  $\theta_D \approx 0^\circ$ ), at other positions dipolar relaxation will not be seen at all (where  $\theta_D \approx 54.7^\circ$ ). This is illustrated in figure 2.4, where a simulation has been performed for a spin system with very pronounced dipolar relaxation anisotropy.

At high temperatures ( $1/T_{1f} \gg \Delta$ ) the dipolar relaxation, measured at a position in the spectrum that is not orientation selective, cannot be simulated by a single exponential. This is caused by the orientation dependence of  $\Delta$ . At such a non-selective point in the spectrum many spins contribute to the signal and, consequently, many values of  $\theta_D$  are detected. These spins have different values of  $\Delta$  and therefore the sum of their different relaxation traces is non-exponential.

Figure 2.4. Simulations of field-swept spectra of a dipolar coupled nitroxide spin at a temperature where the dipolar relaxation is sensitive to dipolar coupling strength. The field-swept spectra are simulated for different inter-pulse spacing times  $\tau$ . In this particular case the  $g_{xx}$  axis of the molecule makes an angle  $\theta_D$  with the dipolar axis that is close to the magic angle. The  $g_{xx}$  position in the spectrum (the low-field edge) therefore experiences a significantly smaller dipolar coupling than the rest of the spectrum, causing only little dipolar relaxation at  $g_{xx}$ . As a result, the  $g_{xx}$  peak appears to rise with respect to the rest of the spectrum when  $\tau$  is increased.



### 2.3.4. Methods to Measure Relaxation Times

There are several methods to measure the longitudinal relaxation time  $T_1$  of which three pulsed methods will be discussed here (figure 2.5).

In the inversion recovery (IR) experiment, the magnetization is first flipped into the  $-z$  direction by application of a  $\pi$  pulse (figure 2.5.b). The recovery of the magnetization is then followed by applying a Hahn-echo detection sequence after a time  $T$ , which is incremented during the experiment. In the ideal case where the initial  $\pi$  pulse inverts all the spins the magnetization recovers as:  $a - 2 \exp(-\frac{T}{T_1})$ , with  $a=1$ . Usually,

because the entire EPR spectrum cannot be excited, and due to the presence of dead-time,  $a$  is normally significantly smaller than 1. To minimize the contributions from spectral diffusion to the signal decay the first pulse is hard (large excitation bandwidth) whereas the detection sequence is soft (smaller bandwidth). Nevertheless, the contribution of spectral diffusion is not negligible in most cases.

A more accurate method to measure  $T_1$  is saturation recovery (SR). The first pulse, or first set of pulses, in the SR sequence (figure 2.5.c) serves to saturate the spin system, i.e. to create a zero net magnetization. A Hahn-echo sequence serves to detect the echo intensity at a recovery time  $T$  after saturation. The echo intensity is given by  $1 - \exp(-\frac{T}{T_1})$ . Unlike in IR, in a SR experiment the magnetization recovers from zero and

not from  $-1$ , making the experiment less sensitive by a factor of two. However, spectral diffusion contributions can be almost eliminated if the applied saturating pulse is long or if the number of saturating pulses at the beginning of the pulse sequence is high enough (figure 2.5.d).

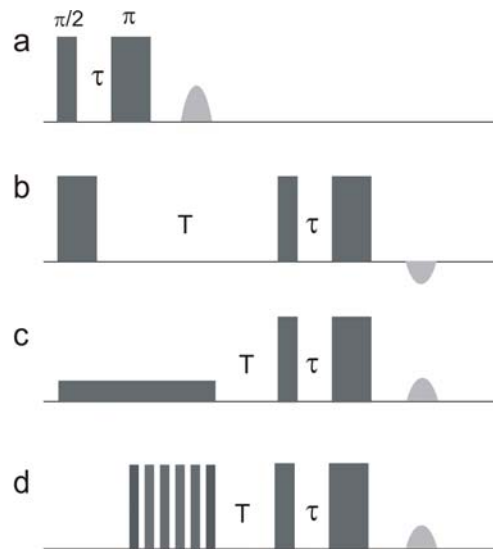


Figure 2.5. Pulse sequences of some common relaxation experiments. a, Hahn echo; b, inversion recovery (IR); c, saturation recovery (SR) with long saturating pulse; d, SR with picket-fence saturation

For very long  $T_1$  values it may be more convenient to study the saturation behavior of the spin echo as a function of the repetition rate of the experiment. A Hahn echo sequence is applied and the echo intensity is recorded as a function of the repetition rate.  $T_1$  may be read off from the ensuing spectrum as the repetition time where the echo has 0.6 times the initial intensity [Ernst et al. 1966], or in case of mono-exponential relaxation the data points may be fitted by:



$$\frac{\Phi(t_{\text{rep}})}{\Phi(t_{\text{rep}} \rightarrow \infty)} = 1 - \exp(-t_{\text{rep}} / T_1) \quad \{2.16\}$$

where  $\Phi$  is the echo intensity as a function of the repetition time  $t_{\text{rep}}$ . In this experiment it is not possible to avoid the admixture of spectral diffusion.

Due to technical restrictions of the G-band spectrometer it was only possible to measure longitudinal relaxation using the IR sequence for short  $T_1$  values ( $< 10 \mu\text{s}$ ), and by varying the repetition rate of the experiment for long  $T_1$  values.

The transverse relaxation time can be measured using a Hahn echo sequence as depicted in figure 2.5.a. The echo intensity is monitored as a function of the time  $\tau$ . The resulting echo decay trace is given by all processes that cause echo decay as explained above, and can often be simulated with a single exponential function with decay time  $T_2$ . In some cases the transverse relaxation is more complicated and the echo decay trace cannot be simulated by one exponential.

## 2.4. Methods of Measuring Distance by EPR

The measurement of distances between spins by magnetic resonance spectroscopy is a measurement of the dipolar coupling between the two spins. As discussed above, the presence of a second spin B causes a change in the Larmor frequency of the observed spin A. There are several methods in EPR to determine the size of this dipolar coupling.

### 2.4.1. CW Methods

The dipole-dipole interaction of two coupled spins causes the resonance lines of the observed spin to split<sup>4</sup> in two. Neglecting J and taking only the first secular term of the dipolar Hamiltonian 2.6, the frequency of this splitting (in rad s<sup>-1</sup>) is given by:

$$\omega_{\text{dip}} = 2\pi\nu_{\text{dip}} = \frac{g_A^{\text{eff}} g_B^{\text{eff}} \beta_e^2}{\hbar r^3} (3 \cos^2(\theta_D) - 1) \quad \{2.17\}$$

with  $\nu_{\text{dip}}$  the dipolar splitting in Hz.

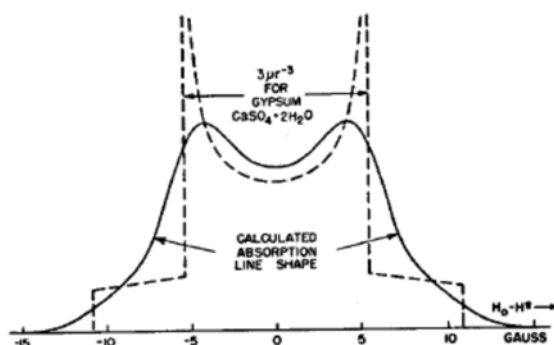


Figure 2.6. Dipolar pattern as calculated for gypsum by G.E. Pake [Pake 1948]. The broken line is the calculated dipolar spectrum, the continuous line is the calculated spectrum folded with a Gaussian line width of 15.4 mT.

When the full EPR line is excited, the split lines display a so-called Pake pattern (see figure 2.6) due to the angular term in equation 2.17. This pattern is obtained by summing up all dipolar coupling frequencies resulting from orientations of the molecule where  $\theta_D = 0^\circ$  to those where  $\theta_D = 90^\circ$ , weighted by the probability of the respective orientation given by  $\sin(\theta_D)$ . In most cases, the Pake pattern is not resolved due to inhomogeneous line-broadening. The observed splitting is then assumed to be caused by the most intense orientation, which has  $\theta_D = 90^\circ$ , making the angular term equal to 1. At temperatures where the spin tumbles or rotates rapidly compared to the dipolar coupling (usually  $10^7 - 10^6 \text{ s}^{-1}$ ) the angular term averages to 0 and no dipolar splitting can be observed.

The isotropic exchange coupling adds to the dipolar coupling and shifts the Pake pattern, but does not influence its shape (figure 2.7).

<sup>4</sup> This thesis deals only with spins with  $S=1/2$ , therefore the EPR line of the observed spin is split into two by its interaction with one coupled spin

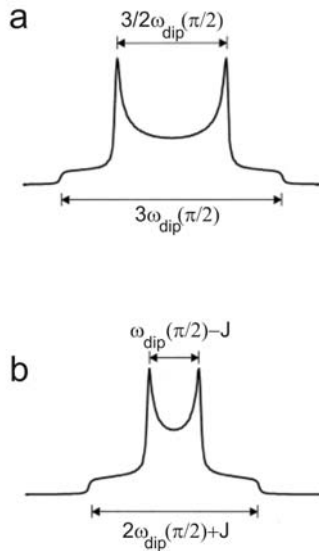


Figure 2.7. Dipolar coupling patterns for the strong coupling case (a) and the weak coupling case (b).  $\omega_{dip}$  frequency of dipolar coupling (in  $\text{rads}^{-1}$ ). Adapted from [Jeschke 2002].

The success of distance measurements by studying the splitting by dipolar coupling depends strongly on the line width of the observed spin. Inhomogeneous broadening of a line can cover up the effects of dipolar coupling, and even for narrow lines this method is restricted to distances up to approximately 1.5 nm.

Another CW method to measure dipolar coupling is by performing saturation experiments at various temperatures, and to study the relaxation behavior of a dipolar coupled spin in this fashion. The interpretation of CW saturation experiments is complicated, however. More precise measurements of relaxation times can be performed with pulse EPR. Dipolar relaxation measurements using pulse EPR will be discussed in section 2.4.4.

#### 2.4.2. Pulsed Electron-Electron Double Resonance

The dipolar coupling of spin B to spin A causes a change in the resonance frequency  $\omega_A^{\text{tot}}$  of spin A, which depends on the spin state of spin B:

$$\omega_A^{\text{tot}} = \omega_A + \omega_{dip} M_S^B \quad \{2.18\}$$

where  $\omega_A$  is the Larmor frequency of spin A in absence of dipolar coupling and  $M_S^B$  is the quantum number associated with spin B and which assumes values of  $\pm 1/2$ . From equation 2.18 it becomes clear that when spin B flips, the resonance frequency of spin A changes by:  $\omega_A \pm \frac{1}{2} \omega_{dip} - (\omega_A \mp \frac{1}{2} \omega_{dip}) = \pm \omega_{dip}$ .

In a normal Hahn-echo experiment (figure 2.8.a), the A spins are rotated into the xy plane by a  $\pi/2$  pulse; they dephase and then rephase again after a  $\pi$ -pulse at time  $t = \tau$  has inverted their phase. An echo appears at  $t = 2\tau$ . In a pulse electron-electron double resonance experiment (PELDOR, also called DEER) the Hahn-echo sequence with frequency  $\nu_A$  is applied for detection of the A spins and a so-called pumping pulse with frequency  $\nu_B$  is applied at a time  $T$  ( $0 < T < \tau$ ) between the two pulses of the detection sequence (figure 2.8.b). The pumping pulse induces a spin flip in the B spins so that A spins coupled to B spins fail to refocus, decreasing the intensity of the A spin echo signal. The phase that the coupled A spins accumulate due to the B-spin flip at time  $T$  is  $\omega_{dip} T$  [Larsen et al. 1992], so that a plot of the A spin echo intensity vs. time  $T$  shows a  $\cos(\omega_{dip} T)$  dependence. Fourier transformation of the modulation on the echo decay trace in the ideal case gives a Pake pattern, but as in the CW case, also in PELDOR often only the most intense  $\theta_D = 90^\circ$  peak can be resolved.

In practice, a single A spin will not be coupled to a single B spin. Smaller, less well-resolved dipolar couplings of B spins to A spins cause both an exponential-like echo decay and a faster damping of the oscillation. For more details about the experiment as

well as a description of the four-pulse PELDOR sequence the reader is referred to the original literature [Milov et al. 1984; Larsen et al. 1992; Martin et al. 1998].

PELDOR was not used for our distance measurements because the large  $g$ -anisotropy of the cytochrome heme makes it impossible to excite a large enough fraction of spins to obtain a PELDOR signal even at X-band. Additionally, the relaxation time of  $\text{Cu}_A$  is too short for a suitable time window for PELDOR measurements. At high field, PELDOR could not be measured for the  $\text{Cu}^{2+}$ -nitroxide pair either because the two species differ too much in  $g$ -values. At X-band, PELDOR measurements of a  $\text{Cu}^{2+}$ -nitroxide molecule were successfully performed [Bode; Narr et al. 2002].

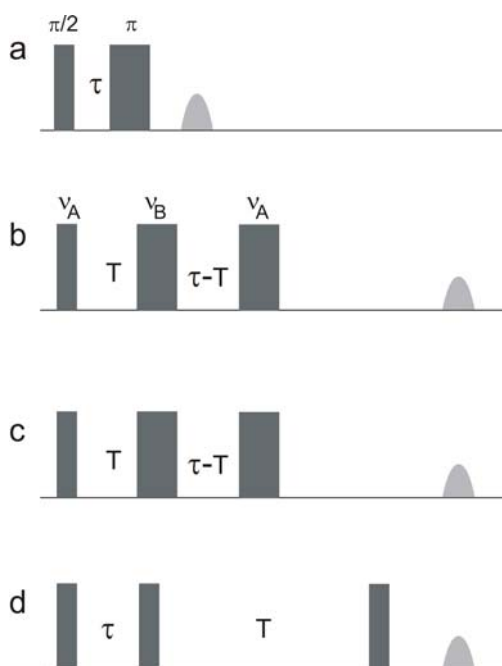


*Figure 2.8. Pulse sequences of EPR distance measurements. a, Hahn echo; b, PELDOR, where the second pulse has a different mw frequency than the first and the third; c, "2+1"; d, RIDME. In PELDOR and in "2+1" the time  $T$  is varied and  $\tau$  is kept constant, whereas in RIDME, as in (dipolar)  $T_2$  relaxation experiments,  $\tau$  is varied. See the text for details about the experiments.*

The "2+1" experiment is an alternative to PELDOR for overlapping spectra with narrow line widths that make selective excitation impossible. The pulse sequence (figure 2.8.c) is essentially the same as the three-pulse PELDOR sequence, but in this case all the pulses have the same frequency. This complicates data analysis, as the B spin may be flipped by either the second pulse, the third pulse, or both, which causes different dependences of echo modulation on time. Adjustment of the lengths of the second and third pulses allows optimization of the observed dipolar signal, for example by changing the ratio between the modulated and unmodulated part.

#### 2.4.3. Relaxation-Induced Dipolar Modulation Enhancement

In dipolar-coupled systems where one of the spins has a short  $T_1$  there is no need of a pumping pulse to study dipolar interaction. In the relaxation-induced dipolar modulation enhancement (RIDME) experiment the Larmor frequency of the detected spin A is affected by spontaneous spin flips of the coupled spin.

The first pulse in the RIDME sequence (figure 2.8.d) flips the A spins into the  $xy$  plane where they start to dephase, creating a polarization grating. The second  $\pi/2$  pulse rotates the magnetization into the  $xz$  plane where it is stored for a time  $T$ . During  $T$ , the

faster relaxing B spin flips due to  $T_1$  relaxation and so changes the Larmor frequency of spin A. After the A spins have been rotated into the xy plane by the third  $\pi/2$  pulse, the coupled spins do not refocus and a decrease in echo intensity is observed. With  $\tau \ll T_{1B}$  and  $T \geq T_{1B}$  (where  $T_{1B}$  is  $T_1$  of the B spin), spin flips of the B spins only occur during T and the signal is independent of the particular moment at which the Larmor frequency of spin A has changed. If T is kept fixed and  $\tau$  is stepped, an echo decay trace is obtained that is modulated by  $\cos(\omega_{dip}T)$ , similar to the PELDOR signal. Details about this experiment can be found in papers by Kulik and Dzuba [Kulik et al. 2001; Kulik et al. 2002; Kulik et al. 2004].

We did not perform this type of measurements because the dead time of the high-field spectrometer was very large in comparison to the inverse dipolar coupling, making it almost impossible to perform accurate measurements.

Another pulsed EPR method to measure distances between two (or more) paramagnetic centers is double quantum coherence (DQC) [Saxena et al. 1996; Saxena et al. 1997]. This method requires the excitation of the whole EPR line, and consequently it could not be applied to our system: the studied spectra were too broad. DQC will therefore not be explained here.

#### 2.4.4. Dipolar Relaxation Enhancement

Dipolar relaxation measurements are closely related to the PELDOR and RIDME experiments in that they rely on the dephasing of A spins due to spin flips by B spins to which they are dipolar coupled. Like in RIDME, the B spins are not excited by an additional microwave pulse, but flip due to  $T_1$  relaxation processes. The echo intensity of the A spins is recorded with a simple Hahn echo sequence (figure 2.8.a) as a function of the pulse separation time  $\tau$ .

Changes in the Larmor frequency of spin A occur due to stochastic flips of spin B caused by  $T_1$  relaxation during the time  $\tau$  between the two pulses (and between the second pulse and the appearance of the echo). This process is the same as in the case of RIDME, except that in this case the flips of the B spins occur at any time between  $t = 0$  and  $t = 2\tau$ , causing relaxation enhancement instead of modulation of the echo signal. This complicates the analysis of dipolar relaxation data, and a single measurement no longer suffices to unambiguously obtain all structural parameters. We therefore performed relaxation measurements at different microwave frequencies (X-band and G-band), as well as at different temperatures. The dipolar relaxation traces were simulated to extract the length and orientation of the dipolar vector, as well as the mutual orientation of the two paramagnetic centers and the exchange coupling. A strict requirement for these simulations is that  $T_{1f}$  is accurately known (to within a factor of two).

A problem in studying dipolar relaxation is the intrinsic transverse relaxation time of the spin under study. The total echo signal is given by:

$$\Phi_{\text{tot}}(2\tau) = \Phi_{\text{Adecay}}(2\tau)\Phi_{\text{dip}}(2\tau) \quad \{2.19\}$$

where  $\Phi_{\text{Adecay}}$  represents the intrinsic echo decay of spin A in absence of spin B. To obtain the pure dipolar echo decay  $\Phi_{\text{dip}}$ , the total echo signal needs to be divided by the signal of spin A alone:

$$\Phi_{\text{A}}(2\tau) = \Phi_{\text{Adecay}}(2\tau) \quad \{2.20\}$$

The extraction of the pure dipolar relaxation signal  $\Phi_{\text{dip}}$  is a prerequisite for a quantitative simulation and interpretation of relaxation measurements.

## 2.5. The Respiratory Chain

The respiratory chain consists of a series of metalloprotein complexes. It transfers electrons through a redox potential span of 1.1 V from the  $\text{NAD}^+/\text{NADH}$  redox couple to the  $\text{O}_2/\text{H}_2\text{O}$  couple, thereby pumping protons across the mitochondrial or bacterial membrane (figure 2.9). The ensuing electrochemical potential is used by the enzyme ATP synthase to create energy-rich ATP. The transfer of electrons by sequential reduction and oxidation steps, and the additional pumping of protons from the inner, negative, N-side of the membrane to the outer, positive, P-side of the membrane is performed by four complexes: NADH:ubiquinone oxidoreductase (complex I), succinate:ubiquinone oxidoreductase (complex II, does not pump protons), ubiquinone:cytochrome c oxidoreductase (complex III) and cytochrome c oxidase (complex IV, CcO). The flow of electrons through these complexes is given schematically in figure 2.10. ATP synthase, or complex V, uses the energy released from the flow of the protons back across the membrane to perform the chemical work of producing ATP from ADP and inorganic phosphate.

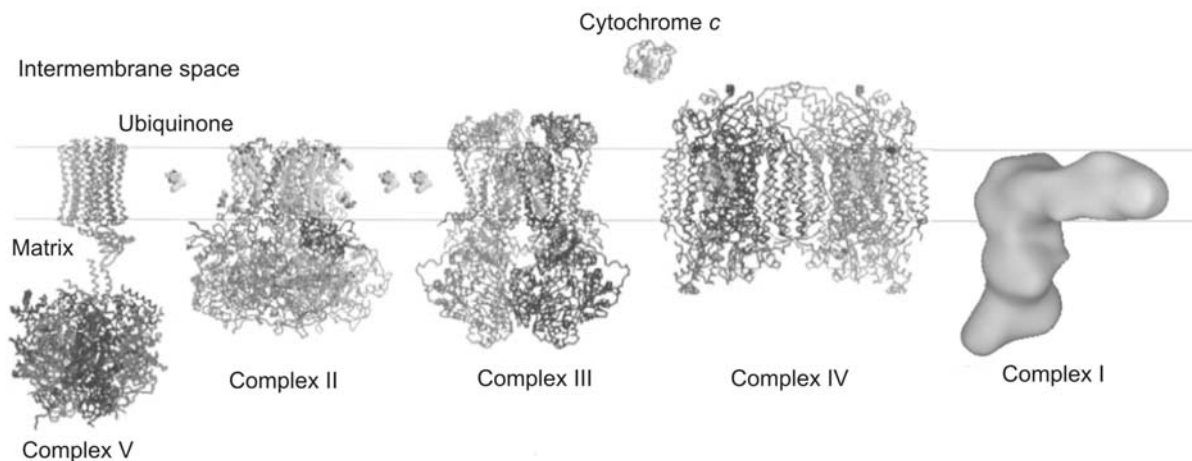


Figure 2.9. The respiratory chain. Figure taken from [Rich 2003], with exception of Complex I from *Yarrowia Lyppica* (from [Maly 2004]). Pdb files of the crystal structures: yeast ATP synthase, 1QO1; trimer of bacterial Complex II, 1NEK; dimer of mammalian Complex III, 1BGY; dimer of mammalian Complex IV, 2OCC; mitochondrial cytochrome c, 1HRC.

The redox-active centers of the respiratory chain enzymes are very diverse. They consist of flavoproteins, cytochromes that contain porphyrin prosthetic groups, iron-sulfur centers, ubiquinone and protein-bound copper centers. Aside from flavoproteins and ubiquinone, which can also react with two protons and two electrons, each of these centers can donate or accept one electron.

During the last several years, all but one<sup>5</sup> of the respiratory chain complexes were crystallized and subsequently analyzed by X-ray spectroscopy. This greatly increased the understanding of the mechanisms of electron and proton translocation. There are, however, many questions that could not be answered by X-ray crystal structures. Biochemical methods and optical, NMR and EPR spectroscopic methods have been

<sup>5</sup> As this thesis was being written, the transmembrane half of Complex I was crystallized and analyzed using X-ray spectroscopy: Sazanov, L. Hinchliffe, P. *Science* **311**: 1430 (2006)

successful in answering some, but even with the help of such advanced techniques, many issues remain open to debate.

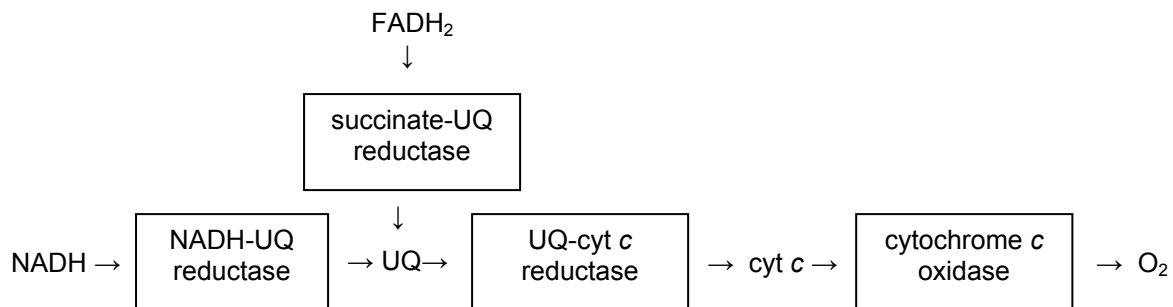


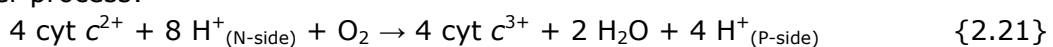
Figure 2.10. Schematic electron flow through the respiratory chain. The respiratory chain complexes are shown in boxes, mobile electron carriers are given by abbreviations: UQ, ubiquinone; cyt c, cytochrome c. The figure was adapted from [Maly 2004].

One of these issues is the possible formation of supercomplexes: ordered clusters of respiratory enzymes that have been isolated from bacteria and yeast as well as from mitochondria [Schägger 2002]. The formation of supercomplexes is thought to stabilize the individual enzyme complexes, especially complex I, and facilitate the electron transfer from the small electron carriers in the respiratory chain (ubiquinone and cytochrome c) which then do not need to diffuse between the enzyme complexes. Both the occurrence in nature and the exact composition of these supercomplexes is still under discussion; no evidence from spectroscopic techniques has been found yet.

In the following section, only cytochrome c oxidase and cytochrome c will be described in detail. More information on the respiratory chain and its components can be found in textbooks such as [Stryer 1995; Messerschmidt et al. 2001; Nicholls et al. 2002], or in recent reviews [Schultz et al. 2001; Brzezinski et al. 2003; Rich 2003; Wikström 2004; Hosler et al. 2006]. More details about cytochrome c oxidase can be found in [Richter et al. 2003; Faxén et al. 2005].

### 2.5.1. Complex IV, Cytochrome c Oxidase

Cytochrome c oxidase (CcO) catalyzes the oxidation of cytochrome c and transfers the electrons to O<sub>2</sub> to form H<sub>2</sub>O. For every O<sub>2</sub> molecule, four protons are taken up from the N-side of the membrane to form water. Four additional protons are pumped from the N-side to the P-side of the membrane, greatly increasing the efficiency of the electron transfer process:



The structures of CcO from various organisms have been solved to high resolution, both by X-ray diffraction and by NMR (e.g. [Iwata et al. 1995; Yoshikawa et al. 1998; Reincke et al. 2001]).



The mammalian CcO is a very large structure that spans the inner mitochondrial membrane. It is a functional dimer with each monomeric unit being composed of 13 different polypeptides. Together with simpler bacterial oxidases it belongs to a superfamily whose members contain the same three highly conserved subunits I, II and III (figure 2.11). These three subunits form a catalytic core that can catalyze all of the electron- and proton-transfer reactions. Subunit I is the largest subunit, containing 12 transmembrane helices and three of the four redox centers involved in the oxygen reduction reaction: heme a, heme a<sub>3</sub> and Cu<sub>B</sub>. The second-largest subunit, subunit II, possesses two transmembrane helices and a large globular domain. This is the location of the fourth redox center, Cu<sub>A</sub>, which has two copper atoms in a cluster with two sulfur atoms (figure 2.12). This binuclear copper center can undergo one-electron oxidation-reduction reactions.

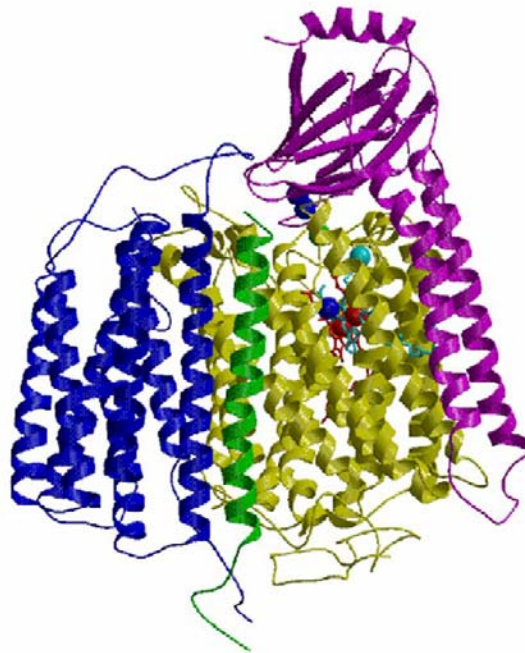


Figure 2.11. Crystal structure at 2.8Å resolution of *Paracoccus denitrificans* cytochrome c oxidase (Pdb file 1BGY) from [Iwata et al. 1995]. Figure generated with WebLab ViewerPro and rendered with POV-Ray. The protein is shown in ribbon representation with each subunit in a different color (SUI, yellow; SUII, magenta; SUIII, green; SUIV, blue). The cofactors (hemes and metal ions) are shown in ball-and-stick fashion.

The two heme groups are located approximately 15 Å below the P-side of the membrane. Heme a is slightly closer to Cu<sub>A</sub> than heme a<sub>3</sub>. The two hemes are only a few Å apart and only differ by the presence (heme a) or absence (heme a<sub>3</sub>) of a sixth, axial amino acid ligand. This is the position on heme a<sub>3</sub> where oxygen binds before its reduction to water. Adjacent to heme a<sub>3</sub> is Cu<sub>B</sub>: a single copper ion with three histidine ligands. The fourth coordination position is occupied by a reaction product during the oxygen reduction reaction.

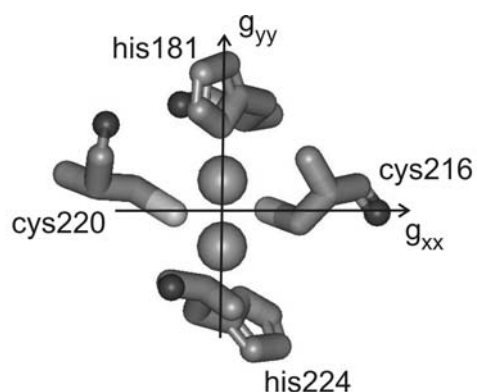


Figure 2.12. Structure of  $\text{Cu}_A$  in CcO of *Paracoccus denitrificans*. The two copper atoms form a plane with the two sulfur atoms from cysteine-216 and cysteine-220, where most (nearly 90%) of the spin density is located when  $\text{Cu}_A$  is in the oxidized  $[\text{Cu}^{1.5+} \dots \text{Cu}^{1.5+}]$  state. The  $g_{xx}$  and  $g_{yy}$  axes lie in the  $\text{Cu}_A$  plane as shown in the figure,  $g_{zz}$  is oriented perpendicular to the  $\text{Cu}_A$  plane [Neese et al. 1996].

Electrons enter CcO exclusively via  $\text{Cu}_A$ , and a patch of negative amino acid residues on subunit II has been described as the main docking site for cyt c [Witt et al. 1998a; Drosou et al. 2002a; Wienk et al. 2003]. From  $\text{Cu}_A$  the electron is transferred to heme a and finally to the binuclear center, consisting of heme  $a_3$  and  $\text{Cu}_B$ , where the reduction of oxygen to water takes place (figure 2.13). Oxygen, which can only bind to the fully reduced binuclear center, is reduced to water in a single fast step, to avoid the production of reactive oxygen species such as hydrogen peroxide.

Two possible proton transfer pathways have been suggested based on crystal structures. They are named after certain critical amino acid residues at the beginning of the channels, the K-channel (for Lys354)<sup>6</sup> and the D-channel (for Asp124). Only one of the two pathways is shown in figure 2.13. The two distinct pathways are probably associated with different parts of the catalytic cycle.

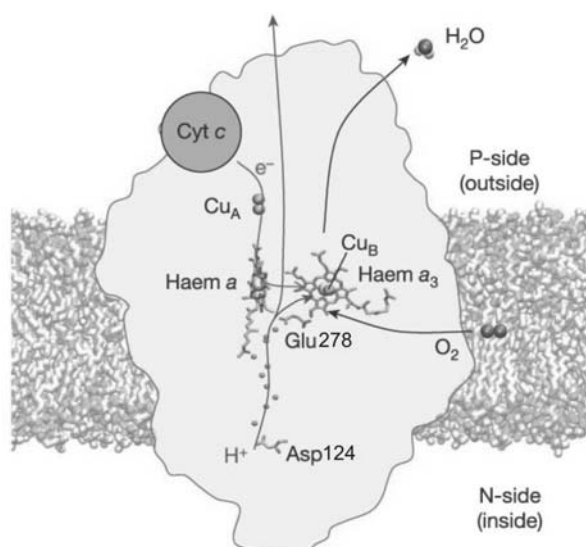


Figure 2.13. The redox-active cofactors, the D-proton-transfer pathway (P.d. numbering) and the reaction catalyzed by cytochrome c oxidase. N and P refer to the two sides of the membrane. Figure adapted from [Faxén et al. 2005].

EPR spectroscopy is an excellent method for studying CcO because of the large number of paramagnetic centers in this enzyme. Several important mechanistic and

<sup>6</sup> *Paracoccus denitrificans* numbering

structural details were clarified with the help of EPR spectroscopy, such as the nature of  $\text{Cu}_A$  (see next section), the surroundings of the  $\text{Mg}^{2+}$  ion [Käss et al. 2000] and the occurrence of a tryptophan radical during enzyme turnover [MacMillan et al. 1999].

### 2.5.2. Binuclear $\text{Cu}_A$ Center

Two types of copper centers are known to participate in ET processes in proteins: the abundant type I, which contains a single copper ion, and the mixed-valence binuclear  $\text{Cu}_A$  center. The  $\text{Cu}_A$  center resembles two type I centers fused together: it consists of two copper ions bound to two cysteine sulfur atoms, to two histidine nitrogen atoms and with two weaker axial ligands, which in CcO are a methionine and the main chain carbonyl oxygen of a glutamine.

The fact that  $\text{Cu}_A$  is a binuclear center was already proposed in 1962 [Beinert et al. 1962], but it took more than 25 years of optical, EPR and EXAFS measurements for convincing evidence to turn up [Kroneck et al. 1988]. The publication of the first high-resolution crystal structure of bacterial CcO several years later [Iwata et al. 1995] erased any remaining doubts. With the detection of the Cu-Cu bond by EXAFS [Blackburn et al. 1994], the structural picture of the  $\text{Cu}_A$  center as it is known today, was complete.

$\text{Cu}_A$  is a highly planar rhomb (figure 2.12) on which the spin density of the unpaired electron in the oxidized form is highly distributed over the sulfur ligands (16-24% spin density each), both copper atoms (15-20%) and the nitrogen ligands (3-5%) [Neese et al. 1996]. Recent ENDOR measurements have shown that the spin distribution reaches far beyond the  $\text{Cu}_2\text{S}_2\text{N}_2$  core, which may be significant for the electron transfer (ET) properties of the center. The reasons for the highly delocalized spin density on  $\text{Cu}_A$  probably include a low reorganization energy upon charge transfer, and the possibility of electrons entering or leaving the center by different pathways [Beinert 1997]. The large metal-metal interaction may serve to shift the redox potential to a range where it can react with its redox partners [Randall et al. 2000].

Unlike type I copper centers,  $\text{Cu}_A$  centers in CcO do not have surface-accessible ligating amino acid residues, but there is evidence that the nearby tryptophan Trp121, whose phenyl side chain sticks out of the protein, plays an important role in transferring the electron from cytochrome *c* to  $\text{Cu}_A$  [Witt et al. 1998b; MacMillan et al. 1999].

The EPR spectrum of  $\text{Cu}_A$  has rhombic symmetry due to the anisotropic *g*-tensor, but the *g*-anisotropy is small and  $g_{xx}$  and  $g_{yy}$  can only be resolved at high microwave frequencies. The spectrum has some features that are quite unusual for copper ions: the *g*-tensor is rhombic,  $g_{xx}$  is smaller than the free electron *g*-value,  $g_{zz}$  as well as the copper hyperfine coupling are quite small, and  $T_1$  was found to be very short [Greenaway et al. 1977]. In addition, it was found that the transverse relaxation of  $\text{Cu}_A$  in CcO shows a peculiar temperature dependence – a feature that was ascribed to dipolar coupling to nearby heme *a*. Attempts to measure this distance accurately by EPR failed [Brudvig et al. 1984; Goodman et al. 1984].

The EPR parameters of  $\text{Cu}_A$  are summarized in table 2.1.

Paramagnetic center	g-values	T <sub>1</sub> (20K) in μs	T <sub>2</sub> (20K) in μs
Cu <sub>A</sub>	2.000, 2.014, 2.189 <sup>a</sup> 1.989, 2.016, 2.2 <sup>b</sup>	5.8 <sup>e</sup>	1.1 <sup>a</sup>
Cyt c <sub>552</sub>	1.1, 2.1, 3.3 <sup>c</sup>	0.26 <sup>c,e</sup>	< 0.2
Cyt c	1.25 2.26 3.06 <sup>d</sup>	0.26 <sup>e</sup>	< 0.2
Heme a	1.49 2.24 3.00 <sup>c</sup>	0.16 <sup>e</sup>	< 0.2
Heme a <sub>3</sub>	2, 6		
Cu <sub>B</sub>	2.06, 2.30 <sup>a</sup> 2.06, 2.20 <sup>f</sup>		

Table 2.1. EPR spectral parameters of paramagnetic centers in cytochrome c oxidase and two different cytochromes

<sup>a</sup> From [Slutter et al. 2001]

<sup>b</sup> Measured by G-band EPR in this study

<sup>c</sup> Measured by A. Weber [Weber]

<sup>d</sup> From [Walker 1999]

<sup>e</sup> Obtained (by extrapolation of data) from [Scholes et al. 1984]

<sup>f</sup> From [Pezeshk et al. 2001]

### 2.5.3. Cytochrome c

The electron transfer between complex III and IV is mediated by the small mobile electron carrier cytochrome c (cyt c, shown in figure 2.14). It contains a heme group covalently bound by two highly conserved cysteine residues. The heme iron is coordinated to four heme nitrogen atoms and two axial ligands: the sulfur atom of a methionine residue and a nitrogen atom of a histidine residue (figure 2.15). During the redox cycle the low-spin iron ion alternates between the diamagnetic reduced (2+) state and the paramagnetic oxidized (3+) state. The heme group is surrounded by many tightly packed hydrophobic side chains, which makes the reduction potential of cyt c more positive.

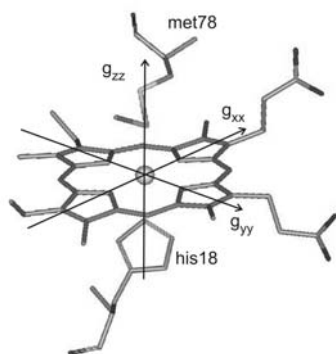


Figure 2.14. NMR solution structure of the soluble fragment of cytochrome c<sub>552</sub> from *Paracoccus denitrificans* [Harrenga et al. 2000] (Pdb file 1QL3). The protein consists of one subunit shown as a ribbon. The heme moiety is shown in stick representation.

The heme group is buried in the protein interior, with only three to five atoms accessible to the solvent at the heme cleft. The heme cleft is surrounded by patches of positive residues that are assumed to contribute to the binding of cyt c to complexes III and IV [Harrenga et al. 2000].

Although the functional part of cyt c is highly conserved among all respiring organisms, there are some small differences in structures of cyt c from various

organisms. The amount of positive charges on cyt *c* varies (being significantly higher in horse heart cyt *c* than in cyt  $c_{552}$  from *Paracoccus denitrificans*, *P.d.*) and mammalian cyt *c* is soluble in water, whereas *P.d.* cyt  $c_{552}$  has a hydrophobic membrane anchor. These subtle differences presumably account for slightly different modes of binding of the cytochromes to the complexes of the respiratory chain.



The low-spin heme iron of cytochrome *c* in its oxidized form has a strongly anisotropic g-tensor ranging from 1 to 3 [Lyubenova et al.; Walker 1999], and see table 2.1. The longitudinal  $T_1$  relaxation of the mitochondrial cytochrome *c* heme iron is mainly caused by a Raman process at temperatures above 3 K [Stapleton et al. 1980] and is very fast, even at low temperatures.

EPR spectral parameters of the three different cytochromes *c* studied in this work are given in table 2.1, the g-tensor axis system is shown in figure 2.15.

Figure 2.15. Structure of heme from *P.d.* cytochrome  $c_{552}$ . The heme iron is ligated by the nitrogen atom of histidine-18 and the sulfur atom of methionine-78. The g-tensor axes system is drawn in the structure [Mailer et al. 1972].

#### 2.5.4. The Binding of Cytochrome *c* to Cytochrome *c* Oxidase

The turnover rate of CcO is limited by the binding of reduced cyt *c* to the enzyme. This demonstrates the dilemma of electron transfer protein-protein complexes, which on the one hand have to be specific so that electron transfer can take place, but on the other hand need to be loosely bound and transient so that the rate of dissociation is high enough. Consequently, the binding interfaces of proteins in electron transfer (ET) complexes tend to be smaller ( $< 1200 \text{ \AA}^2$ ) and include more water molecules than the interfaces between subunits in more tightly bound protein complexes. Also, ET proteins such as cyt *c* are able to bind to different protein surfaces (in this case, complex III and complex IV) and do not have a highly specific binding site. For these reasons, although electrostatic interactions are often important for redox protein association, charged groups are rarely involved in interfacial contacts [Crowley et al. 2004; Prudêncio et al. 2004].

Due to the transient nature of ET protein-protein complexes, only a handful have been crystallized, out of which two structures contain cytochrome *c* [Pelletier et al. 1992; Lange et al. 2002]. Information about dynamics of the protein complexes can be obtained from a combination of NMR measurements and docking calculations, and several structures of ET complexes have been characterized by that method [Prudêncio et al. 2004; Muresanu et al. 2006], sometimes with additional input of results from mutation studies [Bertini et al. 2005]. Docking studies without experimental input were also performed for ET complexes, of which three investigated cyt *c* – CcO interactions [Roberts et al. 1999; Flöck et al. 2002; Flöck et al. 2004]. No ET protein-protein complexes have been successfully investigated by EPR spectroscopy.

As mentioned previously, CcO has a patch of negative charges on the protein surface in the vicinity of Cu<sub>A</sub> and cyt *c* has a ring of positive charges (mainly lysine residues) around the heme cleft. These charges serve to attract and to pre-orient the proteins upon encounter, increasing the number of effective collisions by several orders of magnitude. Evidence for the fact that the general dipole moment is crucial for protein-protein complex formation, rather than individual charge pairs forming upon binding, was found by mutating the negatively charged residues on CcO one by one and comparing catalytic rates [Witt et al. 1998b; Witt et al. 1998a; Maneg et al. 2004].

Based on mutation studies as well as on optical and NMR spectroscopic studies, Ludwig and coworkers proposed a two-step model for the binding of cyt *c* to CcO [Witt et al. 1998b; Wienk et al. 2003; Maneg et al. 2004]. In the first step, the two proteins are attracted by electrostatic interactions and bind loosely, so that in a second step a small structural reorganization leads to the formation of a specific ET complex and an electron is transferred. Docking studies were employed to determine the structure of the specific ET complex [Roberts et al. 1999; Flöck et al. 2002; Muresanu et al. 2006]. In both studies a large number of structures with very similar interaction energies were found. Although the results of these docking studies coincided, the interpretations of the results were rather different: in one case a structure was found that was assumed to be the ET complex [Flöck et al. 2002; Muresanu et al. 2006], whereas in the other case the authors discarded the idea of a single ET structure, saying that the electrostatic forces that orient the proteins are not specific enough to provide a single "lock-and-key" fit [Roberts et al. 1999]. This is also the conclusion of a recent paper by Bertini and coworkers [Bertini et al. 2005], who suggest that cyt *c* docks unspecifically to CcO and moves around on its surface, transferring an electron as soon as the distance between the redox centers is short enough.

#### 2.5.5. Electron Transfer from Cytochrome *c* to Cytochrome *c* Oxidase

According to the Marcus theory [Marcus et al. 1985], the electron transfer rate from one redox group to another depends on the redox potential difference between the involved groups (the free energy), the energy required to adjust the geometry of the redox centers after charge transfer (the reorganization energy) and on the distance *r* between the (edges of the) redox partners. With increasing distance *r*, the electron transfer rate falls off exponentially. As a result, the maximum center-to-center distance for a single-step tunneling through proteins is approximately 20 Å. However, when the position of redox centers and the reaction driving forces are optimal, electrons can "hop" over distances much larger than 20 Å.

After binding of cyt *c* to CcO, the electron transfer from the heme iron to Cu<sub>A</sub> proceeds rapidly (see [Gray et al. 2003] and references therein), even though the distance between the redox centers is expected to be more than 17 Å [Roberts et al. 1999; Flöck et al. 2002]. The electron is, therefore, assumed to hop from the cytochrome heme edge to Cu<sub>A</sub> via a tryptophan residue on subunit II of CcO that has proven to be essential for fast electron transfer between cyt *c* and CcO [Witt et al. 1998b].

From Cu<sub>A</sub> the electron proceeds rapidly to heme a via a pathway that involves the bridging cysteine residues of Cu<sub>A</sub> and several other amino acid residues. The electron

then crosses the 4.5 Å distance between heme a and heme a<sub>3</sub>, either directly or via one or more amino acid residues. In spite of the similarity in Cu<sub>A</sub>-heme a (19.6 Å) and Cu<sub>A</sub>-heme a<sub>3</sub> (22.4 Å) distances, no significant coupling pathways between Cu<sub>A</sub> and heme a<sub>3</sub> seem to exist [Gray et al. 2003].





## Chapter 3. Methods

### 3.1. Relaxation Measurements

The dipolar relaxation method was used for distance measurements. A more straightforward method such as PELDOR was not applicable, because the spectrum of the fast-relaxing spin in the measured systems (the heme iron at both X- and G-band frequency,  $\text{Cu}^{2+}$  at high field) was very broad and the microwave  $B_1$  fields were too small to excite a large enough fraction of spins for a PELDOR experiment.

#### 3.1.1. The G-band Spectrometer

The spectrometer used for all high-field measurements performed for this thesis is a home-built 6.4 T, 180 GHz spectrometer. The details of the setup were published [Rohrer et al. 2001; Hertel et al. 2005] and also appeared in the PhD thesis of Oliver Brüggemann [Brüggemann 2003]. Nevertheless, the setup will be described shortly here.

The spectrometer consists of a superconducting magnet, a high frequency microwave (mw) bridge and a data acquisition system, as shown in figure 3.1. A helium-cooled superconducting magnet from Oxford Instruments produces the external magnetic field, which ranges from 0 - 7 T. A second superconducting coil provides a more easily tunable sweep field of  $\pm 74$  mT. Liquid helium from the magnet cryostat is used for temperature control between 3.3 and 278 K. The temperature at the sample position is regulated by a flow of liquid helium which is pumped from the helium reservoir through a capillary into the sample space where the temperature is adjusted by a heater. Temperature control is performed by an ITC503 temperature controller, but most measurements in this thesis were performed with an extra temperature sensor at the sample position (error < 1K).

A 45 GHz Gunn oscillator is used on the microwave bridge as a master oscillator for driving the transmitter as well as the local oscillator for the sub-harmonic mixer. All switches are driven and synchronized by a pulse generator (Sony/Tektronix DG2020), which is controlled by a home-written LabView program. The exact frequency of the pulses can be monitored by connecting a HP8563 spectrum analyzer to one of the ports of a magic-T. The mw power at 180 GHz, which amounts to 20 mW at the transmitter output, is fed via the quasi-optical circulator into the probehead. The mw power at the sample is approximately 15 mW. Recently, changes were made to the mw bridge that permit double resonance (ENDOR, PELDOR) experiments [Hertel et al. 2005].

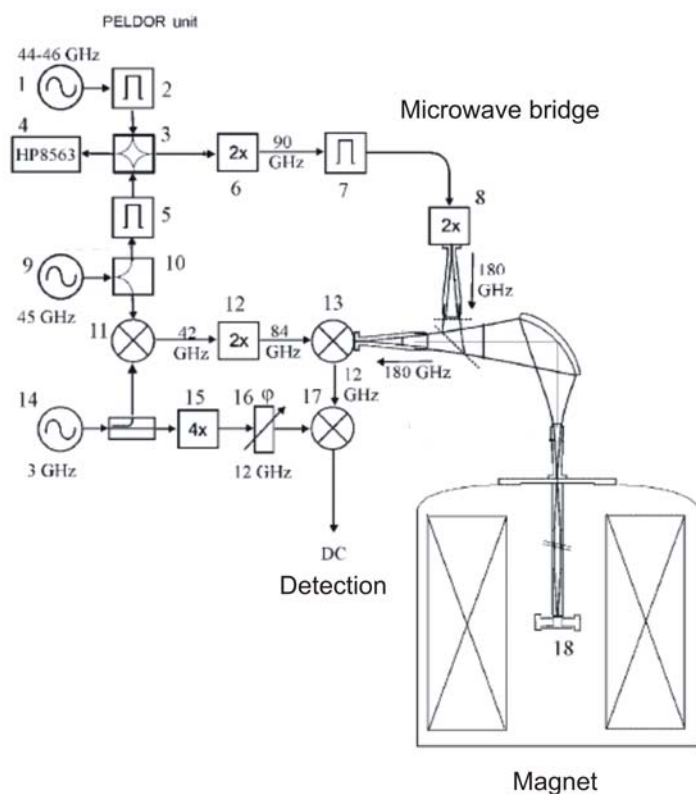
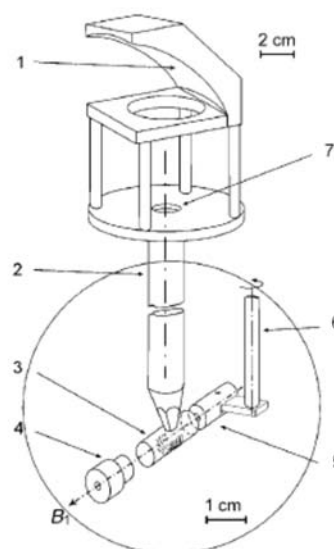


Figure 3.1. Block diagram of the 180 GHz pulse EPR/ENDOR spectrometer. (1) Variable frequency oscillator; (2), (5), (7) fast switches; (3) magic-T; (4) spectrum analyzer; (6), (8), (12) frequency doublers; (9), (14) master oscillators; (10) power divider; (11), (13), (17) mixers; (15) frequency multiplier; (16) phase shifter; (18) resonant cavity. 45 GHz amplifiers are not shown in the figure for simplification. Figure from [Hertel et al. 2005].

The probehead (figure 3.2) is equipped with an elliptical mirror, which reflects the mw radiation through a Teflon vacuum window into a corrugated waveguide with low losses. The waveguide has a tapered end to the cavity that operates in a  $TE_{011}$  mode. The cavity consists of a cylindrical tube of 2.2 mm inner diameter with an iris of 0.4 mm diameter and two plungers. One plunger can be moved with respect to the cavity tube in order to tune the cavity to critical coupling during measurements. The other plunger is screwed to a fixed position. The sample is placed in a suprasil capillary (Rotatec Spintec) of 0.4 mm inner diameter and passed through the hole in the fixed plunger so that the cavity is filled with sample. Without taking the magnetic field distribution into account, the filling factor is 0.2. The quality factor  $Q$  of the filled resonator is approximately 1000.

Figure 3.2. 180 GHz EPR probehead. (1) Elliptical mirror; (2) corrugated waveguide; (3) resonant cavity; (4) fixed plunger; (5) moveable plunger; (6) driving rod; (7) Teflon vacuum window. Figure from [Hertel et al. 2005].



### 3.1.2. G-band Measurements

Dipolar relaxation times were obtained by applying the Hahn echo sequence and detecting the intensity of the echo signal as a function of increasing pulse separation time  $\tau$ , as illustrated in figure 2.5.a. Typical values of experimental parameters are: pulse lengths 35-50 ns ( $\pi/2$ ) and 70-100 ns ( $\pi$ ); pulse spacing  $\tau$  in field-swept experiments or  $\tau_{\text{start}}$  for time-dependent measurements 200 ns; repetition time 0.1 -30 ms depending on sample and temperature; magnetic field of the main coil was typically 6.422 T; sample temperature 5-35 K (cytochrome *c* / cytochrome *c* oxidase) or 5-120 K ( $\text{Cu}^{2+}$ -OEP-TPA and  $\text{Mn}^{2+}$ -terpyridine-TPA). Inversion recovery experiments were performed with a 100 ns inversion pulse, followed after at least 600 ns by a typical Hahn-echo detection sequence (see also appendix B).

Field-swept spectra were recorded with different  $\tau$  values to study relaxation anisotropy. If less than the whole range of the sweep coil was used (i.e. when measuring nitroxide spectra) the magnetic field was stepped slowly to -70 mT and then slowly to the starting field value, in order to avoid errors due to hysteresis effects of the sweep coil.

The full field-swept spectra of  $\text{Cu}_A$  and  $\text{Cu}^{2+}$  could only be obtained by sweeping the magnetic field of the main coil, due to the limited range of the sweep coil (148 mT). For these measurements, the echo intensity was recorded while the field of the main coil was swept. The high-field spectrometer control program has no procedure to perform main-field sweep measurements, therefore they were done as follows: the magnetic field was programmed manually to decrease (or increase) from the starting field value to the end field value with a certain speed (usually 15 mT  $\text{min}^{-1}$ ). Meanwhile, the echo signal was monitored by the program by running a "1D experiment with static magnetic field", keeping the trigger and the pulses constant, but moving a virtual pulse that was far out of the detection area. In this fashion spectra were taken that were linearly dependent on  $B_0$ , but of which the magnetic field value was only known for the first and the last point. The intermediate field positions were determined by interpolation, the linearity of the field sweep was verified by spectral simulation, see figure 3.3.

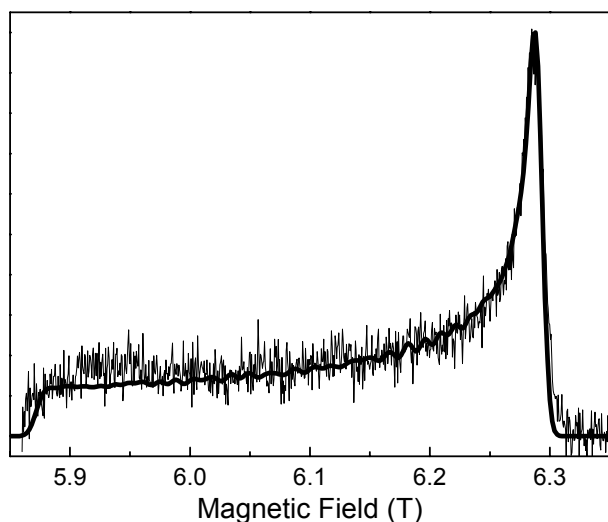


*Figure 3.3. Echo-detected field-swept spectrum of  $\text{Cu}^{2+}$  measured at G-band by means of a main field sweep. The thick noiseless line is a simulation with  $g_{\parallel} = 2.18$  and  $g_{\perp} = 2.044$  and a homogeneous line width of 7 mT. Experimental parameters: Hahn echo sequence with pulse lengths 40 ns and 80 ns;  $\tau = 200$  ns; repetition time 15 ms; temperature 10 K; main magnetic field sweep from 6.450 T – 5.850 T at 1.5 mT  $\text{min}^{-1}$  and 1000 data points.*

The extended sweep-coil sweep was performed by sweeping the sweep coil while the main coil was connected to its power supply and the switch heater was on. The range of this field-sweep method is about three times larger than that of a normal field sweep. This is most probably due to the inductive coupling of sweep coil and main coil; the main coil is kept at a fixed magnetic field value by the power supply, not at a constant current like in the superconducting loop operation. The extended sweep-coil sweep is linear (figure 3.4), but the magnetic field axis needs to be rescaled by a factor of 3.077, as was found by measurement of a  $\text{Mn}^{2+}$  in MgO standard.

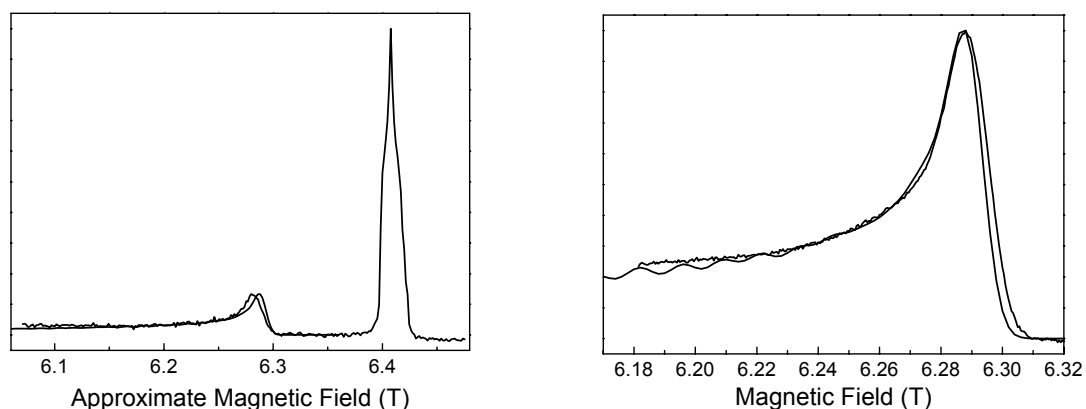


Figure 3.4. Comparison of an "extended sweep-coil sweep" (left) and a normal field-swept spectrum (right) of  $\text{Cu}^{2+}$ -NO. In the left figure, the nitroxide spectrum can be seen as well as part of the  $\text{Cu}^{2+}$  spectrum, whereas in the right figure only  $\text{Cu}^{2+}$  is seen. The simulation of the  $\text{Cu}^{2+}$  spectra, given in the figures by the solid, noiseless line, is the same as shown in figure 3.3. Experimental parameters: (left) Hahn echo pulse lengths 40 ns and 80 ns;  $\tau = 200$  ns; repetition time 15 ms; temperature 10 K; switch heater on, main magnetic field at  $B_0 = 6.300$  T and sweep coil swept from -74.5 mT to +74.5 mT. The sample concentration is approximately 0.2 mM. (right) Hahn echo pulse lengths 50 ns and 100 ns;  $\tau = 200$  ns; repetition time 35 ms; temperature 5.5 K; main magnetic field at 6.260 T and sweep coil swept from -74.5 mT to + 74.5 mT.

## 3.2. Sample Preparation

The synthesis and preparation of samples was performed by M.K. Siddiqui (cytochrome *c* – cytochrome *c* oxidase project) and J. Plackmeyer (Cu<sup>2+</sup>-OEP-TPA, Ni<sup>2+</sup>-OEP-TPA and Mn<sup>2+</sup>-terpyridine-TPA). Details of the protein preparations are given in [Lyubenova et al.; Siddiqui 2006], the synthesis of the model systems, performed by J. Plackmeyer will be published shortly [Plackmeyer et al.]. A short description of the samples and further preparation is given in this section.

### 3.2.1. Cytochrome *c* Oxidase

As a model system to test our experimental setup and our method of analysis, distance measurements were performed to determine the (known) distance between Cu<sub>A</sub> and heme *a* in the fully functional four-subunit containing cytochrome *c* oxidase. The manganese-free preparation contained four paramagnetic centers: Cu<sub>A</sub>, Cu<sub>B</sub>, heme *a* and heme *a*<sub>3</sub>. Normally only Cu<sub>A</sub> and heme *a* are visible by EPR, because Cu<sub>B</sub> and heme *a*<sub>3</sub> are strongly exchange-coupled and form a *S* = 2 center that relaxes extremely fast [Tweedle et al. 1978].

Approximately 1 mM of CcO was dissolved in a 5 mM HEPES buffer with 10% glycerol and *n*-dodecyl maltose as a detergent.

### 3.2.2. Cytochrome *c* and Cytochrome *c* Oxidase

The interactions between cytochrome *c* oxidase (CcO) from *Paracoccus denitrificans* (*P.d.*) and various cytochromes were studied. Manganese-free CcO contains four paramagnetic centers, as mentioned previously. As the purpose of this work was to determine the distance between two paramagnetic centers, the soluble part of subunit II of CcO (from here on termed CcO<sub>II</sub>), which contains Cu<sub>A</sub> as only paramagnetic center, was used in a first approach. Electron transfer from cytochrome *c* is known to occur to this model system [Lappalainen et al. 1993], and has spectroscopic properties that are very similar to that of Cu<sub>A</sub> in CcO [Lappalainen et al. 1993; Maneg et al. 2003].

Three different cytochromes were studied. Cytochrome *c*<sub>552</sub> from *P.d.* (referred to in this work as *c*<sub>552</sub>) is the native substrate of CcO [Reincke et al. 1999]. The measurements were done in solution, and to make the protein soluble in water, the membrane anchor of *c*<sub>552</sub> was removed. This truncated cytochrome is known to be capable of electron transfer to CcO [Drosou et al. 2002b]. Cytochrome *c* from horse heart (*c*<sub>hh</sub>) is also known to transfer electrons to CcO from *P.d.* with a high turnover rate [Drosou et al. 2002b], whereas cytochrome *c*<sub>1</sub> (*c*<sub>1</sub>) from Complex III of *P.d.* does not transfer electrons to CcO [Janzon] and is used as a negative control to our measurements.

The high-resolution structures of CcO<sub>II</sub> and the three cytochromes [Bushnell et al. 1990; Iwata et al. 1995; Reincke et al. 2001; Lange et al. 2002] are given in figure 3.5. The surface of CcO<sub>II</sub> near Cu<sub>A</sub> has a net negative charge, presumably to guide the cytochrome to its docking position (see [Maneg et al. 2004] and references therein). Cytochromes *c*<sub>552</sub> and *c*<sub>hh</sub> are dipoles with a net positive charge around the heme cleft,

where the electron is proposed to leave the cytochrome. The net negative charge on cytochrome  $c_1$  is thought to prevent binding to  $CcO_{II}$ .

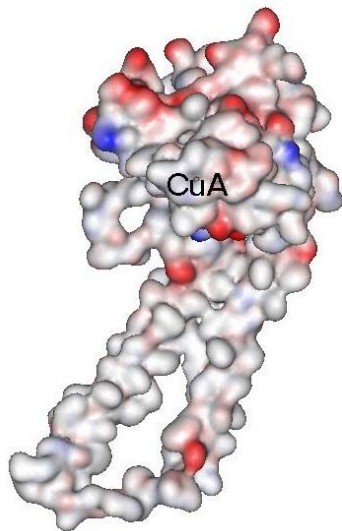


Figure 3.5.a. Surface plot of structure of subunit II of  $CcO$ . The figure was colored according to the charge (blue, positive; red, negative) on the amino acid residues and some important residues around the presumed cytochrome  $c$  binding site. The position of the  $Cu_A$  site is labelled "CuA". Pdb file 1ar1, figure prepared with WebLab ViewerPro.

The relevant EPR spectral parameters of  $Cu_A$  and of the three different cytochromes are given in table 2.1. The short relaxation times [Scholes et al. 1984] and broad spectra of the heme irons of all three cytochromes make EPR detection at G-band impossible. Most of the  $Cu_A$  spectrum lies outside the sweep range of the sweep coil, due to the large spectral width of the  $CcO_{II}$  signal. When the main magnetic field is set to 6.422 T (corresponding to  $g = 2.00$  for  $\nu = 180$  GHz), only the spectral region around  $g_{xx}$  and  $g_{yy}$  can be measured, which is the reason that anisotropy measurements have been performed mainly at these positions.

Sample concentrations of 0.2 up to 0.75 mM of both cytochrome and  $CcO_{II}$  were necessary due to the low intensity of the  $Cu_A$  signal at G-band. The samples were buffered by 5 mM HEPES buffer, and 10% glycerol was added to form a good glass during freezing. The final concentrations of some samples were checked by UV-vis absorption spectroscopy, measuring the absorption of the samples at 552 nm ( $\epsilon_{552} \sim 10$   $\text{mM}^{-1}\text{cm}^{-1}$ ).

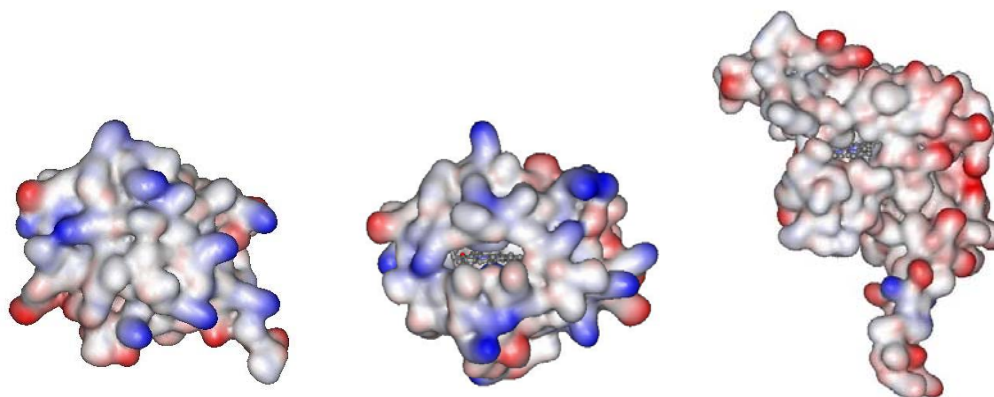


Figure 3.5.b. Surface representation of the soluble part of *Paracoccus denitrificans* cytochrome  $c_{552}$  (left), horse heart cytochrome  $c_{550}$  (center) and *P.d.* cytochrome  $c_1$  (right). The surface is colored according to the charge on the amino acids. The heme moiety in all proteins has approximately the same orientation and is shown in ball-and-stick representation. The molecules are not drawn on the same length scale.

Pdb entry 1QL3 ( $c_{552}$ ), 1hrc ( $c_{550}$ ), 1KY0( $c_1$ ). The figures were prepared with WebLab ViewerPro.

### 3.2.3. Ni<sup>2+</sup>-orthoethylporphyrin-TPA and Cu<sup>2+</sup>-orthoethylporphyrin-TPA

The structure of Cu<sup>2+</sup>-orthoethylporphyrin-TPA (from here on referred to as Cu<sup>2+</sup>-NO·) is shown in figure 3.6. The molecule was designed and synthesized for PELDOR measurements and consists of two non-identical spins connected by a rigid linker. Free rotation is expected around the triple bonds and the bonds connecting the triple bond to the nitroxide moiety and to the porphyrin respectively. The crystal structure of the nickel(II) analogue (figure 3.7) shows that there is a slight flexing of the molecule possible, so that the interspin axis may bend up to ca. 10° with respect to the interspin axis when the molecule is in the extended form. The distance between the nitroxide oxygen and the metal ion is 2.2 nm, the interspin vector makes an angle of 90° with the g<sub>zz</sub> axis of the nitroxide and 36° with the g<sub>xx</sub> axis. The distance between the paramagnetic centers was confirmed by X-band PELDOR measurements, and an exchange coupling of approximately 2.5 MHz was found [Bode].

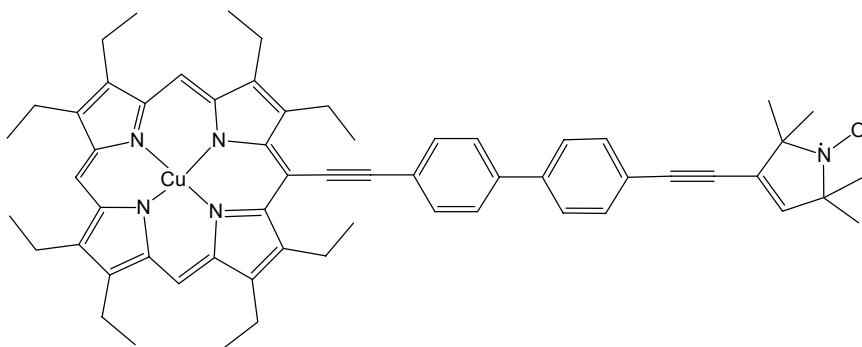


Figure 3.6. Structure of Cu<sup>2+</sup>-OEP-TPA. Figure created with ChemDraw Ultra 6.0.

Small amounts of Cu<sup>2+</sup>-NO· or Ni<sup>2+</sup>-NO· were initially dissolved in ortho-terphenyl (otp) and then measured. The end concentration was 0.026% w/w. To avoid stacking of the porphyrin rings, methylimidazole (MeIm) or pyridine was added which ligated to the metal ions. Subsequent measurements were also performed with the sample dissolved in a 3:7 mixture of chloroform and toluene or fully deuterated toluene, or in tetrahydrofuran (THF), always with an excess of either MeIm or pyridine. The concentration of these Cu<sup>2+</sup>-NO· or Ni<sup>2+</sup>-NO· samples was 0.1 mM.

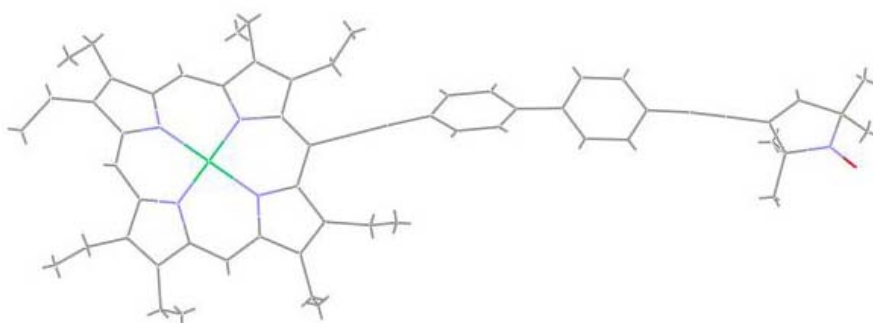


Figure 3.7. Crystal structure of Ni<sup>2+</sup>OEP-TPA [Plackmeyer et al.]. Notice the bend in the molecule. Figure created with Mercury 1.4.1.

### 3.2.4. $Mn^{2+}$ -terpyridine-TPA

The structure of  $Mn^{2+}$ -terpyridine-TPA ( $Mn^{2+}$ -NO $\cdot$ ) is shown in figure 3.8. Like  $Cu^{2+}$ -NO $\cdot$ , it was developed for PELDOR measurements. The rigid linker is almost the same as the one in  $Cu^{2+}$ -NO $\cdot$ , except for the ester bond to TPA that takes the place of a triple bond. In the  $Cu^{2+}$ -NO $\cdot$  molecule, substituting the triple bond by an ester bond was found to decrease the value of exchange coupling  $J$  from 2.5 MHz to approximately 0 [Bode]. The only bond that has free rotation is the triple bond. The ester oxygen atom, the carbonyl carbon and the neighboring carbon atom lie in an inflexible plain. There was no diamagnetic analogue of  $Mn^{2+}$ -NO $\cdot$  available, therefore the terpyridine-TPA ligand without ligating metal ion was used as a control system.

$Mn^{2+}$ -NO $\cdot$  was dissolved in dimethylformamide (DMF) to a concentration of 5 mM and mixed with a nine fold excess of toluene to ensure good glass formation. The end concentration of the 1:9 DMF:toluene solution was 0.5 mM  $Mn^{2+}$ -NO $\cdot$ .

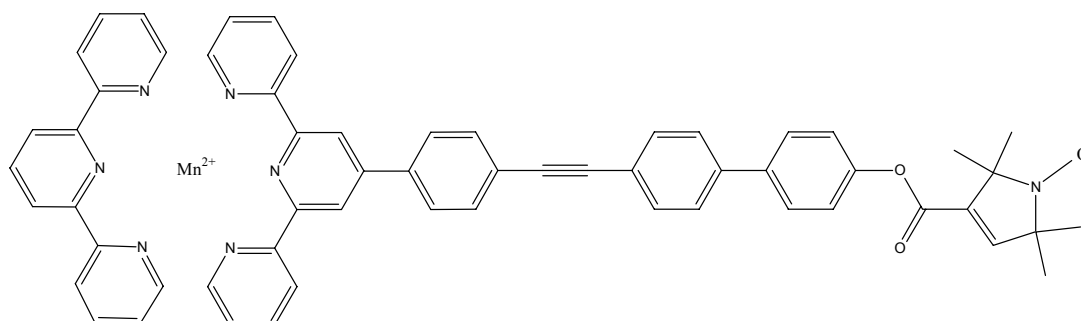


Figure 3.8. Structure of  $Mn^{2+}$ -terpyridine-TPA. The terpyridine units are perpendicular to each other so that the  $Mn^{2+}$  orbitals have octahedral symmetry. Figure created with ChemDraw Ultra 6.0.



### 3.3. Simulation Program

Two simulation programs were used in this thesis. HEdipolar is a program to calculate the dipolar relaxation traces for any field position in a spectrum taken at any microwave frequency. The other program, statdiprelax, calculates the dipolar relaxation traces induced by a certain concentration of fast-relaxing spins distributed randomly in a sample. Both programs were home-written by T.F. Prisner in MatLab (The Mathworks) code. The codes of the HEdipolar program with its subprograms, as well as the code of the statdiprelax program are given in appendix A.

#### 3.3.1. The Program HEdipolar

The program that was used to simulate and fit data from relaxation measurements is capable of simulations in one dimension (relative echo intensity vs. time) and in two dimensions (relative echo intensity vs. time and magnetic field) and of fitting sets of 1D relaxation data gathered at different temperatures for any microwave frequency and for any field position in the EPR spectrum.

The simulation procedure performed the following steps, also schematically shown in scheme 3.1:

Step 1. The spectrum of the slow-relaxing observer spin (A) is calculated. This is done using a procedure that calculates the resonance frequencies for a certain number of orientations on a sphere given by the user, taking into account electron Zeeman and hyperfine contributions. The obtained spectrum is folded with a Lorentzian line shape of a user-given homogeneous line width. The orientations corresponding to the different field positions in the spectrum are saved for use in the second step.

Step 2. In the 1D case, the user is asked which position in the spectrum the simulation should be performed at, and the corresponding orientations are selected for the consecutive calculation. In the 2D case, echo decay traces are calculated for each magnetic field position with intervals as large as the step width of the magnetic field axis. All resonances of spins that fall within the step width at a particular value of the magnetic field are taken into account for the calculation of the echo decay trace at that position in the EPR spectrum.

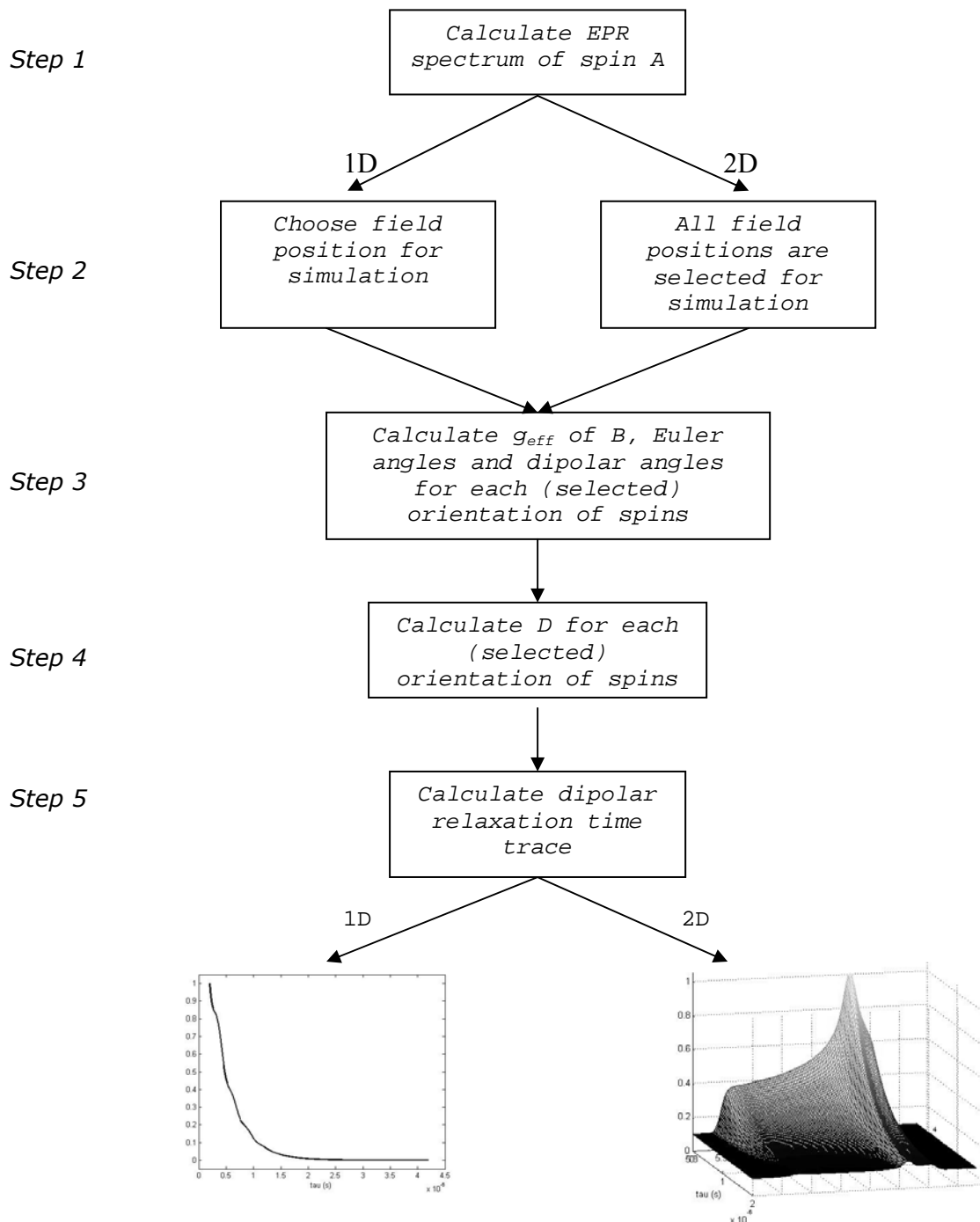
Step 3. For each orientation of the observer spin selected in step 2 the effective  $g$ -value of the fast-relaxing coupled spin (B) is calculated using the  $g$ -values of spin B and the Euler angles  $\alpha$ ,  $\beta$  and  $\gamma$  that determine the orientation of the  $g$ -tensor of spin B with respect to the  $g$ -tensor of spin A. The effective  $g$ -value of spin A is approximated by  $g_{yy}$  for all positions in the spectrum. The dipolar angles are defined in the program with respect to the  $g$ -tensor of the A spin. For each selected orientation of the spin in the magnetic field, these angles are transformed to the dipolar angles  $\theta_D$  and  $\phi_D$  between the dipolar axis and the external magnetic field.

Step 4. The effective  $g$ -values and dipolar angles calculated in step 3 are used to calculate the dipolar coupling (see section 2.1.4) for each individual orientation selected in step 2.

Step 5. From the dipolar coupling values obtained in step 4 the dipolar relaxation enhancement trace is calculated point by point using

$$\Phi_{\text{dip}}(2\tau) = R^{-2} \left[ \frac{k}{2} ((k+R)\exp(-(k-R)2\tau) + (k-R)\exp(-(k+R)2\tau)) + \Delta^2 \exp(-k2\tau) \right] \quad \{3.1\}$$

where  $k = 1/T_{1f}$  and  $R = \sqrt{k^2 - \Delta^2}$ . This formula is equivalent to equation 2.14 in the theory chapter.



Scheme 3.1. Sequence of steps executed by the computer program used to simulate dipolar relaxation echo decay traces. See the text for details.

The fit program follows the same procedure, adjusting the fit parameters used for calculation of the dipolar coupling  $\Delta$  in step 4 within the boundaries given by the user to minimize the mean square deviation from the experimental data. The fit parameters are varied according to a SIMPLEX or a sequential quadratic programming algorithm, both implemented in MatLab. The fit parameters were one or more of the following parameters: the interspin distance  $r$ , the dipolar angles  $\theta_D$  and  $\phi_D$ , the Euler angles  $\alpha$ ,  $\beta$  and  $\gamma$ , the exchange coupling  $J$ , an offset and a  $T_1$  factor for each temperature that takes into account errors in measured  $T_1$  or temperature. In table 3.1 the fit parameters for a typical fit of cytochrome  $c$  – cytochrome  $c$  oxidase dipolar relaxation data is given.

The HEdipolar program was tested with the help of dipolar relaxation data published previously by Eaton and coworkers [Budker et al. 1995]. Using the structural and relaxation parameters given in the paper for the spin-labeled hemoglobin, we were able to reproduce the experimental results very well. It must be mentioned, however, that the orientation dependence of dipolar relaxation could not be tested in this fashion, because Eaton and coworkers were not able to detect any relaxation anisotropy at X-band.

Parameter	Name in program	Units	Upper boundary	Lower boundary
$r$	R	nm	2.5	1.5
$\theta_D$	thetaD	degrees	90	0
$\phi_D$	phiD	degrees	90	0
$\alpha$	gangles(1)	degrees	90	0
$\beta$	gangles(2)	degrees	90	0
$\gamma$	gangles(3)	degrees	90	0
$J$	J	Hz	$10^7$	$-10^7$
offset	offset	-	0.2	0
$T_1$ factor	T1factor	-	2	0.5

Table 3.1. Typical parameters for a fit of cytochrome  $c$ –cytochrome  $c$  oxidase dipolar relaxation data

### 3.3.2. Sensitivity of HEdipolar to Simulation Parameters

The simulations performed by HEdipolar were very sensitive to various parameters. At low temperature, where  $T_1$  of the fast-relaxing spin,  $T_{1f}$ , is large, the simulated echo decay traces only depend on  $T_{1f}$ . For  $T_{1f} < 1 \mu\text{s}$  the signal decay was strongly dependent on the distance  $r$  and on the exchange coupling  $J$  (shown in figure 3.9). The echo decay traces were simulated at the maximum ( $g_{yy}$ ) of the G-band  $\text{Cu}_A$  spectrum, and it can be seen by the non-exponential decay that spins experiencing different dipolar coupling strengths contribute to the signal. In figure 3.10 dipolar relaxation traces are shown where the dipolar angles  $\theta_D$  and  $\phi_D$  (left figure) or the Euler angles  $\alpha$ ,  $\beta$ , and  $\gamma$  (right figure) were stepped from  $-90^\circ$  to  $90^\circ$  in  $10^\circ$  steps. The angles influence the shape of the relaxation traces and the size of the offset. The field-swept G-band spectra of  $\text{Cu}_A$  were very sensitive to different parameters as well. Shown in figure

3.11 is the dependence of the field-swept spectrum at  $\tau = 200$  ns on the exchange coupling  $J$ . The exchange coupling shifts the dipolar pattern (as illustrated in figure 3.12), and consequently, a point in the spectrum experiencing dipolar coupling when  $J = 0$  MHz may sense less or no dipolar coupling when  $J = 10$  MHz (such as  $g_{zz}$  in figure 3.11).

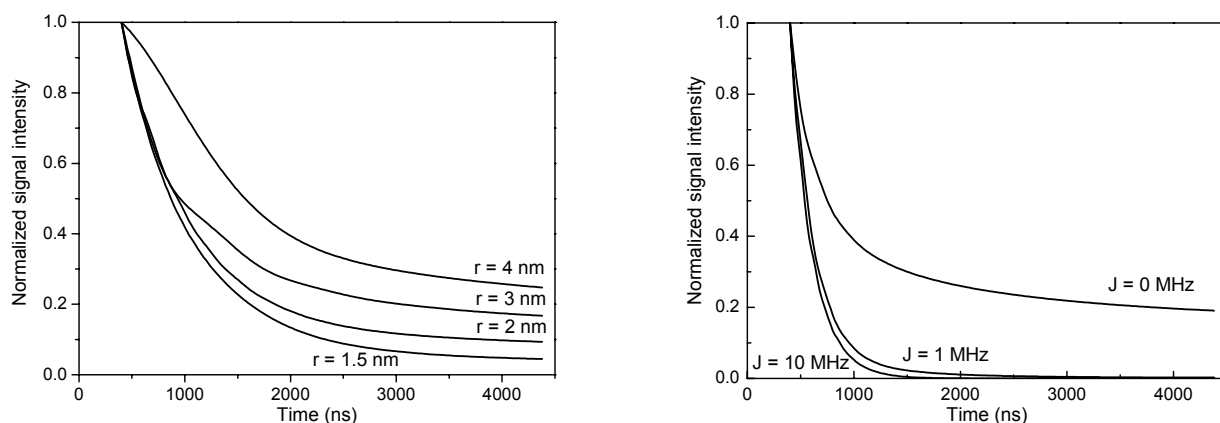


Figure 3.9. Sensitivity of dipolar relaxation simulations to distance  $r$  (left) and to the exchange coupling  $J$  (right). G-band simulations of  $\text{Cu}_A$  relaxation at the  $g_{yy}$  spectral position due to the presence of horse heart cytochrome  $c$ . Simulation parameters left:  $r$  varied as given in the plot, dipolar and Euler angles  $0^\circ$ ,  $J = 0$  MHz, offset  $0\%$ ,  $T_{1f} = 0.8 \mu\text{s}$ . Simulation parameters right:  $r = 2$  nm,  $J$  varied as given in the plot, all other parameters as above.

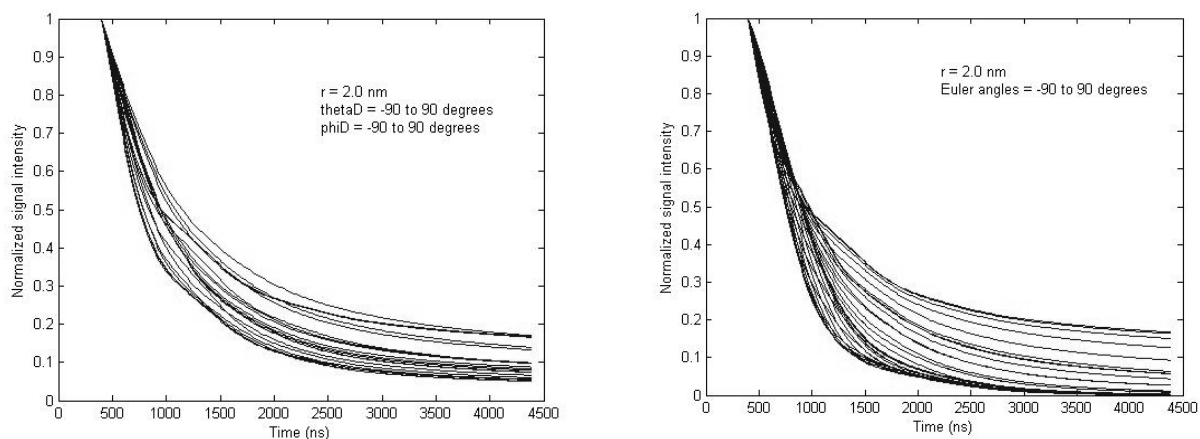


Figure 3.10. Sensitivity to parameters: variation of the dipolar angles (left) and variation of the Euler angles (right). G-band simulations of  $\text{Cu}_A$  relaxation at the  $g_{yy}$  spectral position due to the presence of horse heart cytochrome  $c$ . Simulation parameters:  $r = 2$  nm,  $T_{1f} = 0.8 \mu\text{s}$ ; the angles that were not varied were set to  $0^\circ$ , offset =  $0\%$ .

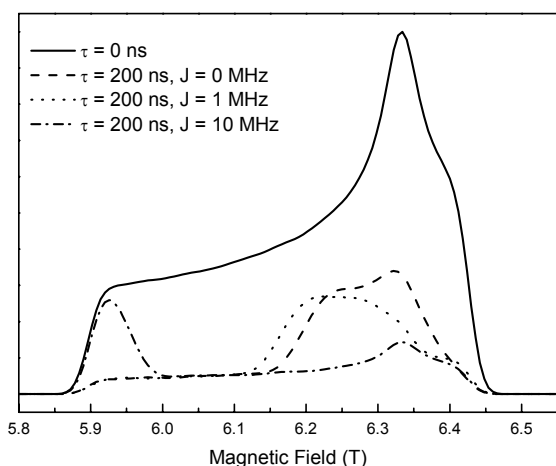
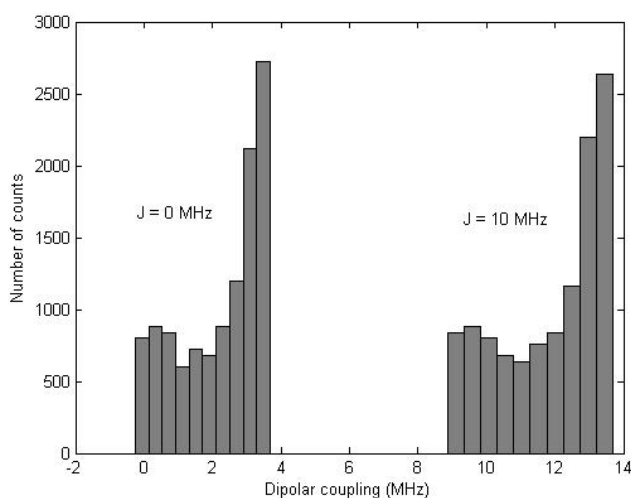


Figure 3.11. Sensitivity of simulated field-swept spectra to the exchange coupling  $J$ . Parameters the same as given for the right plot in figure 3.9.

Figure 3.12. Distribution of dipolar coupling at the  $g_{yy}$  position of  $\text{Cu}_A$  due to the presence of  $c_{hh}$  with the following simulation parameters:  $r = 2 \text{ nm}$ , all angles =  $0^\circ$ ,  $J = 0$  or  $10 \text{ MHz}$ , as indicated in the figure. Introducing exchange coupling shifts the dipolar coupling frequency, but hardly changes the shape of the dipolar pattern.



### 3.3.3. The statdiprelax Program

The dipolar relaxation enhancement of randomly distributed fast-relaxing spins B on slow-relaxing spins A can be calculated by equation {2} in the paper by Salikhov, Dzuba and Raitsimring [Salikhov et al. 1981]. However, this formula is only valid if  $\tau \ll T_{1f}$ . We are also interested in the region where the formula does not hold, and therefore a more extensive calculation is required.

The statdiprelax program separates the calculation of the decay caused by B spins that are relatively far from the A spin and that doesn't need to be treated implicitly, and decay caused by B spins that are closer to the A spin.

The input parameters for the statdiprelax program are: the magnetic field  $B_0$ , the concentrations of the A and B spins, the radii of the respective molecules containing the A and B spins,  $T_{1f}$  and the g-tensor of fast-relaxing spin B. The g-tensor of spin A was set to the isotropic value of 2. The sample, or "box" size that is taken into account in the calculations (Xbox), the maximum interspin distance that is calculated accurately (rmax) and the number of runs of the program (kstat) can be varied, but were kept constant at Xbox = 60 nm, rmax = 17 nm, and kstat = 2000. Smaller values caused inaccurate results.

The first step taken by the program is to calculate the dipolar relaxation caused by B spins that are relatively far (further than rmax) from the A spin. This is done using the following equation:

$$1/T_2^{\text{dip}} = nT_{1f} \left( \frac{\pi K_{\text{dip}} g_A^{\text{eff}} g_B^{\text{eff}}}{r_{\text{max}}^3} \right)^2 \quad \{3.1\}$$

where  $K_{\text{dip}} = \frac{\beta_e^2}{h}$  and n is the amount of B spins in the sample. The effective g value of the A spin is assumed to be 2 in all calculations, the effective g value of spin B was calculated for every possible orientation of the B spin g-tensor. The resulting echo decay traces are saved and added later to the dipolar relaxation traces from the B spins that are at a distance smaller than rmax to the A spin.

The calculation of the dipolar relaxation enhancement due to "close" B spins is more extensive. The spherical molecules containing the A spins or the B spins are placed successively in a cubic box whose dimensions are given by the parameter Xbox. The molecules are allowed to come very close to each other, but may not overlap. This is a very time-consuming step. Subsequently, the B spins are selected that fall within the boundary given by rmax. For each of these B spins the dipolar coupling to one A spin is calculated, from which the dipolar relaxation enhancement is computed using equation {3.1}. The resulting echo decay traces are summed and added to the decay traces resulting from dipolar coupling to the "far" spins. This procedure is then repeated a number of kstat times. The sum of all calculated echo decay traces is then normalized to the first point.



## Chapter 4. Cytochrome c and Cytochrome c Oxidase

### 4.1. Results

The binding of cytochrome c to cytochrome c oxidase was studied by measuring the effect of dipolar coupling by cytochrome c on the transverse relaxation of  $\text{Cu}_A$ . First, the EPR spectrum and relaxation behavior of  $\text{Cu}_A$  were studied in detail, because these were not measured before at G-band frequency. Subsequently, the relaxation enhancement of  $\text{Cu}_A$  by the nearby heme a was studied as a test of our method: the purpose of the high-field measurements was to detect relaxation anisotropy and this had never before been directly detected.

Finally, dipolar relaxation measurements were performed on mixtures of  $\text{Cu}_A$  with three different cytochromes c: two cytochromes ( $c_{552}$  and  $c_{hh}$ ) that form functional electron-transfer complexes with  $\text{CcO}$ , and one ( $c_1$ ) that did not form a complex with  $\text{CcO}$  was used as a negative control. Similar measurements were performed in X-band by S. Lyubenova [Lyubenova et al.], and the G-band results will be compared with those obtained at X-band frequency.

#### 4.1.1. Measurements of $\text{Cu}_A$ in $\text{CcO}_{II}$

$\text{Cu}_A$  in the soluble part of subunit II of *Paracoccus denitrificans*  $\text{CcO}$  ( $\text{CcO}_{II}$ ) was studied. Its field-swept spectrum was measured by integrating the Hahn echo while sweeping the main magnetic field. It is shown in figure 4.1, together with a spectrum measured at X-band. In contrast to X-band frequency, at high frequencies ( $> 95$  GHz) the  $\text{Cu}_A$  spectrum is fully resolved and the  $g_{xx}$ ,  $g_{yy}$ , and  $g_{zz}$  values can be read directly from the spectrum. The field-swept spectrum of  $\text{Cu}_A$  around  $B_0 = 6.422$  T is shown in figure 4.2. This spectrum was simulated with  $g$ - and hyperfine values that agree very well with those found previously by W-band EPR [Slutter et al. 2001].

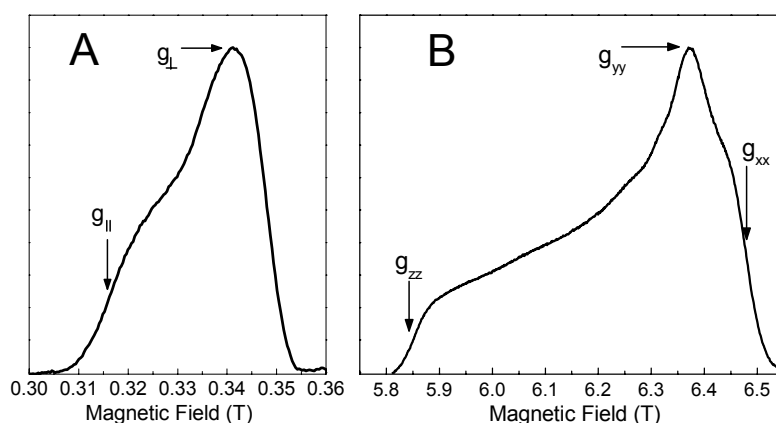


Figure 4.1. Field-swept echo detected EPR spectra of the oxidized mixed-valence binuclear  $\text{Cu}_A$  center in  $\text{CcO}_{II}$ : A) X-band frequency (9.72 GHz), 0.1 mM  $\text{CcO}_{II}$ ,  $T = 15$  K, pulse separation  $\tau = 120$  ns, from [Lyubenova et al.]; B) G-band frequency (180 GHz), 3 mM  $\text{CcO}_{II}$ ,  $T = 5$  K, pulse separation  $\tau = 300$  ns, main field sweep. The canonical orientations are shown by arrows.



The  $g_{zz}$  value could not be determined to high precision at G-band, because the spectra obtained by sweeping the main magnetic field have no accurate magnetic field axis, as explained in chapter 3.

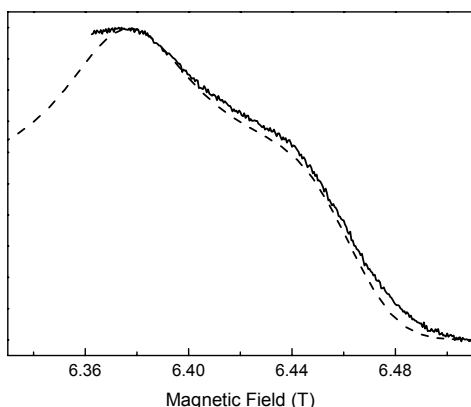


Figure 4.2. Field-swept echo detected EPR spectrum of  $Cu_A$  in  $CcO_{II}$  at G-band frequency (180 GHz). 0.2 mM  $CcO_{II}$ ,  $T = 10$  K, pulse separation  $\tau = 200$  ns, main field set to 6.422 T. Simulation (dashed line) of G-band spectrum:  $g = (1.989, 2.0160, 2.189)$ , hyperfine tensor (23, 25, 37) G, isotropic line width 200 G.

The  $Cu_A$  spectrum is very broad at G-band (approximately 0.7 T) due to  $g$ -anisotropy. In order to perform measurements above 15 K, the sample concentration needed to be at least 0.2 mM. The measurements at X-band, described in [Lyubenova et al.], were all performed with a protein concentration of 0.1 mM. The increase in  $Cu_A$  relaxation rate due to the higher protein concentration was negligible, and the effect on the dipolar relaxation measurements was also small (see section 4.1.3).

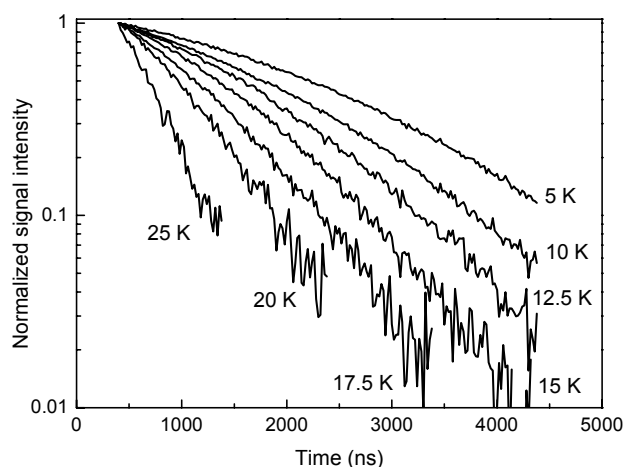


Figure 4.3. Echo decay traces of 0.75 mM  $CcO_{II}$  at various temperatures as indicated in the plot. Measurements performed at the  $Cu_A$  signal maximum ( $g_{yy}$ ). Experimental parameters as given in chapter 3.

The relaxation of  $Cu_A$  at the  $g_{yy}$  spectral position was studied at G-band frequency as a function of temperature for different  $CcO_{II}$  concentrations. Echo decay traces of  $Cu_A$  between 5 and 25 K are shown in figure 4.3. The echo decay traces at low temperature ( $T < 20$  K) were well described by a stretched exponential function ( $\exp\{(-2\tau/T_2)^a\}$ , with  $1 \leq a \leq 1.6$ ). At G-band, at higher temperatures the echo decay traces showed single exponential behavior. This corresponds to a single process dominating the transverse relaxation, or the product of several exponential processes. The  $T_2$  values derived from such temperature-dependent experiments of samples with varying  $CcO_{II}$  concentrations are shown in figure 4.4.

At 5 K the transverse relaxation times of  $Cu_A$  at X-band and G-band are equal, but at higher temperatures the relaxation at G-band becomes significantly faster. This behavior cannot be explained by the difference in sample concentration (typically 0.1 mM at X-band, 0.2 mM at G-band). There is no significant difference between the relaxation times at G-band for samples with a concentration of 0.2 or 0.3 mM, but increasing the

concentration to 0.75 or even 1 mM  $\text{CcO}_{II}$  causes an increase in transverse relaxation rate, especially at temperatures above 10 K.

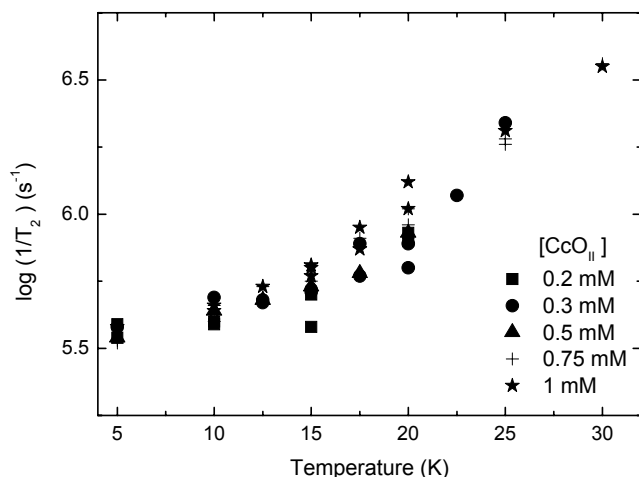


Figure 4.4. Transverse relaxation times of  $\text{Cu}_A$  as a function of temperature and for several  $\text{CcO}_{II}$  concentrations.

Recent X-band measurements showed that the transverse relaxation of  $\text{Cu}_A$  depends on the spectral position [Lyubenova]. This behavior was also found at G-band frequency, as shown in figure 4.5. The difference in relaxation times between  $g_{yy}$  and the low-field edge near  $g_{zz}$  at G-band (factor of 1.4) is smaller than between  $g_{\perp}$  and  $g_{\parallel}$  at X-band (factor of 2). Also, at G-band the difference in relaxation times decreases with increasing temperature, becoming negligibly small at 15 K. This is probably because a different, isotropic,  $T_2$  process becomes dominant at higher temperatures (see discussion section).

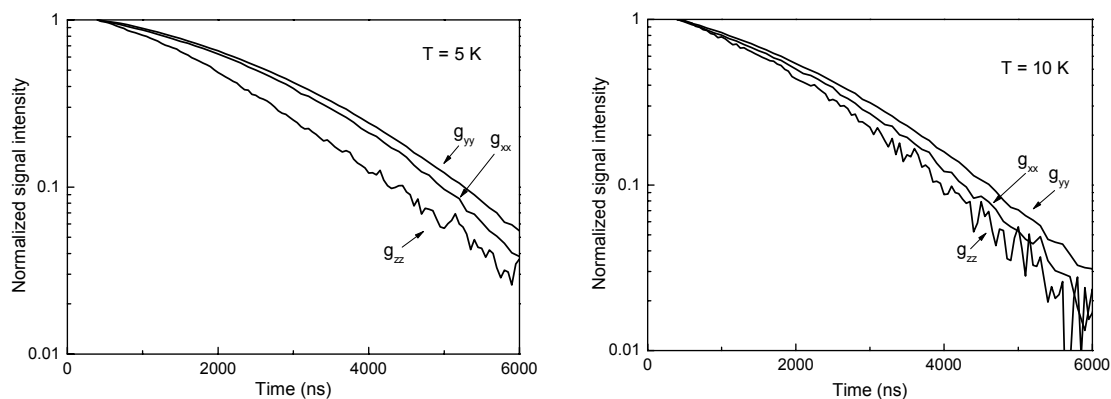


Figure 4.5. Echo decay traces of  $\text{Cu}_A$  in 1 mM  $\text{CcO}_{II}$  at 5 K and at 10 K for different spectral positions as indicated in the plots.

The temperature dependence of the  $T_1$  relaxation of  $\text{Cu}_A$  at G-band was also very different from that at X-band frequency. This subject will be treated in detail in chapter 6.

#### 4.1.2. Cytochrome c Oxidase

Samples containing approximately 1 mM four-subunit CcO were studied at X-band and G-band frequencies. All structural parameters of the two paramagnetic centers are known ([Iwata et al. 1995], and see chapter 2 for the g-tensor of heme a). The field-swept G-band EPR spectra of  $\text{Cu}_A$  in full CcO are indistinguishable from those of  $\text{Cu}_A$  in  $\text{CcO}_{II}$ . Hahn-echo decay traces of  $\text{Cu}_A$  in CcO measured between 5 and 25 K at G-band are shown in figure 4.6. A significant enhancement of relaxation of  $\text{Cu}_A$  in CcO with respect to  $\text{Cu}_A$  in  $\text{CcO}_{II}$  was observed, both at X-band and G-band frequencies.

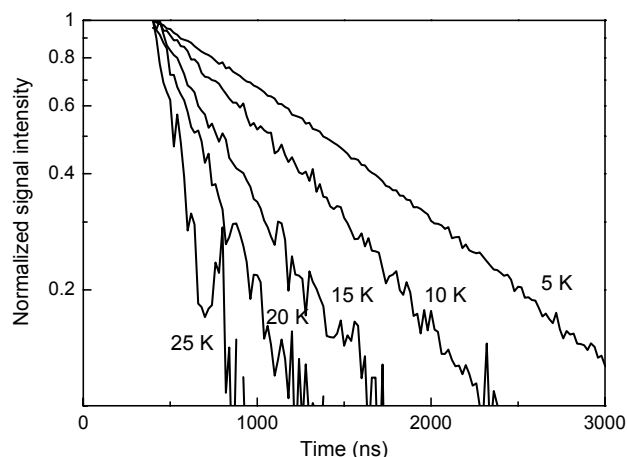


Figure 4.6. Echo decay traces of  $\text{Cu}_A$  in four-subunit CcO. Experimental parameters as given in chapter 3. All measurements were performed at the maximum of the  $\text{Cu}_A$  signal, i.e.  $g_{yy}$ .

In order to study purely dipolar relaxation enhancement, the echo decay traces of  $\text{Cu}_A$  in CcO were divided by echo decay traces of  $\text{Cu}_A$  in a sample of 0.3 mM  $\text{CcO}_{II}$ , as explained in chapter 3. Some of the resulting traces are plotted in figure 4.7. All dipolar relaxation traces were well described by a single exponential, from which we inferred that all measurements had been performed in the low-temperature region as defined in chapter 2. The values of  $T_2^{\text{dip}}$  are therefore equal to  $T_{1f}$ .  $T_{1f}$  values are plotted as a function of temperature in figure 4.8 together with  $T_1$  of heme a at X-band from [Scholes et al. 1984]. There is a large difference between the  $T_1$  values obtained at G-band, and those from X-band measurements. The origin of this difference will be discussed in chapter 6. The echo decay traces measured at  $g_{xx}$  of  $\text{Cu}_A$  were identical to those at  $g_{yy}$ , because in the low-temperature regime the dipolar relaxation does not depend on the dipolar coupling  $\Delta$ , and therefore the dipolar relaxation in this regime is isotropic.

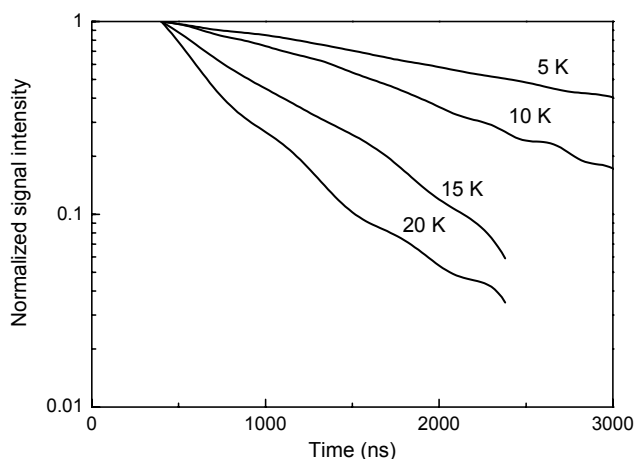


Figure 4.7. Dipolar relaxation traces of  $\text{Cu}_A$  in CcO. The echo decay traces of  $\text{Cu}_A$  in CcO and  $\text{Cu}_A$  in  $\text{CcO}_{II}$  were low-pass filtered prior to division. All traces were fitted with single exponential functions.

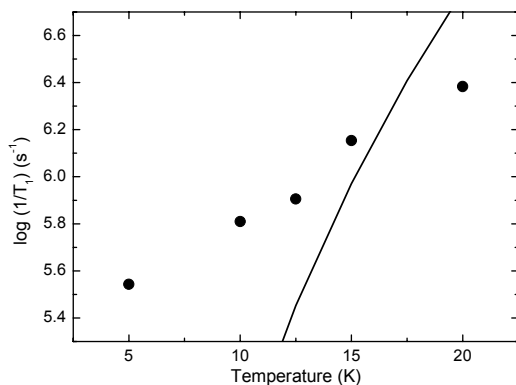


Figure 4.8.  $T_1$  relaxation time of heme a at X-band (solid line, from [Scholes et al. 1984]) and G-band frequency (filled circles, from fits to dipolar relaxation traces of CcO).

An attempt to exclude the influence of heme  $a_3$  on the relaxation behavior of  $Cu_A$  in CcO failed. We tried to perform measurements on the mixed-valence CcO, in which heme  $a_3$  is diamagnetic, but heme a and  $Cu_A$  are both paramagnetic [Vanneste 1966]. To obtain this state, samples containing approximately 1 mM CcO were bubbled with CO for several minutes and then left to react for at least 30 minutes. This causes 50-60% of heme  $a_3$  to be reduced, and 5-10% of heme a [Bickar et al. 1984]. The samples were transferred under  $N_2$  atmosphere to capillaries for G-band measurements.

The transverse relaxation of  $Cu_A$  in CcO after treatment with CO was slightly faster ( $T_2$  was 200-500 ns shorter) than that before treatment between 5 K and 12.5 K. At 15 K, the highest temperature studied, the echo decay traces were the same within error. However, we did not analyze the experiments because of the uncertainty of the redox states of heme a and heme  $a_3$ .

#### 4.1.3. Different Cytochromes

To study the binding of cytochrome c to  $CcO_{II}$ , the transverse relaxation of  $Cu_A$  was studied for  $CcO_{II}$  alone, and for  $CcO_{II}$  in the presence of equimolar amounts of one of three cytochromes  $c_{552}$ ,  $c_{hh}$  or  $c_1$ . The spectral parameters of the cytochrome c hemes are given in chapter 2. The results for the four different samples at 10 K are shown in figure 4.9. Addition of cytochrome to  $CcO_{II}$  caused enhancement of the transverse relaxation of  $Cu_A$ , but the extent of enhancement was smaller for  $c_1$  than for  $c_{552}$  and  $c_{hh}$ . For a quantitative analysis, the relaxation traces of the  $CcO_{II}$ -cytochrome mixtures were divided by the traces of  $CcO_{II}$ , to get rid of internal  $Cu_A$  relaxation and potential other

intrinsic effects, as was discussed in chapter 3.

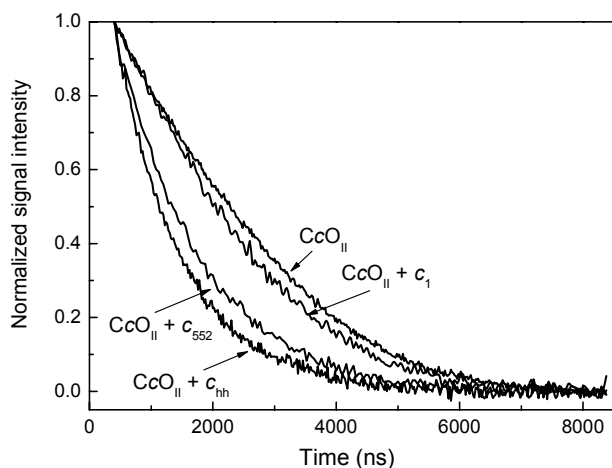


Figure 4.9. Echo decay traces of 0.2 mM  $CcO_{II}$  in absence or presence of either 0.2 mM  $c_1$ , 0.2 mM  $c_{552}$  or 0.2 mM  $c_{hh}$ , as indicated in the plot. Temperature: 10 K, the echo decay traces were recorded at the maximum of the  $Cu_A$  signal (corresponding to  $g_{yy}$ ).

To avoid an increase in noise in the spectra, both datasets were low-pass filtered prior to division. Subsequently, a direct comparison of the dipolar-coupling induced relaxation was made.

The dipolar relaxation caused by the addition of  $c_1$  is small relative to the dipolar relaxation in the  $CcO_{II}$ - $c_{552}$  and  $CcO_{II}$ - $c_{hh}$  mixtures. The non-binding  $c_1$ , which we employ as a negative control, on first thought should not cause any relaxation enhancement in  $Cu_A$ , as it does not form a productive complex with  $CcO_{II}$  [Janzon]. However, due to the large magnetic moment of electrons, dipole-dipole interaction is sensed even at the large distances that are found in a random distribution of cytochrome molecules in a sample. Figure 4.10 shows experimental data as well as simulations of the dipolar relaxation of randomly distributed cytochromes  $c_1$  and  $CcO_{II}$ , at protein concentrations of 0.2 mM and of 0.75 mM. The dipolar relaxation in the simulations is slower than the corresponding experimental data.

The cytochromes  $c_{552}$  and  $c_{hh}$  cause relaxation enhancement that is significantly larger than that caused by  $c_1$ . This is a strong indication of complex formation by the first two cytochromes.

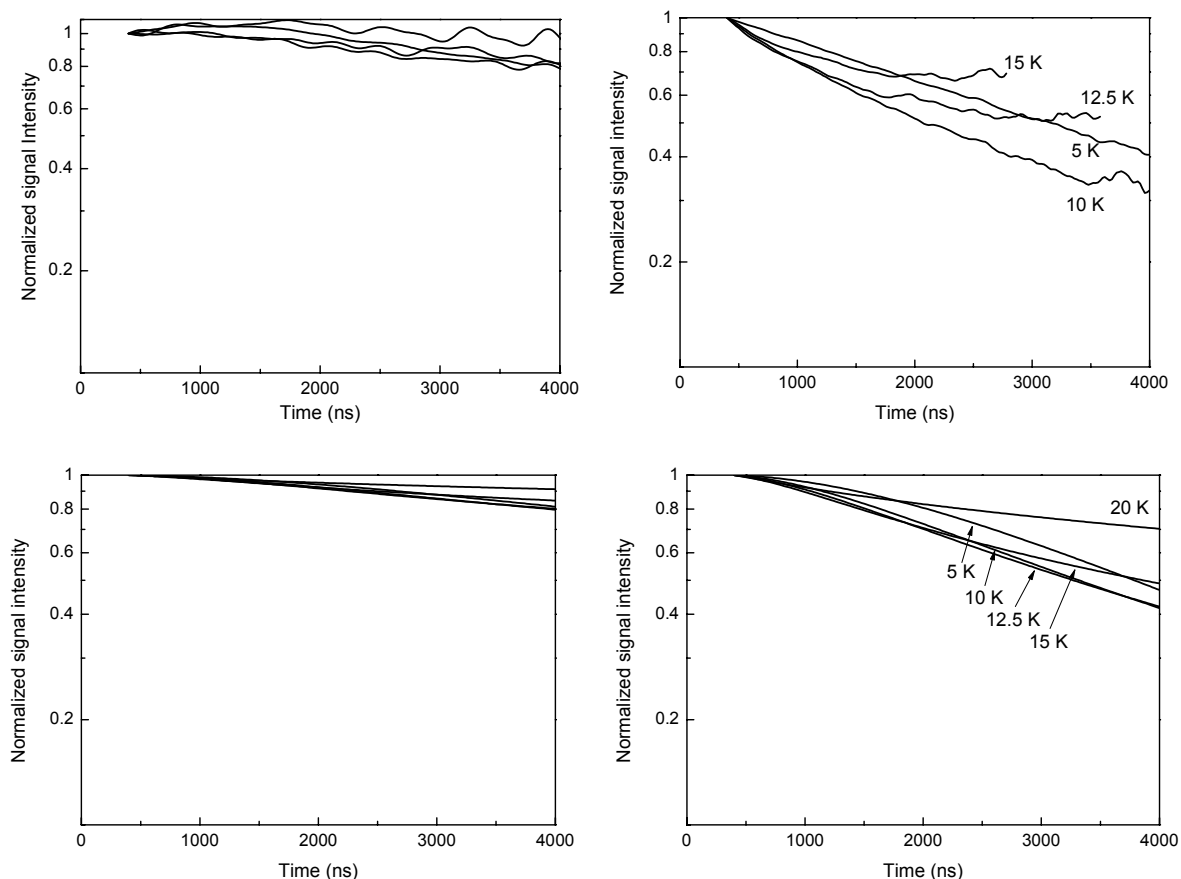


Figure 4.10. Dipolar relaxation of a mixture of 0.2 mM  $CcO_{II}$  and 0.2 mM  $c_1$  (left) and of 0.75 mM  $CcO_{II}$  and 0.75 mM  $c_1$  (right). Top: data measured at G-band; bottom: data simulated using our program to calculate dipolar relaxation caused by a random distribution of spins. The samples with a concentration of 0.2 mM protein were measured or simulated at the same temperatures as the higher concentrated samples.

For the mixture of  $\text{CcO}_{\text{II}}$  and  $c_1$  the relaxation scales with concentration as predicted by [Salikhov et al. 1981] and by our simulations. In contrast, the dipolar relaxation observed in the mixtures of  $\text{CcO}_{\text{II}}$  with either  $c_{552}$  or  $c_{\text{hh}}$  is relatively larger at low concentration than at high concentration, pointing to complex formation.

Dipolar relaxation was studied at different temperatures. The temperature dependences of the mixtures with each of the three cytochromes are shown in figures 4.10 to 4.12. Comparing the three G-band measurements it is obvious that there is again a significant difference in behavior between the mixture with  $c_1$  on the one hand, and the mixtures with  $c_{\text{hh}}$  and  $c_{552}$  on the other. The temperature dependence of the sample with  $\text{CcO}_{\text{II}}$  and  $c_1$  is weaker than that for the two binding cytochromes, especially at the lower protein concentration shown (0.2 mM). This is evidence for a (nearly) random distribution of cytochrome in the sample, because a single fixed distance between paramagnetic centers leads to a strong, well-characterized temperature dependence (see chapter 2).

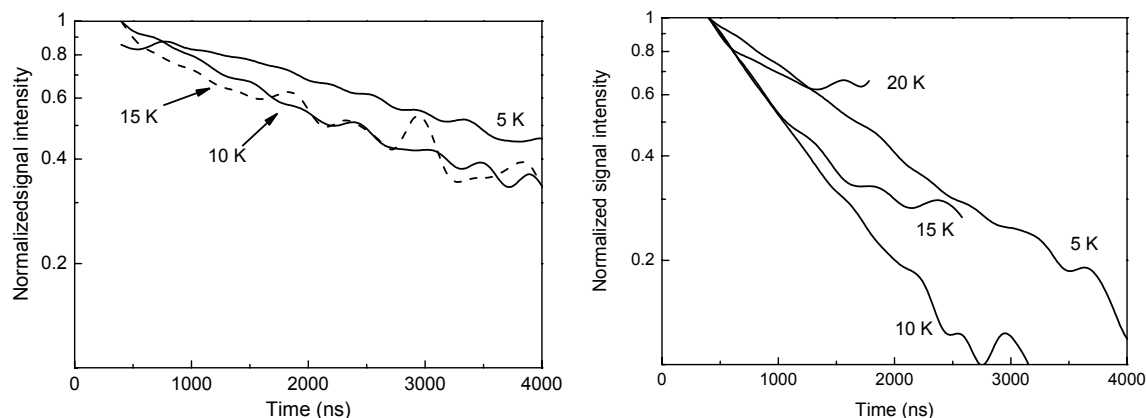


Figure 4.11. Dipolar relaxation of a mixture of 0.2 mM  $\text{CcO}_{\text{II}}$  and 0.2 mM  $c_{552}$  (left) and of 0.75 mM  $\text{CcO}_{\text{II}}$  and 0.75 mM  $c_{552}$  (right). The 15 K trace in the right figure is dashed for clarity.

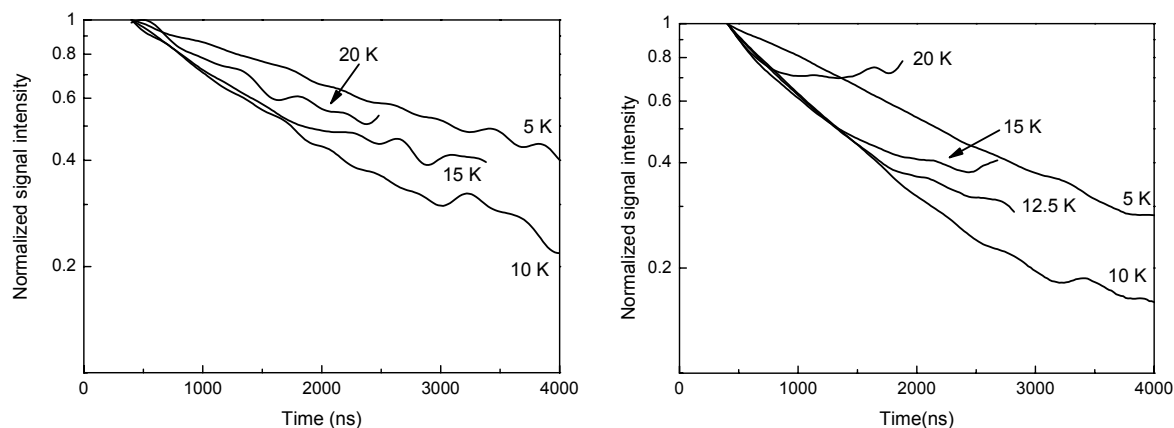


Figure 4.12. Dipolar relaxation traces of a mixture of 0.2 mM  $\text{CcO}_{\text{II}}$  and 0.2 mM  $c_{\text{hh}}$  (left) and of 0.75 mM  $\text{CcO}_{\text{II}}$  and 0.75 mM  $c_{\text{hh}}$  (right).

The maximum relaxation enhancement effect occurs at a lower temperature at G-band than at X-band frequency. The maximum occurs at  $1/T_{1f} = \Delta$ , as discussed in section 2.3.3. Dipolar coupling is independent of magnetic field, therefore a difference in the  $T_1$  of cytochrome heme must be the reason for this shift. No relaxation times of heme iron are known at frequencies higher than X-band, and due to the extreme broadness of

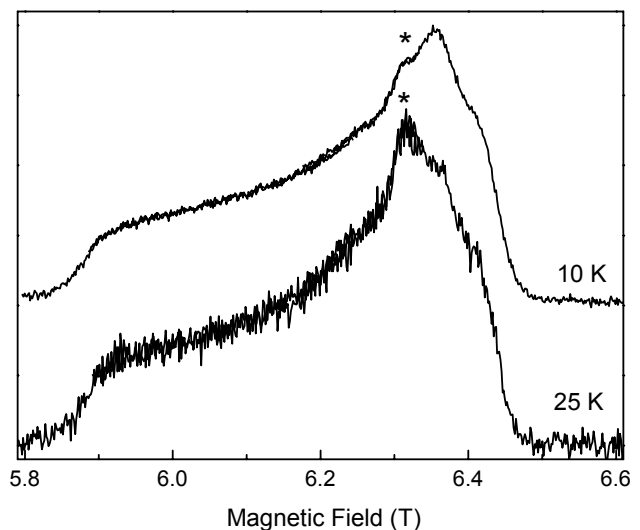
the heme iron signal, its relaxation time could not be measured at G-band. However, an estimate of  $T_1$  was made by studying the dipolar relaxation of  $Cu_A$ , because at low temperatures  $T_2^{\text{dip}} = T_{1f}$ . This way,  $T_1$  relaxation of the heme iron at G-band was found to have a different temperature dependence than at X-band, and to be significantly faster at low temperature (1.6 ms at X-band *versus* 6  $\mu$ s at G-band). The frequency (or magnetic field) dependence of  $T_1$  relaxation will be discussed in more detail in chapter 6.

The mixture of  $CcO_{II}$  and  $c_{552}$  showed a pronounced temperature dependence for high sample concentration (0.75 mM), but this dependence was much less obvious for the less concentrated sample (0.2 mM). The dipolar relaxation of the mixture of  $CcO_{II}$  and  $c_{hh}$  had a clear temperature dependence both at low and at high sample concentrations. Comparing figures 4.11 and 4.12, it can be seen that the dipolar relaxation enhancement due to  $c_{552}$  is stronger at the higher sample concentration. The traces at 5 and at 15K at the lower concentration are almost equal to those measured in the mixture of  $CcO_{II}$  and  $c_{hh}$ .

At X-band frequency, the dipolar relaxation enhancement induced by  $c_{hh}$  was larger than that induced by  $c_{552}$  [Lyubenova et al.]. The occurrence of anisotropic dipolar relaxation at G-band was therefore investigated only for the mixture of  $c_{hh}$  and  $CcO_{II}$ . Anisotropic relaxation was studied in two ways: 1) by comparing field-swept spectra at different temperatures and/or different  $\tau$  values, and 2) by comparing echo decay traces measured at different spectral positions. The measurements were only performed with samples containing 0.2 mM  $CcO_{II}$  and 0.2 mM  $c_{hh}$ , because non-specific dipolar interactions with surrounding spins would obscure the specific, possibly anisotropic dipolar relaxation effect coming from the protein-protein complex.

In a field-swept spectrum, relaxation anisotropy causes differences between spectra measured with small  $\tau$  values (or low temperature) and spectra recorded with large  $\tau$  (higher temperature), see chapter 2. Some typical field-swept spectra measured at two different temperatures are shown in figure 4.13. The spectra were measured using the extended sweep-coil sweep method described in chapter 3 at temperatures between 10 and 25 K. Despite the presence of a slower relaxing  $Cu^{2+}$  contamination, that shows up as a low-field shoulder on the  $Cu_A$  spectrum, strong relaxation anisotropy caused by dipolar coupling could be excluded.

*Figure 4.13. Field-swept spectra of a mixture of 0.2 mM  $CcO_{II}$  and 0.2 mM  $c_{hh}$ , measured by the extended sweep coil sweep method. Each spectrum is composed of three spectra overlaid end-to-end. Main magnetic field set to 6.400 T, 6.100 T and 6.000 T for each of the three sweeps, respectively. The sweep coil was swept from its minimum to its maximum value (see chapter 3 for details of the measurement). The peak marked by an asterisk is due to  $Cu^{2+}$  contamination. It relaxes more slowly than  $Cu_A$  and thus has a higher relative intensity in the spectrum taken at 25 K.*



The dipolar relaxation traces of  $\text{Cu}_A$  in the presence of  $c_{hh}$  were measured at two turning points in the spectrum ( $g_{xx}$  and  $g_{yy}$ ), as shown in figure 4.14. At these positions, the dipolar echo decay traces are expected to differ, as at the  $g_{xx}$  position only a very small selection of spins is detected, and therefore only a small spread of dipolar coupling values. At  $g_{xx}$  the dipolar relaxation should be nearly mono-exponential at all temperatures, whereas at  $g_{yy}$  more spins contribute to the signal and the dipolar relaxation traces are multi-exponential at temperatures higher than 10 K. No differences in dipolar relaxation were found at these points or at a point in between  $g_{xx}$  and  $g_{yy}$ . The signal was too small at the  $g_{zz}$  position to obtain reliable data at temperatures higher than 10 K.

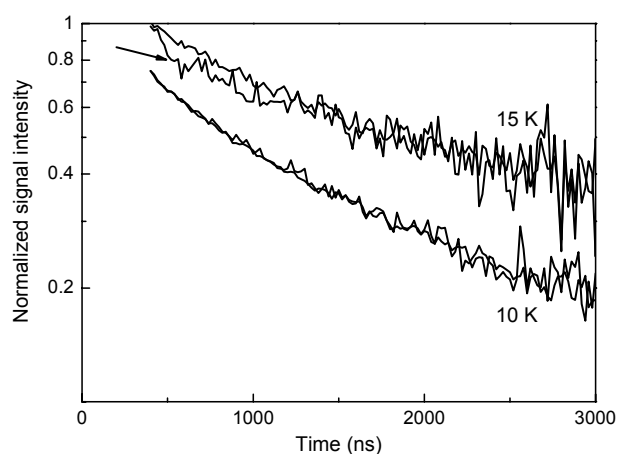


Figure 4.14. A. Dipolar relaxation traces of  $\text{CcO}_{II}$  with  $\text{cyt } c_{hh}$  measured at  $g_{xx}$  and  $g_{yy}$  spectral positions at two temperatures as indicated in the plot. The echo decay traces measured at 10 K were shifted by a factor of 0.75 for clarity.

The bump in the echo decay trace measured at  $g_{xx}$  at 15 K is an artifact caused by a slight error in the echo decay trace of  $\text{CcO}_{II}$ , that was amplified by the division procedure.

#### 4.1.4. Simulations

A program developed in our group was used to simulate the dipolar relaxation traces and their dependence on temperature, magnetic field and spectral position (see chapter 3 and appendix A). The program aided the interpretation of dipolar relaxation experiments; this is not straightforward due to the presence of all orientations of the proteins (powder sample). Measurements on a single crystal would be considerably easier to interpret.

Using the simulation program, the X-band data taken at five different temperatures (12, 16, 18, 20 and 23 K) were fitted with eight parameters, as well with small corrections (within a factor of two) to the cytochrome heme  $T_1$  values from [Scholes et al. 1984]. The fit parameters were: the distance  $r$ , two dipolar angles  $\theta_D$  and  $\phi_D$ , three Euler angles  $\alpha$ ,  $\beta$  and  $\gamma$ , the exchange coupling  $J$  and an offset. The X-band data could be equally well described by several different parameter sets. One of the fits is shown in figure 4.15, together with a G-band simulation using the same structural parameters; these parameters are given in the figure caption. This simulation was performed assuming a temperature dependence of heme  $T_1$  at G-band that is discussed in chapter 6.



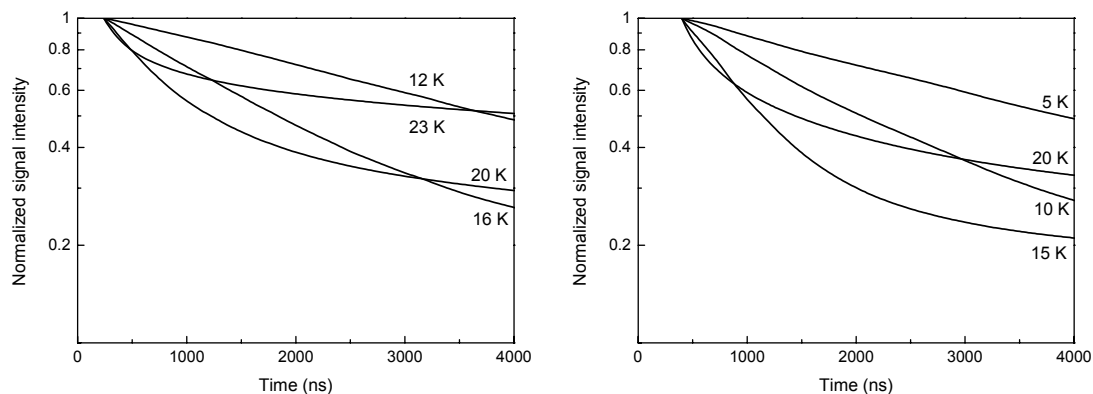


Figure 4.15. Simulations for X-band (left) and G-band (right) assuming one complex structure. Fit parameters:  $R = 2.6$  nm; dipolar angles  $\theta_D = 48^\circ$ ,  $\varphi_D = 37^\circ$ ; Euler angles  $\alpha = 0^\circ$ ,  $\beta = 5^\circ$ ,  $\gamma = 43^\circ$ ;  $J = 1.7$  MHz; offset 11%. Because of the difference in temperature dependence of  $T_{1f}$  at X- and G-band, the simulations were performed for different temperature intervals.

The large offset observed in the X-band experimental data taken at high temperature (23 K) was fitted by the computer program by setting  $J$  to such a value that the dipolar pattern was shifted and the most intense ( $\theta_D = 90^\circ$ ) peak had  $\Delta = 0$ . Only in very special cases would  $\Delta$  ( $90^\circ$ ) and  $J$  to cancel each other out exactly like that, therefore these results were regarded as artifacts of the fit program. This belief was supported by the fact that the G-band echo decay traces could not be simulated with these parameters.

Nevertheless, for all of the parameter sets obtained from fits to the X-band data, 2D simulations (time  $\tau$  vs. magnetic field  $B_0$ ) were performed to investigate dipolar relaxation anisotropy. No anisotropy was seen in the simulations of X-band spectra, because the spectral resolution at this frequency is not high enough (figure 4.16, left). In contrast, all of the G-band simulations performed with the parameters obtained from X-band fits, such as that depicted in the right plot in figure 4.16, showed significant relaxation anisotropy: the field-swept spectrum at low temperature differed markedly from the spectrum at high temperature, when a dead time of 200 ns was included for both spectra. No relaxation anisotropy was detected experimentally, however. Consequently, we discarded all parameter sets obtained from these X-band fits as possible structures of the bound cytochrome *c*-CcO complex.

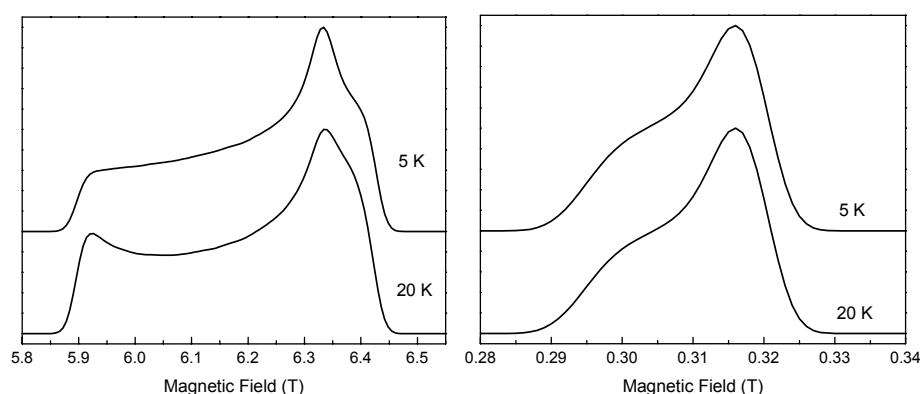


Figure 4.16. Simulations of field-swept spectra at G-band (left) and at X-band (right) frequency, assuming one complex structure.  $T = 200$  ns; simulation parameters as in figure 4.15.

The lack of dipolar relaxation anisotropy can be explained by assuming that not a single, well-defined protein-protein complex structure was detected, but rather a

superposition of many different complexes. This hypothesis lead us to attempt fitting the X-band data with an adapted version of the fit program, in which two complex geometries were allowed. The relative amount of the two complex structures, as well as the distances and orientations with respect to  $\text{Cu}_A$  for each of the two complex geometries were allowed to vary. The X-band data could be fitted very well with various parameter sets, in which one  $\text{Fe}^{3+} - \text{Cu}_A$  distance was short (2 nm), and the other significantly longer (4 nm). A representative fit of the X-band data and a simulation with the same parameters at G-band are shown in figure 4.17. A comparison of figure 4.15 and 4.17 shows that the X-band fits with either one or two complex structures are indistinguishable. At G-band there is a clear difference between the two simulations, due to the higher spectral resolution. In contrast to X-band, however, the G-band experimental results are not in agreement with the simulations.

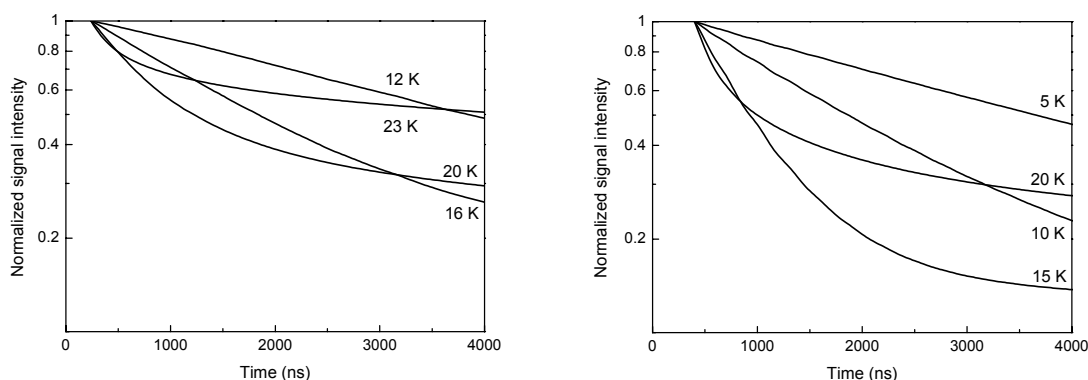


Figure 4.17. Simulations (X-band and G-band) with two structures. Fit parameters:  $R = 2.3 \text{ nm}$ ; dipolar angles  $\theta_D = 54^\circ$ ,  $\varphi_D = 11^\circ$ ; Euler angles  $\alpha = 27^\circ$ ,  $\beta = 6^\circ$ ,  $\gamma = 29^\circ$  (set 1) and  $R = 4.0 \text{ nm}$ ; dipolar angles  $\theta_D = 54^\circ$ ,  $\varphi_D = 11^\circ$ ; Euler angles  $\alpha = 90^\circ$ ,  $\beta = 57^\circ$ ,  $\gamma = 12^\circ$  (set 2); offset 11%; the data from set 1 and set 2 were added in a ratio of 1.2:1. The simulations at X-band and G-band were performed for different temperature intervals as explained in the figure caption of figure 4.15.

The G-band 2D simulations obtained using the parameters from the X-band fits with two complex structures showed less relaxation anisotropy than those with one complex structure (compare figures 4.16 and 4.18). These simulations are in better agreement with the data from high-field measurements.

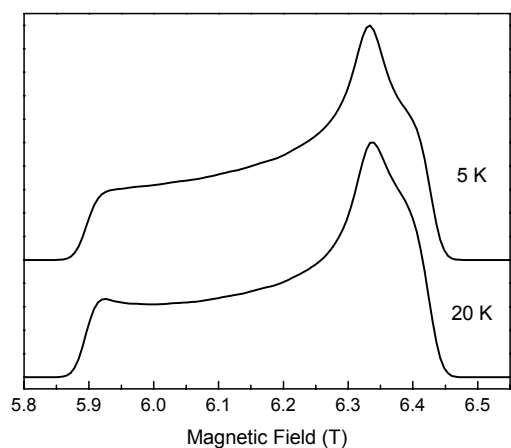


Figure 4.18. Simulations of field-swept spectrum at  $\tau = 200 \text{ ns}$ , taking into account two complex structures. Simulation parameters as given in figure 4.14.

Due to the large increase in the number of parameters, we were not able to perform reliable fits with more than two complex structures. We did perform fits with structures proposed by docking studies [Flöck et al. 2002; Bertini et al. 2005], but were not able to obtain good fits to the X-band data with these parameters, even with a superposition of several structures.

## 4.2. Discussion

### 4.2.1. Cu<sub>A</sub> Relaxation

The binuclear copper center Cu<sub>A</sub> from *Paracoccus denitrificans* cytochrome *c* oxidase was studied by EPR at G-band frequency (180 GHz) for the first time. At this frequency, the small anisotropy between  $g_{xx}$  and  $g_{yy}$  could be resolved and consequently, orientation-dependent studies could be performed.

The transverse relaxation properties of Cu<sub>A</sub> differ at X-band and G-band frequencies. At low temperature ( $T \leq 10$  K) the echo decay traces are very similar. The fact that the traces were well described by stretched exponentials means that the main contribution to  $T_2$  relaxation of Cu<sub>A</sub> at low temperature is a non-Markoffian process [Klauder et al. 1962]. At higher temperatures  $T_1$  relaxation dominates the Cu<sub>A</sub>  $T_2$  relaxation at G-band, making the echo decay faster than at X-band and causing mono-exponential signal decay. Not many studies on Cu<sub>A</sub> intrinsic relaxation have been performed. Brudvig and coworkers found that the relaxation of Cu<sub>A</sub> was relatively fast in comparison to other copper centers in proteins with comparable  $g$ -anisotropy [Brudvig et al. 1984], and attributed this fact to dipolar coupling to nearby heme *a*. The echo decay of Cu<sub>A</sub> in the absence of heme *a* was not studied.

The anisotropic relaxation of Cu<sub>A</sub> that was seen at X-band [Goodman et al. 1984; Lyubenova] was also observed at G-band frequency. However, the difference in relaxation rate between  $g_{yy}$  and  $g_{zz}$  was smaller at G-band than that between  $g_{\perp}$  and  $g_{\parallel}$  at X-band. Additionally, at G-band the anisotropy in relaxation disappears for higher temperatures ( $T \geq 15$  K). This may be explained by the fact that at G-band the  $T_2$  relaxation is dominated by  $T_1$  relaxation at these temperatures. Although it was found that  $T_1$  relaxation of Cu<sub>A</sub> is anisotropic [Mchaourab et al. 1993], this is not expected to be the case for Cu<sub>A</sub> at G-band below 20 K. Up to approximately 20 K the direct process dominates  $T_1$  relaxation at G-band frequency and this process is isotropic. More details about  $T_1$  relaxation of Cu<sub>A</sub> can be found in chapter 6 of this thesis.

Transverse relaxation depends on the concentration of paramagnetic centers in the sample, because it is caused in part by spin-spin interactions (see chapter 2). It was found here that the echo decay was faster for higher CcO<sub>II</sub> concentrations (figure 4.4), but the effect did not depend linearly on the concentration, in contrast to what was postulated by [Salikhov et al. 1981]. This is due to the fact that many different processes contribute to Cu<sub>A</sub> relaxation, and most processes do not depend on spin concentration.

### 4.2.2. Dipolar Relaxation of Cu<sub>A</sub> by heme *a*

The dipolar interaction between heme *a* and Cu<sub>A</sub> in CcO was studied at G-band for the first time in order to test the method and our simulation program. All structural parameters, as well as the  $T_1$  of heme *a* at X-band, are known [Scholes et al. 1984; Iwata et al. 1995]. The distance between the fast-relaxing heme *a* and Cu<sub>A</sub> in CcO is 2.1 nm, which causes a dipolar coupling on the order of 6 MHz.

A strong relaxation enhancement was found for Cu<sub>A</sub> in four-subunit CcO with respect to Cu<sub>A</sub> in CcO<sub>II</sub>, both at X-band and G-band frequency. To study the pure dipolar relaxation, relaxation traces of Cu<sub>A</sub> in CcO were divided by decay traces of Cu<sub>A</sub> in CcO<sub>II</sub>. However, performing this division procedure on the echo decay traces measured at X-

band indicated that there is a structural difference between the  $\text{Cu}_A$  center in CcO and the one in  $\text{CcO}_{\text{II}}$ : the echo modulation, which is caused by hyperfine interaction and which appears on the echo decay traces of  $\text{Cu}_A$  at X-band, was different for  $\text{Cu}_A$  in CcO than for  $\text{Cu}_A$  in  $\text{CcO}_{\text{II}}$  [Lyubenova 2006]. In an earlier EPR study, no difference was found between the field-swept spectra of the  $\text{Cu}_A$  centers in CcO and in  $\text{CcO}_{\text{II}}$  [Lappalainen et al. 1993]. But the small hyperfine couplings that cause the echo modulation on an echo decay trace cannot be resolved in field-swept spectra due to line broadening effects. In the same study it was found that  $\text{Cu}_A$  in  $\text{CcO}_{\text{II}}$  was more sensitive to changes in pH and was somewhat labile in comparison to  $\text{Cu}_A$  in full CcO. On the basis of EPR measurements at high pH, it was suggested that there was a change in ligation of the  $\text{Cu}_A$  center in  $\text{CcO}_{\text{II}}$  with respect to  $\text{Cu}_A$  in CcO. There may also be differences in the relaxation behavior of  $\text{Cu}_A$  in CcO and in  $\text{CcO}_{\text{II}}$ , but these could not be measured as we did not have a sample where heme a was reduced (diamagnetic) and  $\text{Cu}_A$  oxidized (paramagnetic).

The dipolar relaxation traces at G-band were mono-exponential up to 30 K, which was the highest temperature where an echo signal could be observed, and the dipolar relaxation for  $g_{xx}$  and  $g_{yy}$  was the same over the whole measured temperature range. The measurements must therefore have been performed in the low-temperature regime, as defined in chapter 2. This was in disagreement with the assumed  $T_1$  relaxation behavior of heme a at G-band (see chapter 6). No structural information could be obtained from our results, because in the low-temperature regime dipolar relaxation depends solely on the  $T_1$  of the fast-relaxing spin.

The results from CO-treated CcO were not analyzed because the dipolar relaxation became faster after treatment with CO, instead of slower, which one would expect when the fast-relaxing heme  $a_3$  is reduced. This may be due to the partial reduction of heme a, which causes less  $\text{Cu}_A$  centers to be affected by dipolar relaxation. Further analysis of the data was not considered useful, because it was not possible to determine the fraction of oxidized heme a.

Several attempts have been made in the past to determine the distance between  $\text{Cu}_A$  and heme a by EPR measurements [Brudvig et al. 1984; Goodman et al. 1984], but none succeeded in obtaining a correct, accurate result. One reason may well be that CcO in its oxidized form contains not just the paramagnetic centers  $\text{Cu}_A$  and heme a, but a high-spin heme  $a_3$  and mono-nuclear  $\text{Cu}_B$  as well. The EPR parameters of these metal centers are not well known; it is generally assumed that heme  $a_3$  and  $\text{Cu}_B$  are very strongly coupled and form a  $S = 2$  center that relaxes so fast that it cannot be detected by EPR. Heme  $a_3$  and/or  $\text{Cu}_B$  might induce dipolar relaxation in  $\text{Cu}_A$  or in heme a. This would make quantitative analysis of the dipolar relaxation data of CcO impossible, because too little is known about heme  $a_3$  and  $\text{Cu}_B$  to be able to include them in our simulations. The effect of heme  $a_3$  and  $\text{Cu}_B$  on the relaxation behavior of  $\text{Cu}_A$  was previously found to be negligible [Brudvig et al. 1984; Goodman et al. 1984], but the evidence is questionable.

We concluded that CcO in this form was not a good system to test our simulation program. Measurements on the mixed-valence CcO, where heme  $a_3$  is reduced and diamagnetic, and heme a and  $\text{Cu}_A$  oxidized and paramagnetic, should make the analysis more straightforward. It would, however, still be necessary to know the echo decay behavior of  $\text{Cu}_A$  in CcO in absence of heme a. Goodman and Leigh have succeeded in

measuring  $\text{Cu}_A$  in CcO with heme a, heme  $a_3$ , and  $\text{Cu}_B$  reduced [Goodman et al. 1984]. They did not arrive at the correct  $\text{Cu}_A$ -heme a distance, due to the difficulties that arise with the interpretation of CW saturation experiments: one can only measure the product of  $T_1$  and  $T_2$ . The  $T_1$  values of heme a that were calculated by Goodman and Leigh were not in agreement with those measured by pulse EPR, and consequently the data analysis was flawed. Similar measurements as those performed by Goodman and Leigh should be redone using pulse EPR, which simplifies the analysis of the relaxation data.

Our measurements on CcO have shown that a crucial step in the quantitative analysis of dipolar relaxation enhancement measurements is the possibility of studying the paramagnetic center of interest in presence and in absence of its dipolar-coupled partner.

#### 4.2.3. Dipolar Relaxation of $\text{Cu}_A$ by Cytochrome $c_1$

The transverse relaxation of  $\text{Cu}_A$  was enhanced by the presence of  $c_1$ . Simulations of  $\text{Cu}_A$  surrounded by randomly distributed cytochromes show similar relaxation enhancement. For these simulations, the same  $T_1$  relaxation was assumed for  $c_1$  as for bovine cytochrome c [Scholes et al. 1984]. This assumption is reasonable, because the direct environment of the heme in cytochromes c is very similar. Also, the  $T_1$  relaxation of  $c_{552}$  was measured by X-band EPR at temperatures between 5 and 15 K and found to be in excellent agreement with the values found by Scholes and coworkers for  $c_{\text{hh}}$  [Weber].

By performing simulations, it was shown that randomly distributed cytochromes cause a temperature-dependent dipolar relaxation enhancement of  $\text{Cu}_A$  transverse relaxation. This was also found experimentally for  $c_1$ , a cytochrome that is a very poor electron donor to CcO [Janzon], and does not form a specific complex with CcO. The simulated dipolar relaxation traces decayed slower than the experimental data, which may mean two things: 1) the concentration of cytochrome in the samples was not 0.2 mM and 0.75 mM, but 0.3 mM and 1.1 mM respectively; 2) the probability of cytochromes being close to  $\text{CcO}_{\text{II}}$  is (slightly) higher than expected in a purely statistical distribution. The second effect could be explained by assuming weak binding of cytochromes to  $\text{CcO}_{\text{II}}$  (for example at other positions than at the cytochrome c binding site).

Comparison with X-band data and simulations led us to the conclusion that the dipolar relaxation caused by  $c_1$  is due to the random distribution of cytochrome in the sample, with a slightly enhanced probability of the cytochrome being in the near vicinity of  $\text{Cu}_A$  [Lyubenova et al.]. This hypothesis should be checked by measuring a sample of  $\text{CcO}_{\text{II}}$  and  $c_1$  at very high salt concentrations, where electrostatic attraction between the two proteins would be much less. The dipolar relaxation traces should then reach –or at least approach– the simulated dipolar relaxation traces.

#### 4.2.4. Dipolar Relaxation of $\text{Cu}_A$ by Cytochrome $c_{552}$ and $c_{hh}$

The addition of  $c_{552}$  or  $c_{hh}$  to a sample containing  $\text{CcO}_{II}$  significantly enhanced the transverse relaxation of  $\text{Cu}_A$ . This is not caused by aggregation, because (1) the relaxation enhancement observed in the samples with  $c_{552}$  and  $c_{hh}$  was significantly stronger than that observed for samples with  $c_1$ , and (2) the dipolar relaxation enhancement caused by  $c_1$  scaled with protein concentration at both EPR frequencies, as predicted by [Salikhov et al. 1981] for randomly distributed spins in a sample. Finally, the fact that the dipolar relaxation enhancement showed a characteristic temperature dependence was a strong indication that a protein-protein complex was formed. This temperature dependence could be simulated qualitatively for the G-band data, and even quantitatively for the X-band measurements.

The data recorded at G-band frequency could not be quantitatively simulated for two reasons: the  $T_1$  relaxation behavior of the cytochrome heme at this frequency was unknown and could not be measured directly, as will be discussed in further detail in chapter 6. Also, the sample concentrations were not as accurately known as for the X-band samples. These concentrations did not need to be so exact, as the purpose of the high-field measurements was to study relaxation anisotropy, and not quantitative simulation of the echo decay traces.

The mixtures of  $\text{CcO}_{II}$  with  $c_{552}$  or with  $c_{hh}$  both showed a more pronounced temperature dependence at high sample concentration (0.75 mM), than at lower sample concentration (0.2 mM). This effect cannot be ascribed to the formation of more protein-protein complexes, because in both samples  $\text{CcO}_{II}$  and cytochrome are present in 1:1 ratios. The presence of a high concentration of (randomly distributed) paramagnetic centers caused temperature-dependent dipolar relaxation as shown in figure 4.10. An increase in the total concentration of paramagnetic centers thus lead to the more pronounced temperature dependence for high protein concentrations.

There was a significant difference in X-band between the dipolar relaxation enhancement of  $\text{Cu}_A$  by  $c_{552}$  and by  $c_{hh}$ . No extra information regarding the difference between the two cytochromes could be inferred from the G-band measurements because of the uncertainty (approximately 25%) in the protein concentrations of the G-band samples. In [Lyubenova et al.], it was argued that a difference in dipolar relaxation enhancement most probably points to differences in binding geometry or binding kinetics between the native  $\text{CcO}$  substrate  $c_{552}$  and alien  $c_{hh}$ . This hypothesis is supported by the fact that the two cytochromes have different binding interfaces, the interface of  $c_{hh}$  being more positively charged than that of  $c_{552}$ . Therefore, the binding kinetics are different, as seen in the dependence of substrate turnover on ionic strength. The maximum turnover rate of  $\text{CcO}$  with  $c_{hh}$  occurs at 56 mM, whereas the maximum for  $c_{552}$  is found at 15 mM [Drosou et al. 2002b]. The optimum ionic strength represents the condition where the association rate and the dissociation rate of the electron transfer (ET) partners are balanced: at lower ionic strength the dissociation process becomes rate-limiting, whereas at higher ionic strength the association process is hindered by electrostatic screening. The more highly charged cytochrome,  $c_{hh}$ , requires more charges to be effectively screened off from  $\text{CcO}$ , and therefore its turnover maximum occurs at higher ionic strength. For our measurements, the ionic strength of the samples was kept low (5 mM), to ensure complex formation. This ionic strength is much nearer to the optimum for  $c_{552}$

than to the optimum for  $c_{hh,r}$ , which may cause  $c_{hh}$  to bind in a different way than  $c_{552}$  (see below).

High-field EPR measurements could not detect anisotropy of the dipolar relaxation enhancement of  $Cu_A$  by  $c_{hh}$ , although all 2D simulations performed with parameter sets representing one complex geometry exhibited significant relaxation anisotropy. The structural parameters obtained from fits of X-band data assuming a single complex geometry were unusual (the distance  $r$  was too large for efficient ET to occur, the dipolar and Euler angles did not agree with the two binding interfaces of the proteins to face each other, and  $J$  exactly cancelled out the dipolar coupling at  $\theta_D = 90^\circ$ ). This led us to the hypothesis that the protein-protein complex exists in different geometries. Simulations taking into account two complex geometries were in very good agreement with the X-band echo decay traces, and also showed less relaxation anisotropy at high field. No fits were performed with more than two complex geometries because an increase of fit parameters causes more local minima: the time that is needed to obtain reliable results would increase drastically. We assume that including more complex geometries will provide equally good or even better fits to the X-band data (as adding more parameters cannot worsen the fit). The 2D simulations will show less or no relaxation anisotropy at G-band, because the superposition of different mutual orientations of the paramagnetic centers averages out the anisotropic effects.

These arguments back up theories about electron-transport complex formation that were inferred from experiments or calculations on cytochrome  $c$  with  $CcO$  [Roberts et al. 1999; Bertini et al. 2005], but also on various other electron-transfer protein pairs such as cytochrome  $c$  and cytochrome  $c$  peroxidase [Northrup et al. 1988; Nocek et al. 1996], cytochrome  $c$  and cytochrome  $b_5$  [Wendeloski et al. 1987], cytochrome  $f$  and plastocyanin [Ubbink et al. 1998], cytochrome  $c$  and flavodoxin [Cunha et al. 1999], cytochrome  $c_{550}$  or pseudoazurin and nitrous oxide reductase [Mattila et al. 2005], and many others (as reviewed in [Prudêncio et al. 2004]). These studies agree that ET complexes need to be: 1) unspecific, in order to bind to different partner proteins; 2) short-lived, because the formation and successive disruption of such complexes are the rate-limiting steps in the ET reaction [Crowley et al. 2004]. The binding model is therefore as follows (figure 4.19) [Wienk et al. 2003; Prudêncio et al. 2004]. The two electron-transfer partners are attracted to each other by their oppositely charged binding interfaces. The next step is the formation of a non-specific complex with a small amount of hydrogen bonds or salt bridges. The proteins rearrange slightly to form a functional electron-transfer complex, an electron is transferred from the donor to the acceptor protein, and the proteins dissociate. The effective electron-transfer complex might have a single geometry, in the lock-and-key fashion, but more likely is the formation of different complex geometries where an electron is transferred as soon as the distance between donor and acceptor is small enough. In this light, it should be borne in mind that structures of electron-transfer complexes that emerged from docking studies with experimental input [Muresanu et al. 2006], or without [Flöck et al. 2002] are falsely described as the only electron-transfer complex.

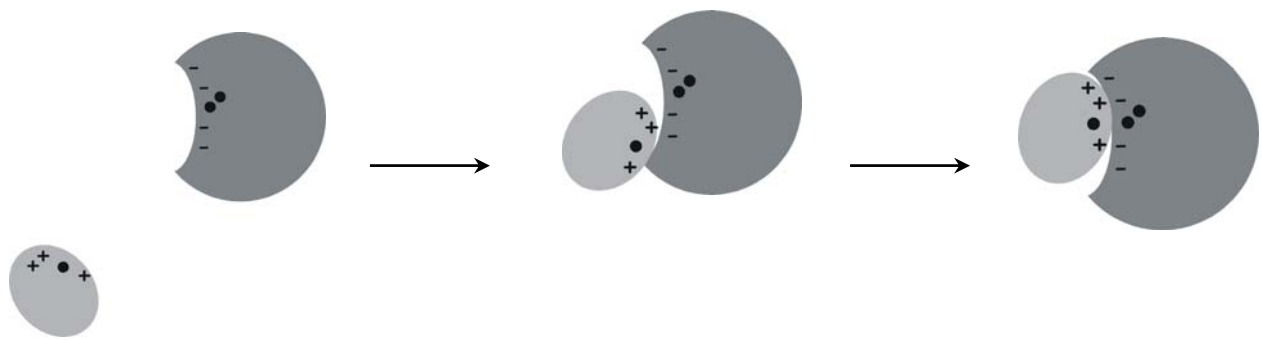


Figure 4.19. Scheme of the formation of an electron-transfer complex. The fictive proteins are depicted as ovals containing the electron donor and acceptor site as small black spheres. The charges on the proteins are denoted with + and - signs.

Long-range attraction due to the complementary charges on the ET partners guides the mobile protein to the binding site on its partner. Small rearrangements of the mobile protein allow the redox centers to come close enough for ET to occur. More details about the binding model are given in the text.

A possibility that cannot be discarded, however, is that different complex geometries were observed in our study because the low ionic strength condition of our EPR samples drove the proteins to build unspecific complexes. We performed both the X-band as well as the G-band measurements at low ionic strength (5 mM HEPES) in order to drive the equilibrium to the bound complex form. Pelletier and Kraut argue that a certain ionic strength is required so that the proteins can slightly dissociate in order to rearrange and form a (or the) productive electron-transfer complex [Pelletier et al. 1992]. Cunha et al. found that at low ionic strength, the two proteins associate strongly in unproductive conformations that do not allow ET [Cunha et al. 1999]. It should be noted here that with EPR relaxation measurements one cannot distinguish unproductive protein complexes from productive ET complexes.

The frozen state of the protein samples may also have influenced the complex formation by cytochrome *c* and CcO<sub>II</sub>. In an NMR study on *c*<sub>552</sub> and CcO<sub>II</sub>, lowering the temperature by 15-20°C it was found that the equilibrium was shifted slightly to the bound state [Wienk et al. 2003]. The EPR samples were frozen slowly in liquid nitrogen and the equilibrium between bound state and unbound state may have been perturbed. This might have caused more unspecific binding of the two proteins.

The measurements described in this chapter were performed with truncated versions of both *c*<sub>552</sub> and CcO. A more interesting and more relevant system is four-subunit CcO in a membrane with full, membrane-anchor bearing *c*<sub>552</sub>. The extra metal centers that CcO contains in comparison to CcO<sub>II</sub> do not pose a big problem if the division method is applied. These measurements have been initiated at X-band, and some first promising results have already been obtained [Lyubenova 2006].

Another interesting application of dipolar relaxation measurements is the study of super-complex formation. These complexes are assumed to consist of varying amounts of (several of) the different proteins of the respiratory chain. The complexes have been shown to exist *in vitro* [Schägger 2002], and their function, composition and existence *in*



*vivo* is under debate. All the electron-transfer proteins contain paramagnetic centers, and EPR dipolar relaxation measurements would be suitable to help solve these problems.

#### 4.2.5. Conclusion

The spectrum and relaxation behavior of  $\text{Cu}_A$  in soluble subunit II of *Paracoccus denitrificans* CcO were measured using high-field EPR at 180 GHz. Some striking differences with X-band measurements were observed, such as the occurrence of different relaxation mechanisms that caused a different shape and faster decay of the echo signal at G-band.

The dipolar relaxation enhancement of  $\text{Cu}_A$  caused by the presence of heme a in a four-subunit CcO was studied by pulsed high-field EPR. The structure of the protein is known to great detail, hence it was deemed a useful system to test our simulation program. However, it was not possible to obtain structural information from the relaxation data, because in the studied temperature range, the heme a  $T_1$  relaxation rate was not high enough to reach the fast-motion regime where dipolar relaxation depends directly on the dipolar coupling strength.

For the first time, the formation of electron-transfer complexes was studied by pulse EPR. Electron spin echo decay measurements of the paramagnetic  $\text{Cu}_A$  center in the soluble subunit II of CcO were performed in the absence and presence of one of three cytochromes. Significant differences were seen in the dipolar relaxation enhancement of  $\text{Cu}_A$  between the negative control cytochrome  $c_1$  and the complex-forming cytochromes  $c_{552}$  and  $c_{hh}$ , such as the extent of the relaxation enhancement and the dependence on cytochrome concentration. Orientation dependence of dipolar relaxation was studied using G-band EPR measurements, but no anisotropy could be detected.

Simulations of the data at X-band and G-band frequencies were performed, both in a one-dimensional fashion (echo decay traces) as well as in two dimensions (echo decay traces as a function of spectral position). Comparison of the simulations with high-field relaxation data showed that there was more than one complex geometry present in our samples.



## Chapter 5. Model Systems for Distance Measurements

### 5.1. Results

To test the accuracy of our simulation program, especially the orientation dependence of dipolar relaxation, samples were required that have one well-defined geometry, unlike the cytochrome *c* – CcO<sub>II</sub> pair. For this purpose, organic molecules were synthesized in our group that contained two paramagnetic centers at a fixed distance from each other, and that had a fixed orientation of the interspin vector with respect to the *g*-tensors of the two spins. Their transverse relaxation was studied at different temperatures, and compared to similar molecules whose relaxation was not influenced by dipolar coupling.

#### 5.1.1. The Nitroxide Radical in Ni<sup>2+</sup>-octoethylporphyrin-TPA

Echo-detected field-swept spectra of Ni<sup>2+</sup>- octoethylporphyrin -TPA (Ni<sup>2+</sup>-NO<sup>•</sup>) were recorded. In an octahedral ligand field, Ni<sup>2+</sup> is paramagnetic with *S* = 1. Nevertheless, the system was treated as if there were no dipolar coupling of the nitroxide to the Ni<sup>2+</sup> ion; an assumption that is valid at G-band at temperatures higher than 20 K. As shown in figure 5.1, the transverse relaxation of the nitroxide radical becomes slower with increasing temperature up to 20 K. The T<sub>1</sub> relaxation of Ni<sup>2+</sup> is so fast at 20 K, that no dipolar relaxation effect is seen at this or at higher temperatures. In addition, the dipolar relaxation traces of Cu<sup>2+</sup>-NO<sup>•</sup>, which were obtained by dividing the Cu<sup>2+</sup>-NO<sup>•</sup> time traces by Ni<sup>2+</sup>-NO<sup>•</sup>, were fitted with T<sub>1</sub> values that agree very well with directly measured T<sub>1</sub> values of Cu<sup>2+</sup> (see later on). For these reasons, it was assumed that dipolar coupling to Ni<sup>2+</sup> did not influence nitroxide relaxation at temperatures above 20 K.

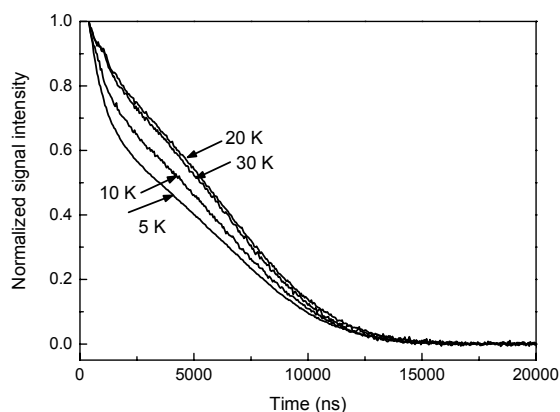


Figure 5.1. Transverse relaxation of the nitroxide in Ni<sup>2+</sup>-NO<sup>•</sup> dissolved in *otp*, with MeIm. Dipolar relaxation of the nitroxide by Ni<sup>2+</sup> has a minimum at *T* ≤ 5 K.

The nitroxide in Ni<sup>2+</sup>-NO<sup>•</sup> samples displays a typical nitroxide spectrum whose width is mainly determined by the *g*-anisotropy. The *g*- and hyperfine tensors are nearly collinear in nitroxide radicals, and therefore the *g*<sub>zz</sub> peak is split into three peaks by the large *z*-component of the hyperfine interaction. The much smaller *x* and *y* components of the hyperfine coupling are not resolved, due to unresolved hyperfine couplings to surrounding hydrogen atoms and other line-broadening mechanisms.

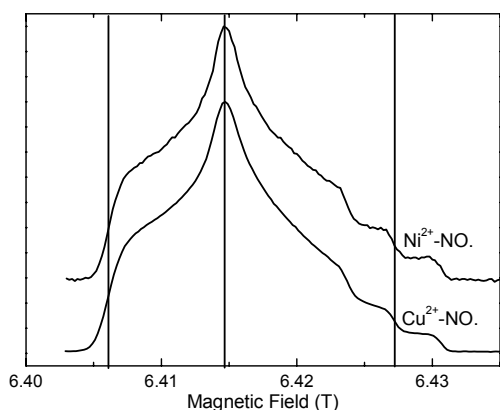
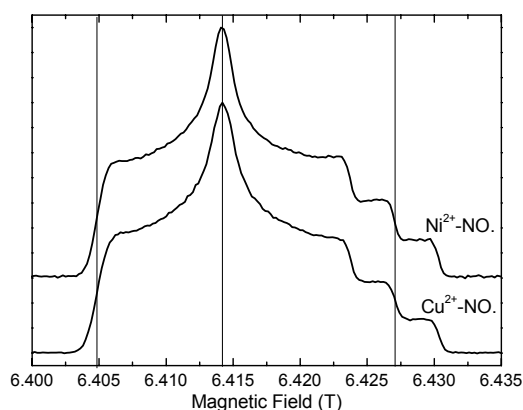


Figure 5.2. Field-swept spectra of the nitroxide of  $\text{Ni}^{2+}\text{-NO}\cdot$  and of  $\text{Cu}^{2+}\text{-NO}\cdot$ , both dissolved in otp. Temperature: 20 K. The vertical lines indicate the position of (from left to right)  $g_{xx}$ ,  $g_{yy}$  and  $g_{zz}$ .

It is well known that the  $g$ -values and hyperfine coupling of the nitroxide strongly depend on the polarity and the hydrogen-bonding capacity (proticity) of the solvent. The spectrum of the nitroxide of  $\text{Ni}^{2+}\text{-NO}\cdot$  dissolved in ortho-terphenyl is shown in figure 5.2, and in 3:7 chloroform: toluene (CT) in figure 5.3. Because the absolute magnetic field value was not accurately known for field-swept spectra taken at G-band, the spectra were lined up by their  $g_{zz}$  values. The  $g_{zz}$  value is not very sensitive to changes in the surroundings of the nitroxide radical. The  $g$  values differed depending on whether the nitroxide was dissolved in otp or in CT. The EPR parameters of the nitroxide radical in different solvents obtained by simulation of the spectra are given in table 5.1.

Figure 5.3. Field-swept spectra of the nitroxide of  $\text{Ni}^{2+}\text{-NO}\cdot$  and of  $\text{Cu}^{2+}\text{-NO}\cdot$ , both dissolved in CT. Temperature: 20 K. The vertical lines indicate the position of (from left to right)  $g_{xx}$ ,  $g_{yy}$  and  $g_{zz}$ .



solvent	$g_{xx}-g_{yy}$ ( $\cdot 10^3$ )	$g_{yy}-g_{zz}$ ( $\cdot 10^3$ )	$A_{zz}$ (mT)
ortho-terphenyl	2.9	4.0	3.4
3:7 chloroform: toluene	2.6	3.9	3.4

Table 5.1. EPR parameters of the nitroxide radical in  $\text{Ni}^{2+}\text{-NO}\cdot$  in different solvents, determined at G-band frequency. The absolute  $g$ -values are inaccurate because the magnetic field is not precisely known. Nevertheless, the field-swept spectra are very reproducible (as was also found for a  $\text{Mn}^{2+}$  in  $\text{MnO}$  standard) and the differences in  $g$ -values have an error of less than  $\pm 0.1 \cdot 10^{-3}$ . The accuracy of the  $A_{zz}$  values in this table is limited by the noise in the spectra, and could be determined with approximately  $\pm 0.2$  mT precision.

Transverse relaxation of the  $g_{yy}$  peak of the nitroxide spectrum of  $Ni^{2+}$ - $NO\cdot$  was studied at different temperatures. The echo decay traces of the nitroxide dissolved in otp or in CT measured at 50 K are shown in figure 5.4. Relaxation times  $T_2$  were determined for these samples by fitting the echo decay traces with a single exponential function. The  $T_2$  of  $Ni^{2+}$ - $NO\cdot$  in otp at temperatures below 90 K was determined by fitting the data with a stretched exponential function.

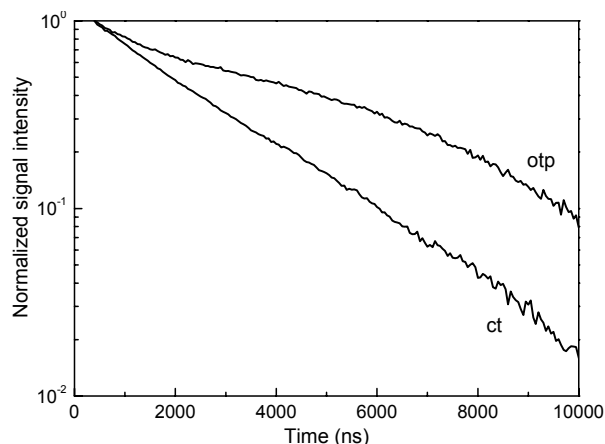


Figure 5.4. Echo decay traces at 50 K at the  $g_{yy}$  position of the nitroxide of  $Ni^{2+}$ - $NO\cdot$  dissolved in otp or in CT, both with MeIm.

These relaxation times have been plotted as a function of temperature in figure 5.5. The transverse relaxation of the nitroxide radicals is almost constant at low temperature. At approximately 70 K, the relaxation rate increases sharply with increasing temperature. It was suggested that this increase in transverse relaxation rate is caused by the rotation of the methyl groups in the nitroxide and in the surrounding solvent, of which the rate of rotation is comparable to the electron-nuclear coupling at temperatures between 80 and 200 K [Zecevic et al. 1998].

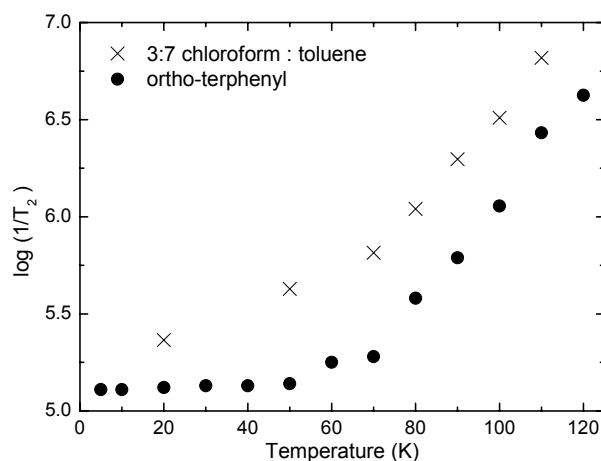


Figure 5.5.  $T_2$  relaxation times measured at the  $g_{yy}$  peak of the nitroxide radical in  $Ni^{2+}$ - $NO\cdot$  in two different solvents (both with MeIm) as shown in the plot.

The  $T_2$  relaxation of the nitroxide radical is strongly anisotropic. In figure 5.6, relaxation anisotropy of the nitroxide radical in  $Ni^{2+}$ - $NO\cdot$  is shown for two different solvents. Dissolved in the CT mixture, the relaxation of the nitroxide radical is slow at the canonical orientations ( $g_{xx}$ ,  $g_{yy}$  and  $g_{zz}$ ) with respect to the intermediate positions. These spectral positions therefore appear to become more intense at larger  $\tau$  values (or at higher temperatures) with respect to the rest of the spectrum. The relaxation anisotropy of the nitroxide radical dissolved in otp (figure 5.6) is very different. The high-field ( $g_{zz}$ ) part of the nitroxide spectrum relaxes more slowly than the rest of the spectrum, indicating that the rotational movement of the nitroxide is different in otp than in CT. This is most probably due to the much more bulky structure of otp (see discussion section).

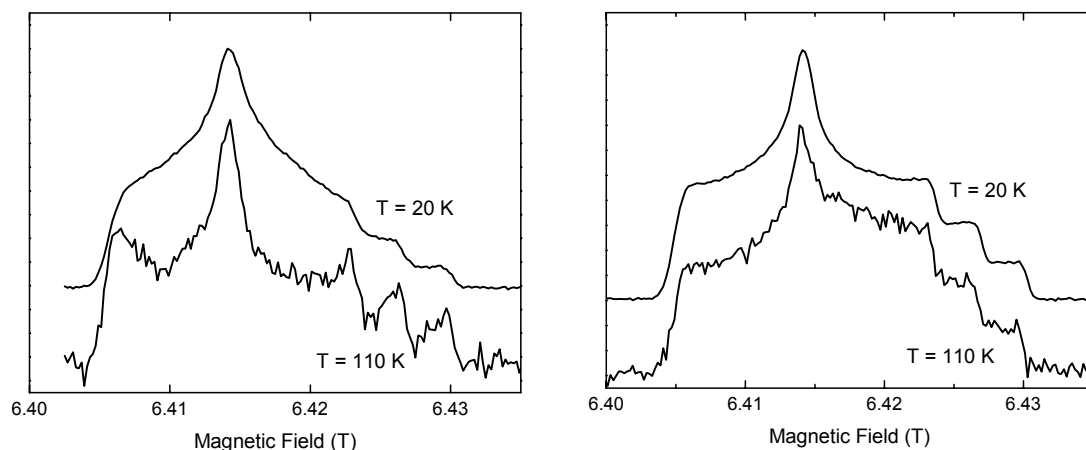


Figure 5.6.  $\text{Ni}^{2+}\text{-NO}\cdot$  dissolved in CT with MeIm (left) and in otp with MeIm (right) at 20 and 110 K, keeping  $\tau = 200$  ns.

### 5.1.2. The Nitroxide Radical and $\text{Cu}^{2+}$ in $\text{Cu}^{2+}$ -octoethylporphyrin-TPA

The nitroxide spectrum of  $\text{Cu}^{2+}$ - octoethylporphyrin-TPA (from here on:  $\text{Cu}^{2+}\text{-NO}\cdot$ ) dissolved in otp is shown in figure 5.2, dissolved in the CT mixture in figure 5.3. Comparison with the spectra of  $\text{Ni}^{2+}\text{-NO}\cdot$  shows that the nitroxide spectrum of  $\text{Cu}^{2+}\text{-NO}\cdot$  is identical to that of  $\text{Ni}^{2+}\text{-NO}\cdot$ .

To record the full  $\text{Cu}^{2+}$ , or even the  $\text{Cu}^{2+}$  and the nitroxide spectrum,  $\text{Cu}^{2+}\text{-NO}\cdot$  was measured by performing main-field sweeps (figure 5.7). At G-band frequency, unlike at X-band, the spectra of  $\text{Cu}^{2+}$  and of the nitroxide radical are very well separated. The field-swept spectrum of  $\text{Cu}^{2+}$  is 0.6 T wide. Even at 180 GHz the spectrum is axial; we determined  $g_{\perp} = 2.044$  and  $g_{\parallel} = 2.18$  for the sample dissolved in otp. The spectrum is determined by the anisotropic g-tensor. Whereas the  $g_{\perp}$  peak is very sharp, the  $g_{\parallel}$  edge is broadened by hyperfine interaction that is unresolved at this frequency; at X-band the copper and the nitrogen hyperfine lines can be resolved.

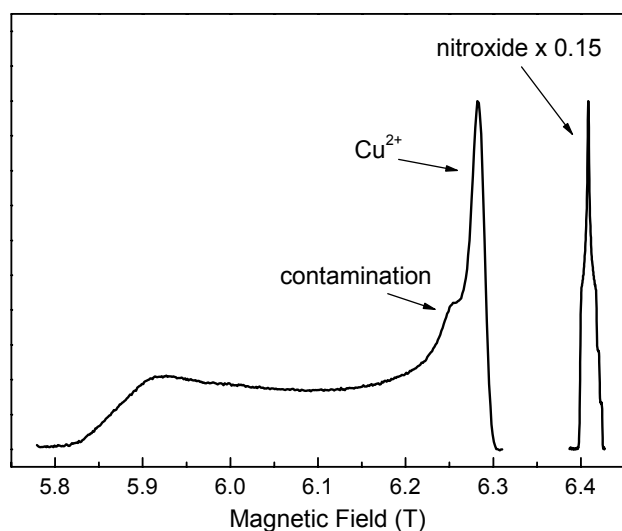
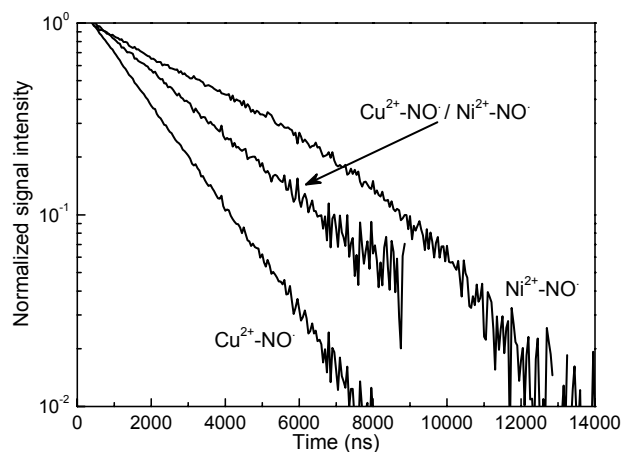


Figure 5.7. The G-band spectrum of  $\text{Cu}^{2+}\text{-NO}\cdot$  dissolved in otp with MeIm. The spectrum was measured by performing a main-field sweep over 0.8 T. The nitroxide spectrum was multiplied by 0.15 for clarity. Temperature: 20 K, other parameters as given in chapter 3.

### 5.1.3. Dipolar Relaxation Measurements of $\text{Cu}^{2+}$ -OEP-TPA

The dipolar relaxation measurements were mainly performed on  $\text{Cu}^{2+}$ -NO $\cdot$  dissolved in otp. As shown in figure 5.8, there is a significant difference in relaxation between equally concentrated samples of  $\text{Ni}^{2+}$ -NO $\cdot$  and  $\text{Cu}^{2+}$ -NO $\cdot$ . Division of the two traces removes the non-exponential curvature caused by intrinsic nitroxide relaxation. Figure 5.9 shows the temperature dependence of the dipolar relaxation of the nitroxide radical by the nearby  $\text{Cu}^{2+}$ . Dipolar relaxation was not studied at temperatures below 20 K, because there the dipolar coupling of the nitroxide to  $\text{Ni}^{2+}$  was apparent in the  $\text{Ni}^{2+}$ -NO $\cdot$  sample, and influenced the relaxation behavior of the nitroxide (see above).

Figure 5.8. Echo decay traces of  $\text{Ni}^{2+}$ -NO $\cdot$  and  $\text{Cu}^{2+}$ -NO $\cdot$  measured at the  $g_{yy}$  position of the nitroxide at 70 K. The middle trace was obtained by dividing the echo decay trace of  $\text{Cu}^{2+}$ -NO $\cdot$  by the trace of  $\text{Ni}^{2+}$ -NO $\cdot$ . This way, the non-exponential intrinsic signal decay of the nitroxide is divided out and only the single-exponential dipolar relaxation contribution is left.



For  $\text{Cu}^{2+}$ -NO $\cdot$ , the signal decay caused by dipolar coupling shows single exponential behavior at all temperatures, and the relaxation time decreased continuously from 20 to 120 K (figure 5.9). From this we deduced that the  $\text{Cu}^{2+}$   $T_1$  relaxation rate at 120 K is smaller than the dipolar coupling, which means the measurements were all performed in the low-temperature regime where  $T_2^{\text{dip}} = T_{1f}$ . G-band EPR measurements could not be performed at temperatures higher than 120 K, because the intrinsic  $T_2$  relaxation rate of the nitroxide became so high that no echo could be detected.

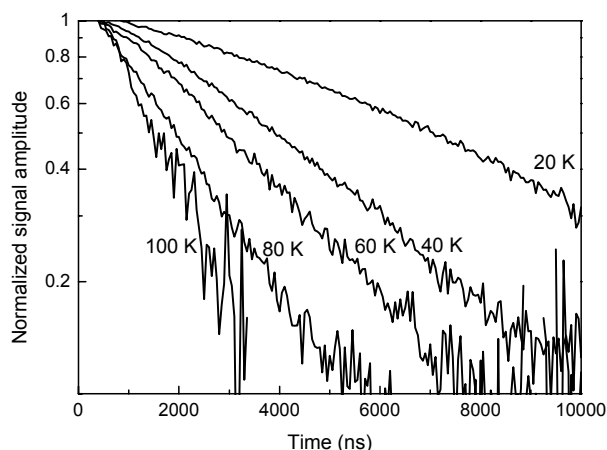
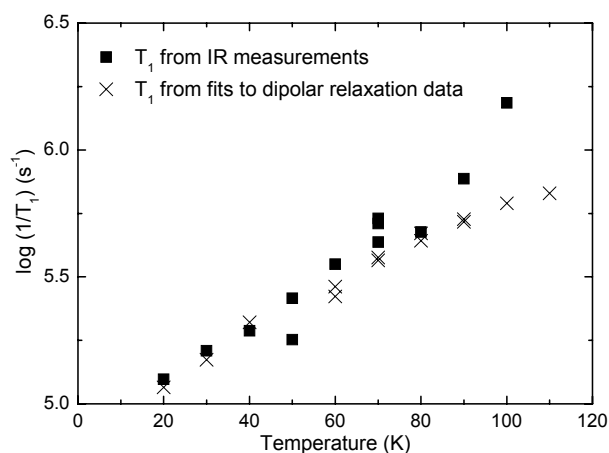


Figure 5.9. Temperature dependence of dipolar relaxation enhancement of the nitroxide in  $\text{Cu}^{2+}$ -NO $\cdot$ . Dipolar relaxation traces at different temperatures as indicated in the plot. The measurements were performed at the maximum ( $g_{yy}$ ) of the nitroxide signal. All relaxation traces are well described by a single exponential function.

By fitting the dipolar relaxation traces  $T_2^{\text{dip}}$ , and thereby  $T_{1f}$ , was determined. These  $T_1$  values agreed very well with  $\text{Cu}^{2+}$   $T_1$  values measured at G-band using the inversion recovery sequence (figure 5.10). However, the measurements were all performed in the low-temperature regime, and no structural parameters could be obtained from simulations.

The difference in temperature dependence of  $T_1$  relaxation at X-band and at G-band will be discussed in the next chapter.

Figure 5.10.  $T_1$  relaxation of  $\text{Cu}^{2+}$  in  $\text{Cu}^{2+}\text{-NO}\cdot$  dissolved in *otp* with MeIm. The  $T_1$  was determined by IR measurements, or by fitting the dipolar relaxation traces such as those in figure 5.9 with a  $T_1$  value as explained in the text. The different types of measurement do not agree at high temperature, because sub- $\mu\text{s}$   $T_1$  can not be measured accurately with the current G-band spectrometer setup.



Although simulations with the  $T_1$  value of  $\text{Cu}^{2+}$  even at 110 K do not display any relaxation anisotropy, field-swept measurements of the nitroxide were taken at this temperature to look for relaxation anisotropy. The resulting spectra are shown in figure 5.11. There was clear anisotropic relaxation, but it was identical to the relaxation anisotropy observed for the  $\text{Ni}^{2+}\text{-NO}\cdot$  sample (compare with figure 5.6, right plot), and was thus caused exclusively by intrinsic nitroxide relaxation.

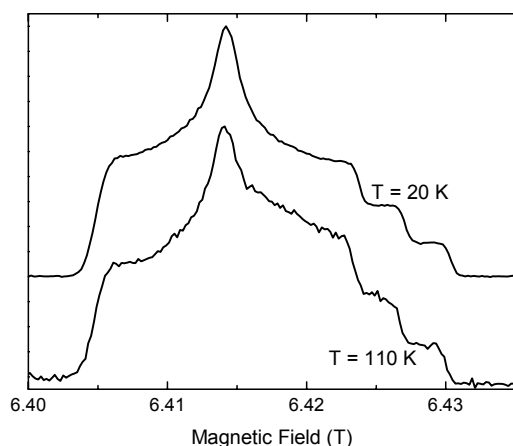


Figure 5.11.  $\text{Cu}^{2+}\text{-NO}\cdot$  in *otp* with MeIm at 20 and 110 K with  $\tau = 200$  ns. The anisotropy of nitroxide relaxation was identical for the  $\text{Cu}^{2+}\text{-NO}\cdot$  sample as for the  $\text{Ni}^{2+}\text{-NO}\cdot$  sample (see figure 5.6, right).

#### 5.1.4. Nitroxide $T_2$ Dependence on Different Solvents

To make the high-temperature regime accessible for dipolar relaxation measurements, different solvents and axial ligands to  $\text{Cu}^{2+}$  were used to increase nitroxide  $T_2$  relaxation time. The dominating relaxation mechanisms were assumed to be coupling to solvent protons and rotation of nearby methyl groups. Therefore, toluene in the CT mixture was exchanged with deuterated toluene ( $d_8$ -toluene) or with benzene. Additionally, MeIm was substituted by pyridine, which does not contain methyl groups. The sample was also dissolved in tetrahydrofuran (THF). The echo decay traces of  $\text{Cu}^{2+}\text{-NO}\cdot$  in these solvents are shown in figure 5.12. The  $T_2$  relaxation of the nitroxide in  $\text{Cu}^{2+}\text{-NO}\cdot$  dissolved in benzene was significantly faster than for  $\text{Cu}^{2+}\text{-NO}\cdot$  in the CT mixture.



Dissolved in THF, the nitroxide relaxed extremely fast, even at a temperature as low as 20 K. The fast relaxation might have been caused by clustering of the  $\text{Cu}^{2+}$ -NO $\cdot$  molecules. The right plot in figure 5.12 shows that exchanging toluene by d8-toluene and substituting MeIm for pyridine had no effect on the  $T_2$  relaxation of the nitroxide. When the nitroxide was dissolved in otp, the  $T_2$  relaxation was significantly slower than for any other solvent used.

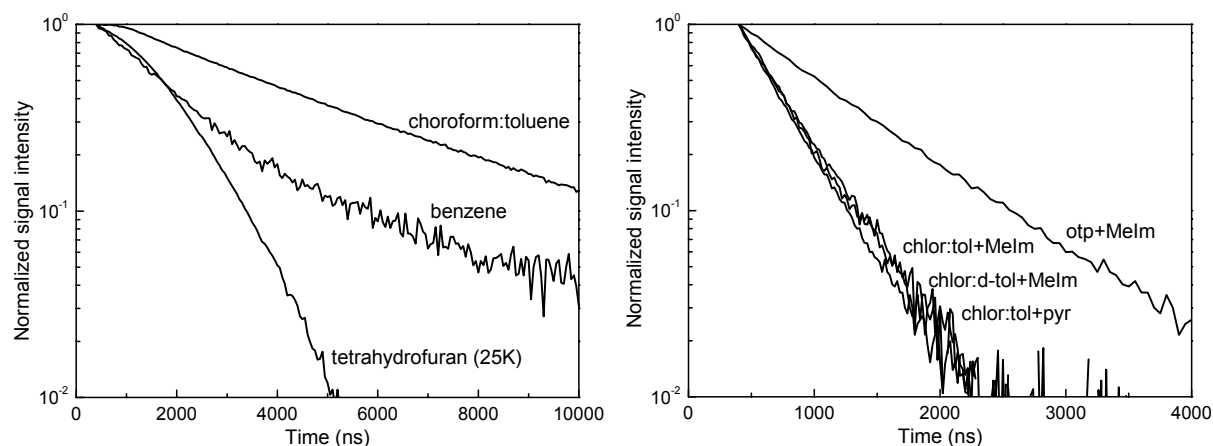


Figure 5.12. Echo decay traces at the nitroxide  $g_{yy}$  position in  $\text{Cu}^{2+}$ -NO $\cdot$  dissolved in various solvents as indicated. chlor, chloroform; tol, toluene; d-tol, fully deuterated toluene; pyr, pyridine. Chloroform to toluene ratio was always 3:7, MeIm or pyridine was added in molar excess. Temperature: 20 K (left) and 90 K (right), except for the tetrahydrofuran curve measured at 25 K.

### 5.1.5. Simulations of $\text{Cu}^{2+}$ -OEP-TPA

Simulations performed with the structural parameters of the  $\text{Cu}^{2+}$ -NO $\cdot$  molecule show pronounced nitroxide relaxation anisotropy if  $T_{1f} = 0.5 \mu\text{s}$ , as shown in figure 5.13. The structural parameters were obtained from the crystal structure of  $\text{Ni}^{2+}$ -NO $\cdot$  and the distance was verified by PELDOR measurements at X-band [Bode]. By PELDOR an exchange coupling of approximately 2.5 MHz had been found. Simulations with various values for the exchange coupling  $J$  demonstrate that it is possible to determine not only the size, but also the sign of  $J$  by high-field relaxation measurements (figure 5.13).

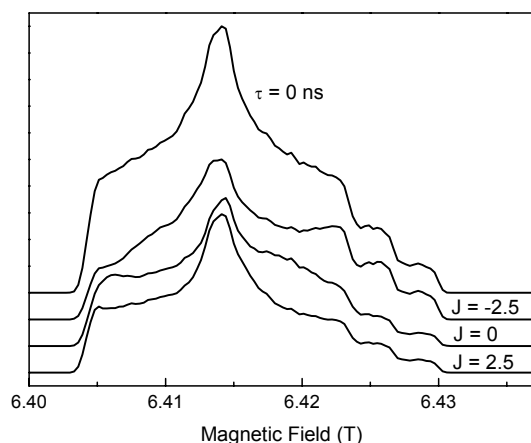


Figure 5.13. Simulations of field-swept spectra of the nitroxide in  $\text{Cu}^{2+}$ -NO $\cdot$  that relaxes anisotropically due to dipolar coupling to  $\text{Cu}^{2+}$ .  $\tau = 200 \text{ ns}$  ( $\tau = 0 \text{ ns}$  spectrum is shown for comparison) and  $T_{1f} = 0.5 \mu\text{s}$ . The spectra were simulated with parameters derived from the molecular structure:  $r = 2.1 \text{ nm}$ ,  $\theta_D = 90^\circ$ ,  $\varphi_D = 36^\circ$ ,  $\alpha = \beta = \gamma = 0^\circ$ ,  $J$  variable as given in the plot.

### 5.1.6. Relaxation Measurements of Mn<sup>2+</sup>-terpyridine-TPA

The field-swept EPR spectrum of Mn<sup>2+</sup>-terpyridine-TPA (Mn<sup>2+</sup>-NO<sup>•</sup>), dissolved in dimethyl-formamide (DMF), is shown in figure 5.14. The isotropic g-value of Mn<sup>2+</sup> in an octahedral ligand environment ( $g_{\text{iso}} = 2.00101$ ) is very similar to the g-values of the nitroxide (2.008 to 2.001), and consequently, the spectra overlap even at G-band frequency. Mn<sup>2+</sup> has  $S = 5/2$ , but at a magnetic field as high as 6.4 T, the main transition observed is between the  $S = +1/2$  and  $S = -1/2$  levels, because the other transitions are broadened by large zero-field splitting terms. The high-field Mn<sup>2+</sup> spectrum is dominated by six hyperfine lines due to the coupling of the electrons to the manganese nucleus, which has  $I = 5/2$ .

Mn<sup>2+</sup> is a high-spin system, therefore the pulse length required for a  $\pi$ -pulse is three times smaller than that for a  $\pi$ -pulse for a  $S = 1/2$  system. The experimental parameters for the spectrum in figure 5.14 were optimized to the nitroxide signal, and consequently, the Mn<sup>2+</sup> signal is distorted. Nevertheless, the position of the Mn<sup>2+</sup> peaks can be discerned in the spectrum.

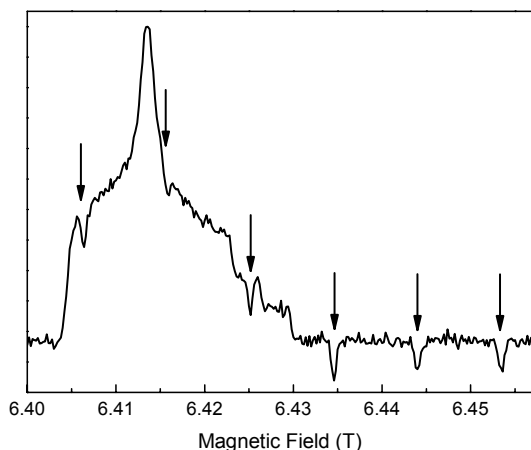


Figure 5.14. Field-swept spectrum of Mn<sup>2+</sup>-terpyridine-TPA in DMF. The positions of the Mn<sup>2+</sup> lines are shown by the arrows, and are 9.4 mT apart. The phase of the Mn<sup>2+</sup> spectrum is incorrect, because the pulses were adjusted to the ( $S = 1/2$ ) nitroxide radical. Temperature: 50 K.

The relaxation behavior of the nitroxide in Mn<sup>2+</sup>-NO<sup>•</sup> was studied and compared to the relaxation behavior of the nitroxide in the terpyridine ligand without any metal ion bound (from here on referred to as terpy-NO<sup>•</sup>). Echo decay traces were measured 1.5 mT to the low-field side of the  $g_{yy}$  peak of the nitroxide, because the high-field side of the  $g_{yy}$  peak was distorted due to the second Mn<sup>2+</sup> hyperfine line (see figure 5.14). Figure 5.15 shows the relaxation behavior of the nitroxide radical in terpy-NO<sup>•</sup> and of the nitroxide in Mn<sup>2+</sup>-NO<sup>•</sup> at different temperatures. To obtain the pure dipolar relaxation, the Mn<sup>2+</sup>-NO<sup>•</sup> echo decay traces were divided by the terpy-NO<sup>•</sup> decay traces. As can be seen in figure 5.15, the difference between the Mn<sup>2+</sup>-NO<sup>•</sup> and terpy-NO<sup>•</sup> nitroxide relaxation traces at 100 K is so small, that the resulting division trace is dominated by noise. Therefore, only the division traces at 70 K and 80 K are shown.

The dipolar relaxation of Mn<sup>2+</sup>-NO<sup>•</sup> displayed single exponential decay behavior. The decay traces were fitted with a time constant  $T_2^{\text{dip}}$ , and because the measurements were performed in the low-temperature region,  $T_2^{\text{dip}}$  was assumed to be equal to  $T_{1f}$ . Contrary to our expectations, the  $T_1$  relaxation of Mn<sup>2+</sup> was very similar to the relaxation of Cu<sup>2+</sup>. Because the intrinsic nitroxide  $T_2$  relaxation in the Mn<sup>2+</sup>-NO<sup>•</sup> system shows a similar temperature dependence as in the Cu<sup>2+</sup>-NO<sup>•</sup> system (as shown in figure 5.16), we were unable to detect a nitroxide signal at temperatures higher than 110 K. Dipolar

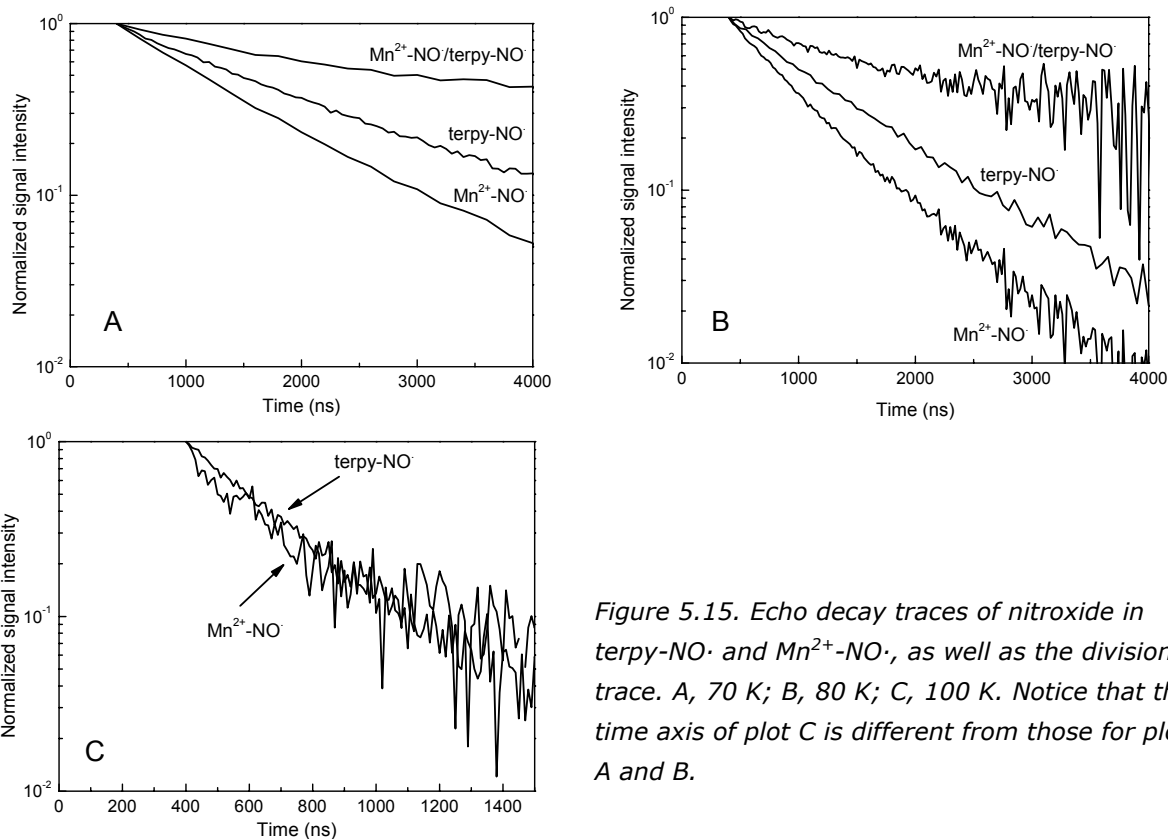


Figure 5.15. Echo decay traces of nitroxide in  $\text{terpy-NO}\cdot$  and  $\text{Mn}^{2+}\text{-NO}\cdot$ , as well as the division trace. A, 70 K; B, 80 K; C, 100 K. Notice that the time axis of plot C is different from those for plots A and B.

relaxation anisotropy was not expected in the low-temperature limit below 100 K, and it was indeed not detected. Figure 5.17 shows the field-swept spectra of  $\text{terpy-NO}\cdot$  and of  $\text{Mn}^{2+}\text{-NO}\cdot$  at high temperature. The intrinsic nitroxide relaxation was anisotropic, and this anisotropy was the same for the  $\text{terpy-NO}\cdot$  and for  $\text{Mn}^{2+}\text{-NO}\cdot$  (although in  $\text{Mn}^{2+}\text{-NO}\cdot$  the  $\text{Mn}^{2+}$  lines overlap the nitroxide spectrum).

Figure 5.16.  $T_2$  values of nitroxide in  $\text{terpy-NO}\cdot$  and  $T_2^{\text{dip}}$  values from dipolar relaxation measurements of  $\text{Mn}^{2+}\text{-NO}\cdot$ . At temperatures higher than 80 K, the signal decays of  $\text{Mn}^{2+}\text{-NO}\cdot$  and  $\text{terpy-NO}\cdot$  were very fast and no reliable data could be obtained.

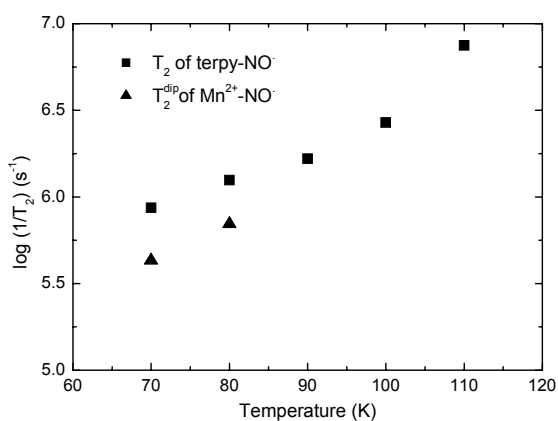
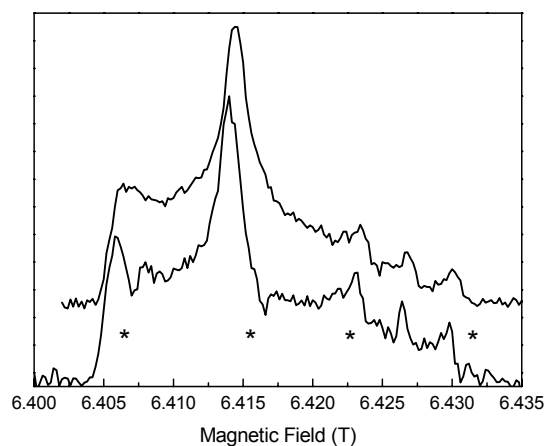


Figure 5.17. Relaxation anisotropy of nitroxide: spectra of terpy-NO $\cdot$  (upper trace) and Mn $^{2+}$ -NO $\cdot$  at 90 K with  $\tau = 450$  ns. The positions of Mn $^{2+}$  lines are marked by asterisks.



All structural parameters of Mn $^{2+}$ -NO $\cdot$  are known, and as there is no exchange coupling (see section 3.2.4), the dipolar relaxation could be simulated with no free parameters. Figure 5.18 shows such a simulation for  $T_{1f} = 0.5$   $\mu$ s. A strong anisotropy at large  $\tau$  values, caused by dipolar relaxation, is observed.

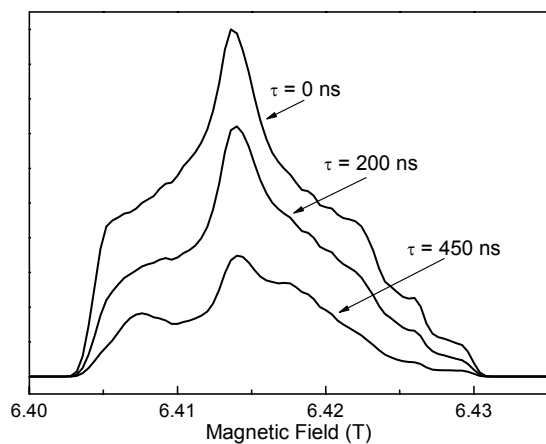


Figure 5.18. Simulation of field-swept spectra with different  $\tau$  values of the nitroxide in Mn $^{2+}$ -NO $\cdot$  for  $T_{1f} = 0.5$   $\mu$ s. Other simulation parameters:  $r = 2.7$  nm,  $\theta_D = 90^\circ$ ,  $\varphi_D = 25^\circ$ , Euler angles =  $0^\circ$ ,  $J = 0$  MHz.

## 5.2. Discussion

### 5.2.1. The Nitroxide

The EPR spectra of the nitroxide radicals in  $\text{Ni}^{2+}\text{-NO}\cdot$  and in  $\text{Cu}^{2+}\text{-NO}\cdot$  displayed  $g$ -values and an  $A_{zz}$  typical of this type of organic radicals. There was a small difference in  $g$ -values between the radicals dissolved in otp and those in CT. This can be ascribed to a difference in polarity between the two solvents, because these EPR parameters are very sensitive to changes in solvent polarity and proticity.

The intrinsic  $T_2$  relaxation of the nitroxide at low temperature ( $T < 70$  K) is caused by cross relaxation due to coupling to nuclei, mainly protons, in the surrounding solvent. This relaxation process is temperature independent, and indeed the  $T_2$  relaxation is nearly constant up to 60 K (see figure 5.5). Between 70 K and 150 K, the rate of the rotation of methyl groups is comparable to the electron-nuclear coupling, causing an efficient relaxation pathway [Zecevic et al. 1998]. This process is strongly temperature dependent and dominates the  $T_2$  relaxation as can be seen in figure 5.5. This relaxation was mainly caused by the methyl groups on the nitroxide moiety; changing the axial ligand MeIm to methyl group-less pyridine had no effect on the  $T_2$  relaxation of the nitroxide. No echo signal from the nitroxide radical could be detected at temperatures higher than 140 K due to the fast  $T_2$  relaxation. The dipolar relaxation enhancement became less well observable at higher temperature, because it was covered by the fast intrinsic relaxation of the nitroxide, and because the signal-to-noise ratio decreased drastically.

The  $T_2$  relaxation of the nitroxide at G-band was faster than the relaxation at X-band. This may be due to the increased Zeeman splitting at G-band, because modulation of the  $g$ -tensor is a relaxation process that becomes more effective at higher magnetic fields [Prisner 1997]. A similar field dependence of  $T_2$  relaxation of Fremy's salt was found in a previous relaxation study [Kirilina et al. 2005].

The nitroxide relaxation was very different when the solvent was otp than when it was CT. The relaxation rate was higher in CT than in otp, and the shape of the echo decay traces was markedly different, especially at low temperature (see figure 5.4). The  $T_2$  relaxation of the nitroxide in CT shows single-exponential behavior, corresponding to one dominating relaxation process or to the product of different exponential relaxation processes. In contrast, in otp this relaxation process is non-Markoffian, as is seen by the stretched exponential shape of the echo decay curves up to 90 K [Klauder et al. 1962]. Similar behavior was found for  $\text{Cu}_A$  in  $\text{CcO}_{II}$  (see chapter 4). Relaxation anisotropy was only observed at higher temperature, where a different relaxation process dominated and the signal decay became exponential.

Nitroxide relaxation was strongly dependent on spectral position. This was caused by rotation of the nitroxide together with nearby solvent molecules. The  $\text{Ni}^{2+}\text{-NO}\cdot$  molecule reorients due to the motion of the surrounding molecules, which is mainly determined by the properties of the solvent glass [Kirilina et al. 2004]. The fact that the relaxation anisotropy of  $\text{Ni}^{2+}\text{-NO}\cdot$  in CT and in otp solution were different can therefore be explained by the differences in molecular structure of the solvent molecules: chloroform and toluene are very small molecules compared to ortho-terphenyl, and their motion is therefore different.

### 5.2.2. Dipolar Relaxation by Ni<sup>2+</sup>

When MeIm was added to the Ni<sup>2+</sup>-NO· sample, the relaxation of the nitroxide at low temperature was enhanced by the presence of Ni<sup>2+</sup>. Ni<sup>2+</sup> is paramagnetic when it is octahedrally coordinated, and has  $S = 1$ . At X-band, dipolar relaxation enhancement of the nitroxide is seen up to 60 K, but because no relaxation enhancement was detected at G-band above 20 K (figure 5.1 and 5.5), it was concluded that the  $T_1$  relaxation of Ni<sup>2+</sup> is much faster at G-band.

The anisotropy of dipolar relaxation caused by Ni<sup>2+</sup> was studied at 5 K, but no anisotropy between  $g_{xx}$  and  $g_{yy}$  of the nitroxide was detected. This might be explained by the presence of exchange interaction, which had been detected in the analogous molecule Cu<sup>2+</sup>-NO· [Bode]. Exchange interaction is isotropic, and consequently less or no relaxation anisotropy could be expected. However, simulations indicate that for sufficiently small  $J$  (such as in this case), dipolar relaxation should still be anisotropic. In a dipolar relaxation study of tyrosyl radicals in photosystem II, it was found that although high-spin ( $S = 2$ ) iron enhanced the relaxation of the tyrosyl, it caused no relaxation anisotropy. This was ascribed to the fact that the anisotropy of Fe<sup>2+</sup> dominated the relaxation anisotropy [Lakshmi et al. 2003]. The same effect might occur for Ni<sup>2+</sup> in our measurements.

In the following discussion, it is assumed that no dipolar relaxation enhancement of the nitroxide by Ni<sup>2+</sup> takes place above 20 K.

### 5.2.3. Dipolar Relaxation by Cu<sup>2+</sup>

The G-band EPR spectrum of Cu<sup>2+</sup> was recorded by sweeping the main magnetic field, and a typical Cu<sup>2+</sup> spectrum was obtained. The  $g$ -values determined at G-band were in good agreement with those found by [Cunningham et al. 1997] for a very similar molecule at X-band. The hyperfine couplings were not resolved at this frequency because of line-broadening effects. At X-band, both the Cu<sup>2+</sup> and the nitrogen hyperfine interactions can be detected, and the latter are in fact an indication that no stacking of the Cu<sup>2+</sup> porphyrin moieties occurs [Cunningham et al. 1997]. One of the Cu<sup>2+</sup>-NO· samples measured in this study was checked at X-band and it was found that the addition of 1-methylimidazole (MeIm) to the sample prevented stacking so that the nitrogen hyperfine pattern on the Cu<sup>2+</sup> signal could be resolved. The half-field signal caused by strong nitroxide-Cu<sup>2+</sup> interaction that could be seen due to binding of the nitroxide to Cu<sup>2+</sup> also disappeared upon the addition of MeIm [Bode].

The presence of Cu<sup>2+</sup> also caused dipolar relaxation enhancement of nitroxide  $T_2$  relaxation. The pure dipolar relaxation traces, obtained by dividing echo decay traces of the nitroxide in Cu<sup>2+</sup>-NO· by those of the nitroxide in Ni<sup>2+</sup>-NO·, were single exponentials between 20 and 100 K (as shown in figure 5.9). At 100 K, the  $T_1$  of Cu<sup>2+</sup> was 1.5  $\mu$ s, which is appreciably larger than  $\Delta^{-1}$  (which is approximately 0.02  $\mu$ s), meaning that the measurements were all performed in the low-temperature region. Nevertheless, simulations showed very slight relaxation anisotropy at 90 K. This was, however, not detected experimentally due to the low signal-to-noise ratio at this temperature, and

because of the intrinsic relaxation anisotropy of the nitroxide that covered up smaller anisotropic relaxation effects.

The most ideal solvent for our dipolar relaxation measurements was ortho-terphenyl. The nitroxide relaxation was slowest in this solvent. Toluene has a phase transition at higher temperature, causing the dissolved molecules to partially orient in the sample tube and creating distortions in the EPR spectrum. This behavior was not found in otp for temperatures up to room temperature. Additionally, otp is solid at room temperature, which made sample handling and storing more easy. The fact that  $\text{Cu}^{2+}$ -NO $\cdot$  formed aggregates in THF was surprising, as a very similar solvent, 2-methyl-THF, was found previously to be a good solvent for  $\text{Cu}^{2+}$ -OEP [Cunningham et al. 1997]. It was mentioned, however, that other porphyrins did not dissolve well in 2-methyl-THF.

At high temperatures, where  $1/T_{1f} \gg \Delta$ , the simulations showed large relaxation anisotropy. They indicate that high-field relaxation measurements may be used to determine the size and the sign of the exchange coupling; different anisotropy patterns emerge when  $J$  is varied (figure 5.13). No anisotropic dipolar relaxation was observed experimentally, because at temperatures above 120 K no echo signal from the nitroxide radical could be detected due to the short  $T_2$  relaxation time of the nitroxide.

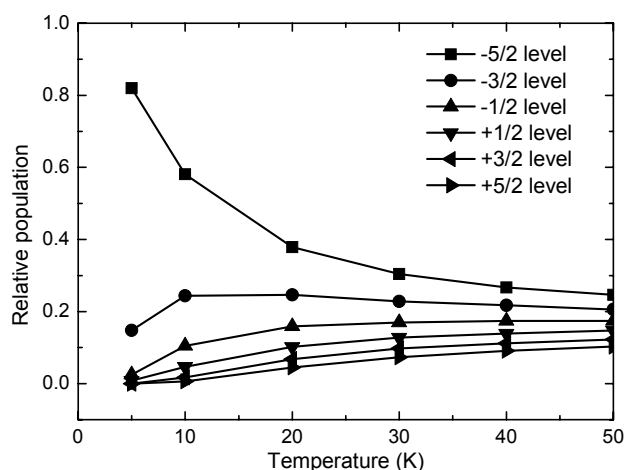
$T_1$  relaxation of  $\text{Cu}^{2+}$  at G-band, determined by fitting the dipolar relaxation data, differed markedly from  $T_1$  measurements performed at X-band [Fielding et al. 2006]. This topic will be further discussed in the next chapter.

#### 5.2.4. Dipolar Relaxation by $\text{Mn}^{2+}$

The  $T_2$  relaxation of nitroxide is enhanced by the presence of  $\text{Mn}^{2+}$ .  $\text{Mn}^{2+}$  is a high-spin system with large zero-field splitting, and the  $T_1$  relaxation was expected to be faster than that found for  $\text{Cu}^{2+}$ . Moreover, the  $T_1$  of  $\text{Mn}^{2+}$  at X-band at low temperatures was much shorter than that of  $\text{Cu}^{2+}$  [Bode]. Yet, the  $T_1$  values of  $\text{Mn}^{2+}$  found by the dipolar relaxation method at G-band were very similar to those for  $\text{Cu}^{2+}$  at G-band. The results for  $\text{Cu}^{2+}$ -NO $\cdot$  and  $\text{Mn}^{2+}$ -NO $\cdot$  were therefore quite similar: at temperatures up to 90 K, the dipolar relaxation was mono-exponential. The dipolar relaxation at higher temperatures could not be determined, because the nitroxide  $T_2$  became too short.

It was difficult to study relaxation anisotropy in the  $\text{Mn}^{2+}\text{-NO}\cdot$  system, on the one hand because of the intrinsic anisotropic relaxation of the nitroxide, and on the other hand because four of the six  $\text{Mn}^{2+}$  hyperfine lines were superimposed on the nitroxide spectrum. Although  $\text{Mn}^{2+}$  had a shorter  $T_2$  than the nitroxide, the  $S = +1/2$  and  $S = -1/2$  energy levels become more populated at higher temperature (see figure 5.19) due to Boltzmann's law. Therefore, the  $\text{Mn}^{2+}$  signal increased relative to the nitroxide signal when the temperature was increased, making the nitroxide spectrum -and dipolar relaxation anisotropy- more difficult to study.

Figure 5.19. Relative population of the electronic energy levels of  $\text{Mn}^{2+}$  at G-band frequency (180 GHz). The  $-1/2$  and  $+1/2$  levels are increasingly populated with rising temperature. The intensity of the six sharp  $\text{Mn}^{2+}$  peaks (originating from the  $-1/2$  to  $+1/2$  transition) at G-band increases with temperature, despite the decrease in  $T_2$ .





### 5.2.5 Conclusions

To test our experimental setup and our simulation program, the dipolar relaxation enhancement of metal ions on a nitroxide in several model complexes was studied. In complexes with  $\text{Cu}^{2+}$  and  $\text{Mn}^{2+}$ , relaxation enhancement was observed, and in the case of  $\text{Cu}^{2+}$  the dipolar relaxation could be simulated very well with  $T_1$  values that were in agreement with direct measurements of  $\text{Cu}^{2+}$   $T_1$  relaxation. However, due to the fast  $T_2$  relaxation of the nitroxide, dipolar relaxation measurements were restricted to temperatures below approximately 100 K. Consequently, all measurements were performed in the low-temperature region of dipolar relaxation enhancement, because the  $T_1$  relaxation rate of  $\text{Cu}^{2+}$  and  $\text{Mn}^{2+}$  was much smaller than the dipolar coupling at 100 K. In this temperature region dipolar relaxation depends only on  $T_{1f}$ , and not directly on structural parameters. Hence, no structural information could be obtained from our measurements.

As a test of our simulation program, high-field relaxation measurements should be performed on a model system where the fast-relaxing spin has a much shorter  $T_1$  at low temperature. Low-spin iron, such as the iron found in cytochrome *c*, would be a very good candidate. In fact, relaxation studies have been performed on spin-labeled iron-containing proteins, such as hemoglobin [Budker et al. 1995; Seiter et al. 1998]. The authors only focused on the distance, however, and did not attempt to disentangle the orientation of the dipolar vector –something that would have been difficult at X-band frequency, due to the lack of orientation selectivity.

The nitroxide spin label should be restricted in its motion in order to be able to observe relaxation anisotropy: full rotational freedom would average out all angular dependence, but small-angle fluctuations may still cause observable anisotropy of dipolar relaxation.

Relaxation anisotropy might also be observable in the  $\text{Ni}^{2+}$ -NO $\cdot$  pair, if the triple bond between the linker and TPA is replaced by an ester bond, as in  $\text{Mn}^{2+}$ -NO $\cdot$ . This would strongly reduce the exchange coupling to  $\text{Ni}^{2+}$ .

A better choice for a slow-relaxing spin would be one whose relaxation is isotropic, because the anisotropic relaxation of the nitroxide may cover up the dipolar relaxation. However, the spin should have a spectrum that is broad enough to do orientation-selective measurements on. Quinones or tyrosine radicals are possible candidates, but they are not stable and make sample preparation and handling much more demanding.



## Chapter 6. $T_1$ Relaxation Measurements

### 6.1. Results

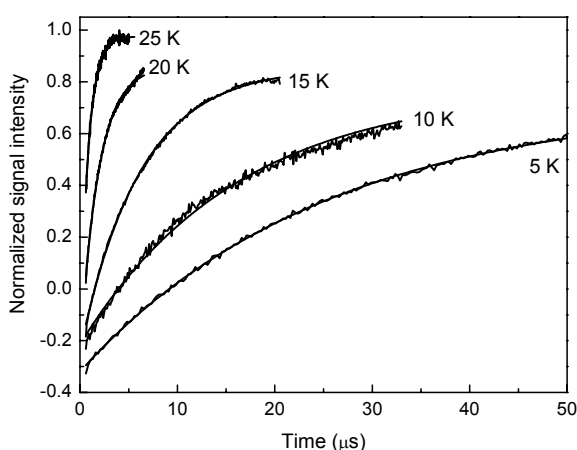
The accurate knowledge of  $T_1$  relaxation behavior of the fast-relaxing spin partner in dipolar relaxation experiments is crucial for the quantitative analysis of such measurements. Some relaxation processes depend on magnetic field, as already indicated in the previous two chapters, and no G-band  $T_1$  relaxation data is known for the systems we studied. We therefore investigated the field dependence of longitudinal relaxation in more detail.

Using primarily the inversion recovery experiment, we measured  $T_1$  relaxation of  $\text{Cu}_A$  and  $\text{Cu}^{2+}$  (in  $\text{Cu}^{2+}\text{-NO}\cdot$ ) at different temperatures. The relaxation times of cytochrome *c* heme and heme *a* in CcO could not be directly measured at G-band, but we studied their dependence on temperature using the  $T_1$  values obtained from dipolar relaxation measurements.

#### 6.1.1. $\text{Cu}_A$

The longitudinal relaxation of  $\text{Cu}_A$  in CcO<sub>II</sub> was investigated by inversion recovery (IR) measurements and by studying the dependence of the echo intensity on the repetition time of the experiment (RT experiment). In figure 6.1 the IR traces of  $\text{Cu}_A$  in CcO<sub>II</sub> measured between 5 and 25 K at G-band frequency are shown. The dead time of the experiment was quite large (600 ns), because the unwanted echo created by the first and second pulses of the IR sequence would otherwise overlap with the echo of interest. The unwanted echo could not be removed by phase-cycling, as the G-band spectrometer has only one excitation channel. For more details about the IR experiment at G-band, see appendix B.

Figure 6.1. IR traces of  $\text{Cu}_A$  in CcO<sub>II</sub>. Protein concentration: 0.2 mM (5 K and 10 K) and 1 mM (15 to 25 K). Measurements were performed at the  $\text{Cu}_A$  signal maximum ( $g_{yy}$ ,  $B_0 = 6.362$  T). Single exponential fits are shown as noiseless lines.



The signal could not be completely inverted, as can be seen in figure 6.1: the IR traces, extrapolated to time = 0 ns do not start at -1, which would mean full inversion, but at -0.3 (at 5 K). This is due to the fact that the whole EPR spectrum of  $\text{Cu}_A$  could not be inverted by the microwave pulse and because of the signal decay within the (large) dead time of the experiment. Nevertheless, the IR traces could be well simulated by a single exponential function, as shown in figure 6.1 by the noiseless traces. A second

component from spectral diffusion was not observed, probably because this fast-relaxing component had fully recovered within the spectrometer dead time. The first few points of the IR traces measured at 5, 10 and 15 K in figure 6.1 are not well simulated by the single exponential function: this might be a small contribution from spectral diffusion.

The binuclear copper center  $\text{Cu}_A$  has a relatively high  $T_1$  relaxation rate at X-band [Scholes et al. 1984]. A fast  $T_1$  relaxation was also found in nitrous reductase, an enzyme that contains a  $\text{Cu}_A$  center very similar to the one found in CcO.  $\text{Cu}_A$  consists of two strongly coupled copper ions, with a covalent bond between them. Wobbling modes of this copper-copper center may suffice to explain the fast  $T_1$  relaxation in comparison to mono-nuclear copper centers [Pfenninger et al. 1995].

Figure 6.2 shows the data from the RT experiments. The  $T_1$  values were read off from the plot where the signal intensity is 0.6 times the signal intensity under non-saturating conditions. The echo signal could not be fully saturated due to relaxation processes other than  $T_1$  relaxation (e.g. spectral diffusion). This is particularly evident at short repetition times (figure 6.2). Another reason that the echo intensity did not go to zero for infinitely small repetition time was that for every measurement 200 signals were summed: the first signals were not saturated yet, but did contribute to the RT signal, producing RT signals that were slightly too large. Assuming (falsely) that only the first detected signal is unsaturated and has an intensity equal to 1, and all other signals are saturated and have intensity 0, the detected relative signal intensity over 200 averages is 0.05. In practice, it takes several shots to saturate the signal fully so that the detected signal intensity is probably at least 0.1. No attempt was made to subtract this contribution. For these reasons, short  $T_1$  relaxation times ( $< 10 \mu\text{s}$ ) were preferably measured by IR.

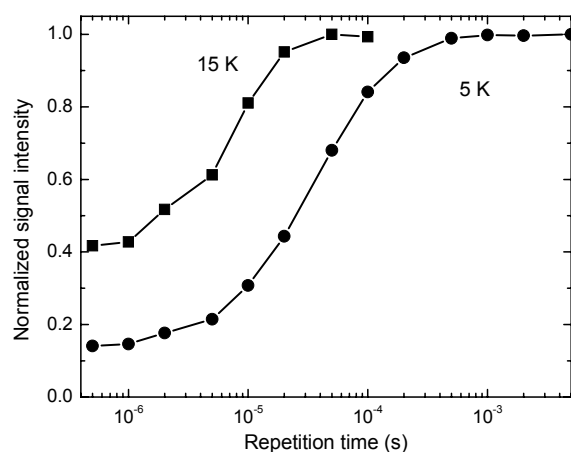


Figure 6.2. RT experiment traces of 0.2 mM  $\text{Cu}_A$  at G-band. The measurements were performed at  $g_{yy}$  of  $\text{Cu}_A$ . The  $T_1$  values were read off where the signal was 0.6 times the signal under non-saturating conditions. The lines serve to guide the eye. The results were the average of 25 data points, where each point was the sum of 200 sequential measurements with a certain repetition time. The traces do not go to zero because of experimental limitations (see text).

The  $T_1$  values measured at G-band frequency are shown in figure 6.3. The values obtained by IR measurements are in good agreement with those obtained by RT experiments. Increasing the concentration from 0.2 mM to 1 mM protein enhanced the signal-to-noise ratio, but did not affect  $T_1$  relaxation.

Also shown in figure 6.3 are  $T_1$  values determined for  $\text{Cu}_A$  in bovine CcO at X-band [Scholes et al. 1984]. At low temperature  $T_1$  at G-band is significantly shorter than at X-band, but at high temperature ( $T > 25 \text{ K}$ ) the  $T_1$  at both frequencies become equal. The X-band data had been simulated by assuming two dominating  $T_1$  relaxation processes: direct process and Raman process. The G-band data were simulated with the same

relaxation processes and the same Raman coefficients, but with a 1600 times larger contribution from the direct process (shown by the dashed line in figure 6.3). The simulation parameters are given in the figure caption.

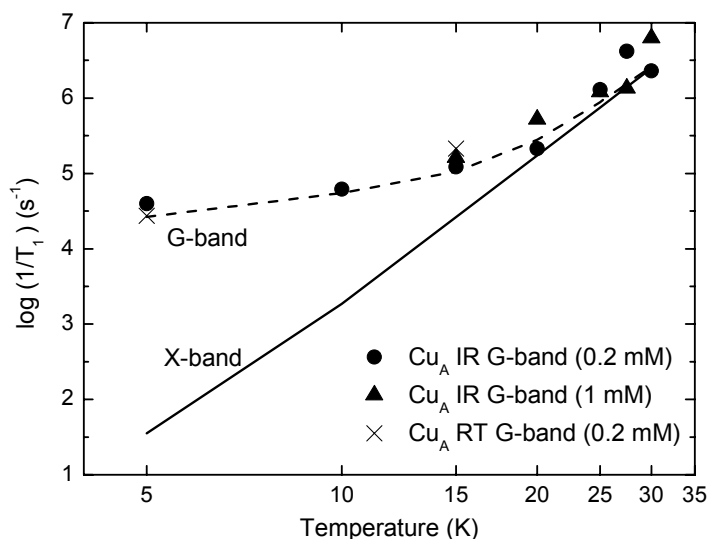


Figure 6.3.  $T_1$  relaxation of  $\text{Cu}_A$  in  $\text{CcO}_{II}$  measured at G-band by IR and RT measurements, and at X-band by saturation recovery measurements [Scholes et al. 1984]. The  $\text{CcO}_{II}$  protein concentration at G-band is given in the plot, X-band measurements were performed on  $\text{Cu}_A$  in  $\text{CcO}$ . The X-band curve is given by:  $1/T_1 = 4.9 \cdot 10^{-4} T^{6.57} + 3.3T$ , the G-band simulation is given by:  $1/T_1 = 4.9 \cdot 10^{-4} T^{6.57} + 5280T$ .

### 6.1.2. $\text{Cu}^{2+}$ in $\text{Cu}^{2+}$ -octoethylporphyrin-TPA

The  $T_1$  relaxation of  $\text{Cu}^{2+}$  in  $\text{Cu}^{2+}$ -NO $\cdot$  dissolved in ortho-terphenyl (otp), between 5 and 100 K was studied at G-band by IR experiments. Some of the IR traces are shown in figure 6.4. The IR traces were fitted with single exponential functions, as shown in the plot, and the resulting  $T_1$  values are plotted in figure 6.5. The single exponential fits do not simulate the data well at first few points, which is due to fast decay caused by spectral diffusion, as discussed above. The  $T_1$  values obtained from fits to the dipolar relaxation data of  $\text{Cu}^{2+}$ -NO $\cdot$  agree very well with the  $T_1$  values determined by IR measurements. This means that the determined  $T_1$  values were not influenced by spectral diffusion, because spectral diffusion does not play a part in dipolar relaxation. The  $T_1$  relaxation rates of  $\text{Cu}^{2+}$  were fitted with a linear temperature dependence, indicative of a direct process that dominates the longitudinal relaxation of  $\text{Cu}^{2+}$ .  $T_1$  values determined at X-band for different  $\text{Cu}^{2+}$  complexes, such as the simulated trace shown in figure 6.5 (sample 1 from [Fielding et al. 2006]), are longer than at G-band when  $T < 90$  K.

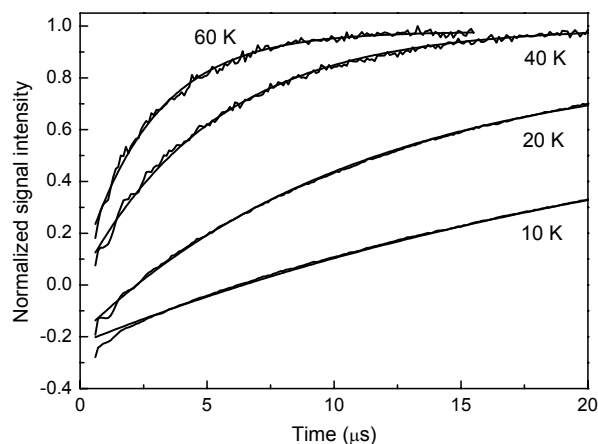
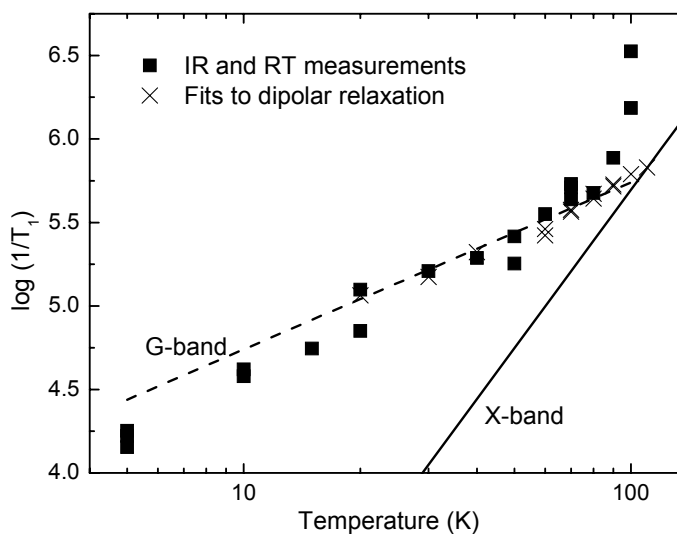


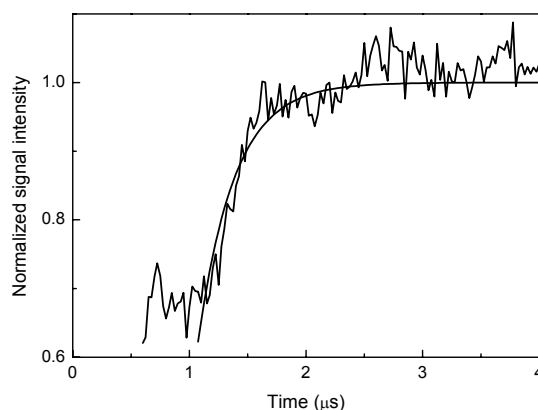
Figure 6.4. IR traces of  $\text{Cu}^{2+}$  in  $\text{Cu}^{2+}\text{-NO}\cdot$  at various temperatures as indicated in the plot. The measurements were performed at the signal maximum ( $g_{\perp}$ ,  $B_0 = 6.282 \text{ T}$ ). Single exponential fits are shown as noiseless lines.

Figure 6.5.  $T_1$  relaxation times of  $\text{Cu}^{2+}$  in  $\text{Cu}^{2+}\text{-NO}\cdot$ , dissolved in ortho-terphenyl, measured at G-band frequency. Measurements were performed at the  $\text{Cu}^{2+}$  signal maximum ( $g_{\perp}$ ). The simulated G-band curve is given by  $1/T_1 = 5500 \cdot T$ , the simulated X-band curve is given by  $1/T_1 = 0.249 \cdot T^{3.15}$  (fit to sample 1 [Fielding et al. 2006]).



The  $T_1$  values determined at 100 K in two separate IR experiments are in strong disagreement with the values obtained from fits to the dipolar relaxation experiments. An IR trace of  $\text{Cu}^{2+}$  measured at 100 K is given in figure 6.6, together with a single exponential fit. From figure 6.6 it becomes clear that the current G-band spectrometer setup is not well suited to measure  $T_1$  relaxation times smaller than  $1 \mu\text{s}$ : due to the presence of an unwanted echo, the dead time of the experiment was at least 600 ns (see appendix B). The unwanted echo was not completely avoided, and it created an artifact in the IR trace during the first  $\mu\text{s}$  of the experiment. Moreover, the signal-to-noise ratio at this temperature was not very high due to fast  $T_2$  relaxation of  $\text{Cu}^{2+}$ . For these reasons, the  $T_1$  values determined from dipolar relaxation measurements were assumed to be more reliable.

Figure 6.6. IR trace of  $\text{Cu}^{2+}$  in  $\text{Cu}^{2+}\text{-NO}\cdot$ , dissolved in otp, at 100 K with corresponding single exponential fit. The fit is given by:  $0.08 + 1.6 \cdot \exp(-T/311 \cdot 10^{-9})$ . This fit was considered unreliable due to large dead time, interference of the unwanted echo up to at least  $1 \mu\text{s}$ , and the large step width (5 ns) of the experiment (see text).



### 6.1.3. Heme Iron in Cytochrome c and in CcO

The spectrum of low-spin heme iron is much too broad at G-band (approximately 6 T) to allow direct measurement of the  $T_1$  relaxation by high-field EPR. At temperatures as low as 5 K, the signal intensity from either heme a in CcO or from cytochrome c was too small to be observed at G-band frequency, although the cytochrome heme signal overlapped with the  $Cu_A$  signal at X-band frequency up to 12 K [Lyubenova et al.]. Using dipolar relaxation measurements, the  $T_1$  relaxation of such broad and fast-relaxing species can be investigated.

From our dipolar relaxation studies of CcO (described in chapter 4), we obtained  $T_1$  values of heme a. Similarly, from dipolar relaxation measurements of CcO<sub>II</sub> with cytochrome c we deduced  $T_1$  relaxation times of the heme in cytochrome c. These  $T_1$  values have been plotted in figure 6.7, along with the simulated curves for heme a and cytochrome c heme at X-band (from [Scholes et al. 1984]).

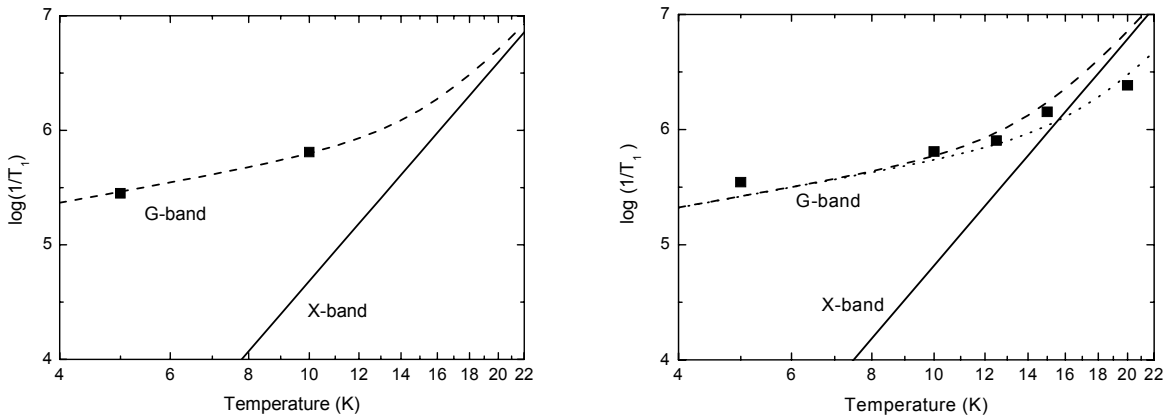


Figure 6.7.  $T_1$  values for cytochrome  $c_{hh}$  heme (left) and heme a in CcO (right). G-band values were obtained from fits to dipolar relaxation data, X-band values by saturation recovery measurements on horse cytochrome c and bovine CcO [Scholes et al. 1984]. The X-band data are given by  $1/T_1 = 2.21 \cdot 10^{-2} \cdot T^{6.34} + 4.85 \cdot T$  (cytochrome c) and  $1/T_1 = 1.9 \cdot 10^{-2} \cdot T^{6.54} + 2.1 \cdot T$  (heme a). The G-band simulations (dashed) are given by:  $1/T_1 = 2.21 \cdot 10^{-2} \cdot T^{6.34} + 58200 \cdot T$ ,  $1/T_1 = 1.9 \cdot 10^{-2} \cdot T^{6.54} + 52500 \cdot T$  (dash) and  $1/T_1 = 0.6 \cdot 10^{-2} \cdot T^{6.54} + 52500 \cdot T$  (dotted line) for cytochrome c and heme a, respectively.

$T_1$  relaxation times were determined for only two points in the cytochrome c – CcO<sub>II</sub> pair. Dipolar relaxation was studied up to 20 K, but above 10 K the relaxation rate of cytochrome heme was so high that the low-temperature approximation  $T_2^{\text{dip}} = T_{1f}$  was no longer valid. At high temperature the  $T_1$  of the cytochrome heme could not be determined, because the exact structural parameters are unknown. The two points lie well above the values determined for  $T_1$  at X-band, and they fit a line of which the slope is  $T^1$ . For the simulation in figure 6.7 it was assumed that at approximately 20 K a Raman process dominates the  $T_1$  relaxation, which makes the  $T_1$  at X-band and G-band equal at that temperature. This assumption could not be proved or disproved by our measurements.

As mentioned in chapter 4, the  $T_1$  relaxation of heme a had an interesting dependence on temperature, shown in figure 6.7. Up to 15 K, the  $T_1$  values could be fitted well by assuming the same type of behavior as cytochrome c: a strongly enhanced direct process at low temperature. However, the  $T_1$  value determined at 20 K is a factor of 3 larger than the value simulated at 20 K when assuming a Raman process with the same coefficients as those determined at X-band frequency. The data point at 20 K is reliable, because the signal-to-noise ratio at this temperature was high (see figure 4.5 and 4.6), and the difference in transverse relaxation between  $\text{Cu}_A$  in  $\text{CcO}_{\text{II}}$  and  $\text{Cu}_A$  in  $\text{CcO}$  was large. There are two ways to interpret the heme a data. First, the  $T_1$  values determined by dipolar relaxation enhancement may be influenced by the near presence of heme  $a_3$ : it is only 23 Å away from  $\text{Cu}_A$ , and may also cause dipolar relaxation enhancement. This would mean that all determined  $T_1$  values of heme a are unreliable, because it is unknown what the exact influence of heme  $a_3$  is. Another reason that the  $T_1$  relaxation times may be unreliable is that it is not clear if the intrinsic relaxation of  $\text{Cu}_A$  is the same in  $\text{CcO}_{\text{II}}$  as in  $\text{CcO}$ . Because the signal of  $\text{Cu}_A$  in  $\text{CcO}$  was divided by the signal of  $\text{Cu}_A$  in  $\text{CcO}_{\text{II}}$  to eliminate intrinsic  $\text{Cu}_A$  relaxation, as explained in chapter 2, a systematic error was introduced if the intrinsic transverse relaxation of  $\text{Cu}_A$  in  $\text{CcO}$  is not the same as the intrinsic relaxation of  $\text{Cu}_A$  in  $\text{CcO}_{\text{II}}$ . Nevertheless, the two orders of magnitude difference at 5 K between heme a relaxation at X-band and at G-band frequency is realistic, not in the last place because an almost equal effect was observed for the structurally similar cytochrome c heme.

Another possible explanation is that the fast  $T_1$  relaxation of heme  $a_3$  may have influenced the  $T_1$  behavior of heme a. The effect of dipolar relaxation enhancement on  $T_1$  of the coupled spin is maximum where  $1/T_{1f} = \omega_L$  ( $\omega_L$  is the Larmor frequency of the observer spin), and because  $\omega_L$  is a factor of 20 larger at G-band than at X-band, a different temperature dependence of  $T_1$  relaxation would occur at the different microwave frequencies.

The G-band data cannot be simulated assuming only the direct process, but changing the Raman coefficient  $A$  from  $1.9 \cdot 10^{-2}$  (which was found for X-band data) to  $0.6 \cdot 10^{-2}$  increased the fit quality significantly, as shown in figure 6.7 (left).



## 6.2. Discussion

### 6.2.1. Frequency Dependence of $T_1$ Relaxation

The dominating  $T_1$  relaxation processes at low temperature for paramagnetic centers with no low-lying excited states are the direct process and the Raman process (see chapter 2). The direct process is characterized by a linear dependence of  $1/T_1$  on temperature, whereas in the Raman process  $1/T_1$  depends on a high power of the temperature ( $T^5 - T^9$ ). The direct process depends on magnetic field as  $1/T_1 \sim B_0^4$ ; the common Raman process is independent of magnetic field [Orbach 1961].

Low-spin heme in cytochrome *c* does not have low-lying excited electronic states [Stapleton et al. 1980], and the temperature dependence of  $T_1$  relaxation of both  $\text{Cu}_A$  [Scholes et al. 1984] and different  $\text{Cu}^{2+}$  complexes [Fielding et al. 2006] could be well described without taking into account the possible presence of low-lying excited states. In the following discussion, only the Raman and direct processes were assumed to play a role in  $T_1$  relaxation.

In a study on dilute  $\text{Fe}^{3+}$  in a  $\text{K}_3\text{Co}(\text{CN})_6$  crystal lattice, performed in the 1960s, a  $B_0^4$  dependence of  $T_1$  relaxation rate was observed [Davids et al. 1964]. Eaton and coworkers found a dependence of  $T_1$  on the magnetic field for  $\text{VO}^{2+}$  ions [Eaton et al. 2001], but because this dependence was much smaller than a power of four (power of  $< 2$ ), they mused that there might be no field dependence at all, and that the difference in relaxation times was caused by high local concentrations of spins in the crystal at high field (W-band in their case). They do not explain why this faster relaxation was not observed at X-band.

In this work, we provide evidence that there is a dependence of the direct process on the magnetic field, albeit not a  $B_0^4$  power. That our observations were not caused by increased spectral diffusion was proven by the fact that the values we measured for  $\text{Cu}^{2+}\text{-NO}\cdot$  using IR experiments were backed by the values obtained by fitting  $T_1$  relaxation times to dipolar relaxation traces.

We found that the direct process in  $\text{Cu}_A$  at G-band was increased a factor of 1600 with respect to X-band, in  $\text{Cu}^{2+}$  it was increased  $\sim 2000$  times. Because the relaxation behavior of  $\text{Cu}^{2+}\text{-NO}\cdot$  was not measured at X-band, no  $T_1$  data was known, and the comparison is based on  $\text{Cu}^{2+}$  ions in similar environments [Fielding et al. 2006]. Those X-band measurements were not performed at temperatures below 9 K, so that the contribution of the direct process to the  $T_1$  relaxation could not be determined very accurately. For low-spin heme iron, the direct process increased a factor of 12000 (cytochrome *c*) and 25000 (heme *a*) relative to X-band data. However, also in this case the contribution of the direct process could not be determined accurately because the measurements were not performed at temperatures lower than 1.5 K [Scholes et al. 1984].

We find factors that lie close to  $B_0^2$  (400) and  $B_0^3$  (8000), but that are certainly not  $B_0^4$  (160 000). It is unclear how this discrepancy could be explained.

### 6.2.2. Conclusions

We have provided strong evidence for the fact that the efficiency of the direct effect, causing  $T_1$  relaxation of spins at low temperature, is strongly dependent on the magnetic field. This direct effect increased a factor of  $10^3$  from X-band (0.3 T) to G-band (6.4 T) frequency for two paramagnetic centers involving Cu ions, and even a factor of  $10^4$  for low-spin hemes. This is not a  $B_0^4$  dependency, as predicted in literature [Orbach 1961], but much smaller.

Our findings of increased  $T_1$  relaxation rates at high magnetic fields have many implications for high-field EPR. A positive consequence is that the repetition time of a low-temperature, echo-detected experiment may be decreased substantially at higher magnetic field, without causing saturation of the sample. Measuring time may therefore be strongly reduced. Obviously, when studies involving  $T_1$  relaxation times are performed, such as dipolar relaxation measurements, one should be aware of changed  $T_1$  values.

Dipolar relaxation measurements were found to be very useful in the study of  $T_1$  relaxation of paramagnetic species with broad EPR spectra or with short relaxation times. The longitudinal relaxation of heme  $\text{Fe}^{3+}$  became accessible at high magnetic fields, and the relaxation of  $\text{Cu}^{2+}$  at high temperatures where IR measurements were unreliable, could be accurately determined.



## Chapter 7. Concluding Remarks

Cytochrome *c* oxidase and its electron-transfer partner, cytochrome *c*, do not form a specific electron-transfer complex, but move along each other's binding surfaces and transfer an electron as soon as the distance between donor and acceptor is suitably small. This binding model is applicable to electron-transfer proteins in general.

A suitable model system for studying orientation-dependent dipolar relaxation enhancement needs to possess the following characteristics:

- It should be possible to measure the slow-relaxing spin, A, in presence and in absence of its fast-relaxing partner, B.
- The B spin should have a  $T_1$  relaxation rate larger than the dipolar splitting (in  $\text{rad s}^{-1}$ ) within the accessible temperature range.
- The A spin should have a  $T_2$  relaxation time that is significantly longer than the dipolar relaxation time.
- The distance between the two coupled spins, as well as their mutual orientation, and the orientation of the dipolar vector with respect to the spins should be fixed and known. In the presence of exchange coupling, this value should also be known.
- The coupled spins should be present in a ratio of 1:1, or else the ratio should be well known.
- The *g*-tensor anisotropy of the A spin should be large enough to obtain good spectral resolution at high fields, but small enough to be measurable.

Accurate dipolar relaxation measurements are useful for measuring distances by EPR if the requirements, as described above, are fulfilled. Qualitative studies of the relaxation enhancement that occurs when adding a fast-relaxing paramagnetic species (proteins or other molecules) are more widely applicable. For instance, to determine if complex formation takes place between two proteins. Or to detect where a radical is situated on a protein by studying how it reacts to addition of paramagnetic agents to the solution [Likhtenshtein 2000].

$T_1$  relaxation that is caused by the direct effect is strongly enhanced at higher magnetic fields.

Dipolar relaxation enhancement is useful to measure relaxation times that would otherwise not be accessible, e.g. due to large spectral width or fast  $T_2$  relaxation of the spin under study.



# Appendix A - Programs for Dipolar Relaxation Calculations

## A.1. HEdipolar

```
% new version TP 21.12.2005

% fit or simulation of Hahn Echo decay function
% by dipolar coupling of 2 molecules I (observer spin slow relaxing) and S (relaxer spin, fast
relaxing)
% relaxation formula of Kev Salikov used for HE decay (two jump model)
% powder sample with orientation selection by hyperfine and g distribution compared to
inhomogeneous lw or Bl
% optimized for heme of Cyt c and CuA of Cox
% geff of cyt is explicitly calculated (no perturbation solution)
% full dipolar interaction considered A C D
% explicit formula for dipolar splitting
% R distribution

% experimental files: vectors with signal intensity (signalexp)

% all experimental, spin system and program routing parameters are defined in parameters
% all simplex variables are defined in simplexparameters

% load general constants
Constants;

% load parameters for the simulation
parameters;

% from parameters define other values
calculatedvalues;

% calculate CuA spectra for the chosen parameters and choose B0 or load orientation selection
calculatespectra;

% simplex parameters for fit procedure or simulation
simplexparameters;

% calculate the echo decay for the given parameters
echodecay;
```

### A.1.1. Constants

```
betae=1.39961e6;           % electronic beta factor Hz/G
gammae=2.8e6;             % electronic gamma factor for free electron spin
kboltz=1.3805e-23;        % Boltzmann constant in J/K
hplanck=6.6256e-34;      % Planck constant in J s
giso=2.0023;              % free electron g-value
Dipconst=1.298e7;         % constant for dipolar splitting
gr=pi/180;                % conversion factor from degree to radians
```

### A.1.2. Parameters

```
% program parameters

SimFitauswahl='S';        % simulation (S) or fit (F)
Orientationauswahl='F';   % Calculate (C) orientation selection or load file (F)
Bauswahl='G';             % selection of field position graphical (G) or numerical (N)

loadfilename='GbandX30';  % filename for loading of stored orientation selection

Nkugel=50;                % Parameter for the resolution on orientational sphere

% experimental parameters

vMW=180e9;                % microwave frequency
```

```

taustart=200e-9;           % start value of tau (corrected for pulse lengths !)
taustep=10e-9;           % step width of tau
tausize=200;             % number of tau steps

Bstart=58000;           % start value of B
Bstep=60;               % step value of B
Bsize=128;              % length of B vector

%B0=64000;              % B0 resonance position for numerical input

T=[20];                 % temperatures in K

    % parameters for spin system

    % observer spin I : CuA of Cytochrome c Oxidase

gI=[2.000 2.0300 2.1800]; % main g value of I spin CuA
mI=3;                   % nuclear spin quantum number for multiplicity
intmI=[1 2 3 4 3 2 1]; % hyperfine intensities of binuclear Cu
AI=[23 25 38];          % hyperfine tensor of CuA spin
lw=200;                 % gaussian inhomogeneous lw of I spin system

    % relaxer spin S : cytochrome c heme

S=1/2;                  % spin quantum number
%gS=[1.49 2.24 3.00];   % g-values of heme a
gS=[1.25 2.26 3.06];    % g-values of Hh cyt
%gS=[1.1 2.1 3.3];      % g-values of c552
gangles=[0 0 0]*gr;     % orientation of g-tensor of S with respect to I in rad

    % dipolare coupling S-I

R=2 ;                   % distance in nm

thetaD=0*gr;            % Polar angles of D with respect to G(I)
phiD=0*gr;

Tlfactor=[1];           % correction factor of T1

offset=0;                % offset of unbound CuA
J= 5e6;                  % exchange interaction in Hz

```

### A.1.3. Calculated values

```

    % program parameters

maindirectory=cd;       % name of the main program directory

    % experimental values

tau=taustart:taustep:taustart+(tausize-1)*taustep; % tauvector
B=Bstart:Bstep:Bstart+(Bsize-1)*Bstep;           % B vector for spectra

spectrum=zeros(1,Bsize); % initialize spectra arrays

GS=diag(gS); % g-Tensor of FeS in its main axis system
GI=diag(gI); % g-Tensor of CuA in its main axis system

    % Relaxation times by formula from Scholes et al. Biophys. J 45, 1027 (84)

    % Cyt c relaxation times
A2=2.21e-2;
n2=6.34;
B2=48500;
TlS=1./(A2*T.^n2+B2*T);

    % parameter for inhomogeneous distribution

gaussrange=2; % +- times lw-parameter
gausspoints=10; % number of pts for gaussian distr. is 2*gausspoints+1

gaussvector=-gaussrange:gaussrange/gausspoints:gaussrange;

```

```

gaussint=exp(-gaussvector.^2);
gaussint=gaussint/sum(gaussint);           % normalized intensities for gaussian
                                           inhomogeneous distribution

geffI=vMW/(B0*betae);                     % effective resonance g (with hfi) for I spin

```

#### A.1.4. Calculatespectra

```

% calculate the CuA spectra and select B0 from display
% or load a saved orientation selection file
% decided by variable Orientationauswahl defined in parameters.m

if Orientationauswahl=='C',                % calculate the orientation selection

    [theta phi]=KUGEL(Nkugel);             % Polar angles for molecules on sphere
    Norientations=length(theta);          % Number of molecules on sphere

    % calculate geff, Aeff for CuA
    % perturbation solution on projection to the field

    geff=(sin(theta).*cos(phi)).^2*gI(1)+(sin(theta).*sin(phi)).^2*gI(2)+cos(theta).^2*gI(3);
    Aeff=(sin(theta).*cos(phi)).^2*AI(1)+(sin(theta).*sin(phi)).^2*AI(2)+cos(theta).^2*AI(3);
    Bz=vMW./(geff*betae);                 % Zeeman resonance fields

    % loop for nuclear spin MI

    for k1=1:length(intmI),
        MI=-mI+(k1-1);
        Bhfi=Aeff*MI/2;                    % hyperfine field
        BeffmI(k1,:)=Bz+Bhfi;              % hyperfine resonance field
        spectrumI=hist(BeffmI(k1,:),B)*intmI(k1); % hyperfine histogram
        spectrum=spectrum+spectrumI;       % add hyperfine spectra for total spectra
    end

    % inhomogeneous lw convolution done in fourier space

    Bhom=B-mean(B);
    linie=exp(-(Bhom/lw).^2);
    inhomlinie=linie/sum(linie);
    finhom=fft(inhomlinie);

    fspectrum=fft(spectrum).*finhom;
    spectrum=real(fftshift(iffshift(fspectrum)));
    plot(B,spectrum);
    if Bauswahl=='G',
        title('choose detection position with cursor');
        [B0 dummy]=ginput;                 % choose the observer position
        close;
    end;

    phiselect=[];
    thetaselect=[];
    intselect=[];                           % intensities of selected orientations

    k3=1;                                    % counter for selected orientations
    for k2=1:length(theta),
        index=find(abs(BeffmI(:,k2)-B0)<lw); % find for all hf lines inside lw box
                                                around resonance field position

        if isempty(index)==0,
            phiselect(k3)=phi(k2);          % lines found
            thetaselect(k3)=theta(k2);      % take orientations
            intselect(k3)=sum(intmI(index)); % take intensity from hf lines inside box
            k3=k3+1;
        end
    end

    % save the selected orientations

    wahl=input('save orientations ?');

    if wahl=='Y',
        filename=input('filename');

```



```

        eval(['save ',maindirectory,'\orientationselectfiles\',filename, '.ang B0 phiselect
thetaselect intselect;' ]);
    end

elseif Orientationauswahl=='F',
    % load orientation selection from file specified
    % in parameters.m

    eval(['load ',maindirectory,'\orientationselectfiles\',loadfilename, '.ang -MAT;']);

end

```

#### A.1.4.1. Kugel

```

% Kugelprogram by Jens Törring

function [theta, phi]=kugel(n)

np = ceil( n * sin( ( 0.5 : n - 0.5 ) * pi / ( 2 * n ) ) );
nF = sum( np );

theta_j = 0;
count = 1;
for j = 1 : n,
    dtheta = acos( cos( theta_j ) - np( j ) / nF ) - theta_j;
    theta( count : count + 4*np( j ) - 1 ) = theta_j + dtheta / 2;
    dphi = pi / ( 2 * np( j ) );
    phi( count : count + 4*np( j ) - 1 ) = 0.5 * dphi : dphi : ( 4*np( j ) - 0.5 ) * dphi;
    count = count + 4*np( j );
    theta_j = theta_j + dtheta;
end;

```

#### A.1.5. Simplexparameters

```

simplexruns=10;
fitoptions=optimset('Display','final','MaxIter',400);
%fitvalues

fitstartvalues= [gangles thetaD phiD offset R J];
vub= [pi/2 pi/2 pi/2 pi/2 pi/2 0.2 4 1e7];
vlb= [0 0 0 0 0 1.5 -1e7];

lsize=10;
lstep=pi/lsize;

wsize=length(thetaselect);

for k=1:lsize;

    theta((k-1)*wsize+1:k*wsize)=thetaselect';
    phi((k-1)*wsize+1:k*wsize)=phiselect';
    l((k-1)*wsize+1:k*wsize)=k*lstep*ones(wsize,1);
    int((k-1)*wsize+1:k*wsize)=intselect';
end

fitvalues=fitstartvalues;

durchlauf=1;
bestsigma=1e20*ones(10,1);
bestfitvalue=zeros(10,length(fitstartvalues));

```

#### A.1.6. Echodecay

```

if SimFitauswahl=='S',
    signalfit=simdecay(fitvalues,tau,T1S,geffI,GS,theta,phi,l,int,betae,Dipconst,B0);

```

```

if exist('signalexp')==0, % plot w or w/o experimental file
else
    semilogy(2*tau,signalexp,'b',2*tau,signalfit,'r')
end
elseif SimFitauswahl=='F', % fit of decay
    % initialize other variables
    tau=tau;
    T1S=T1S;
    geffI=geffI;
    GS=GS;
    theta=theta;
    phi=phi;
    l=l;
    int=int;
    betae=betae;
    Dipconst=Dipconst;
    B0=B0;
    signalexp=signalexp;

    fitfunct=@(x) fitdecay(x,tau,T1S,geffI,GS,theta,phi,l,int,betae,Dipconst,B0,signalexp);
    for k3=1:simplexruns, % loop of new simplex runs with random starting values
        % simplex fitroutine with fitfunction fitsignal
        [x
sigma]=fmincon(fitfunct,fitvalues,diag(ones(1,length(fitvalues))),vub,[],[],vub,vub,[],
fitoptions);

        % renormalize fitvalues
        fitvalues=x;

        'durchlauf nr:',durchlauf,

        % save 10 best results

        if sigma<bestsigma(10),
            number=min(find(bestsigma>sigma));
            bestsigma(number+1:10)=bestsigma(number:9,:);
            bestsigma(number)=sigma;
            bestfitvalue(number+1:10,:)=bestfitvalue(number:9,:);
            bestfitvalue(number,:)=fitvalues;
            save temp ;
            bestsigma,
            bestfitvalue,
        end

        xstart=rand(size(fitvalues)); % random starting conditions for fitvariables
        fitvalues=xstart.*(vub-vlb)+vlb;
        durchlauf=durchlauf+1; % next fit procedure
    end
end
end

```

### A.1.6. Simdecay

```

% including calculation with a distribution in R values with amplitudes
function f=simdecay(fitvalues,tau,T1S,geffI,GS,theta,phi,l,int,betae,Dipconst,B0)

    % calculate dipolar coupling (A & B term) and echo decay function (Kev Salikov formula)

    gangles=fitvalues(1:3);
    thetaD=fitvalues(4);
    phiD=fitvalues(5);
    offset=fitvalues(6);
    R=fitvalues(7);
    J=fitvalues(8);
    T1factor=fitvalues(9:end);

```

```

Tsize=length(T1S);

    % parameters for the Kev Formula
tc=T1S./T1factor;          % correlation time
km=1./tc;                 % corresponding rate
signal=zeros(Tsize,length(tau));

GSM=Tensrot(gangles,GS);  % rotate G-Tensor of S into I-spin axis system

DM=Dipolmol(thetaD, phiD); % calculate dipolar tensor in I spin axis system

for k=1:length(l),

    GSL=Tensrot([l(k),theta(k),phi(k)],GSM); % rotate GS in Lab system
    geffS(k)=sqrt(GSL(1,3)^2+GSL(2,3)^2+GSL(3,3)^2);
    wxz=GSL(1,3)*betae*B0;
    wyz=GSL(2,3)*betae*B0;
    wzz=GSL(3,3)*betae*B0;

    DL=Tensrot([l(k),theta(k),phi(k)],DM); % rotate D tensor in Lab system
    Dxz=DL(1,3)*geffS(k)*geffI*Dipconst;
    Dyz=DL(2,3)*geffS(k)*geffI*Dipconst;
    Dzz=DL(3,3)*geffS(k)*geffI*Dipconst;

    dxz=Dxz/R^3;
    dyz=Dyz/R^3;
    dzz=Dzz/R^3;

    Dm=((wzz+dzz/2+J)^2 +(wxz+dxz/2)^2 +(wyz+dyz/2)^2)^(1/2) - ((wzz-dzz/2-J)^2 +(wxz-dxz/2)^2
+(wyz-dyz/2)^2)^(1/2);
    Dm=Dm*pi; % half splitting in rad s-1
    test(k)=Dm;
    intm=int(k);

    for k2=1:Tsize,
        rmT=sqrt(km(k2)^2-Dm^2);
        kmT=km(k2);

        % Kev Salikov Formula
        signal(k2,:)=signal(k2,:)+(1/rmT^2*(kmT/2*((kmT+rmT)*exp(-2*(kmT-rmT)*tau)+(kmT-
rmT)*exp(-2*(kmT+rmT)*tau))-Dm^2*exp(-2*kmT*tau))*intm);
    end

end

signal=signal/sum(intm);

signal=(signal+offset)/(1+offset); % add offset and renormalize

for k2=1:Tsize,
    signal(k2,:)=signal(k2,:)/signal(k2,1); % normalize signal
end

f=signal;

```

### A.1.6.1. Tensrot

```

% new function for rotation of matrices with 3 euler angles

function T= Tensrot(euler,T),

c=euler(1);
b=euler(2);
a=euler(3);

D =[cos(c)*cos(b)*cos(a)-sin(c)*sin(a), -cos(c)*cos(b)*sin(a)-sin(c)*cos(a), cos(c)*sin(b);...
    sin(c)*cos(b)*cos(a)+cos(c)*sin(a), -sin(c)*cos(b)*sin(a)+cos(c)*cos(a), sin(c)*sin(b);...
    -sin(b)*cos(a), sin(b)*sin(a), cos(b)];

T=D*T*inv(D);

```

### A.1.6.2. Dipolmol

```
% new function for rotation of matrices with 3 euler angles

function T= Dipolmol(tD,pD),

T = [3*cos(pD)^2*cos(tD)^2+1-3*cos(pD)^2, 3*cos(pD)*(-1+cos(tD)^2)*sin(pD), -
3*sin(tD)*cos(pD)*cos(tD); ...
     3*cos(pD)*(-1+cos(tD)^2)*sin(pD), -2+3*cos(tD)^2+3*cos(pD)^2-3*cos(pD)^2*cos(tD)^2, -
3*sin(tD)*sin(pD)*cos(tD); ...
     -3*sin(tD)*cos(pD)*cos(tD), -3*sin(tD)*sin(pD)*cos(tD),-3*cos(tD)^2+1];
```

## A.2. HEdipolar2D

```
% new version TP 06.01.2006 2D

% fit or simulation of Hahn Echo decay function
% by dipolar coupling of 2 molecules I (observer spin slow relaxing) and S (relaxer spin, fast
relaxing)
% relaxation formula of Kev Salikov used for HE decay (two jump model)
% powder sample with orientation selection by hyperfine and g distribution compared to
inhomogeneous lw or B1
% optimized for heme of Cyt c and CuA of Cox
% geff of cyt is explicitly calculated (no perturbation solution)
% full dipolar interaction considered A C D
% explicit formula for dipolar splitting
% new minimization algorithm SQP

% experimental files: vectors with signal intensity (signalexp)

% all experimental, spin system and program routing parameters are defined in parameters2D
% all simplex variables are defined in simplexparameters2D

% load general constants
Constants;

% load parameters for the simulation
parameters2D;

% from parameters define other values
calculatedvalues;

% calculate CuA spectra for the chosen parameters and choose B0 or load orientation selection
calculatespectra2D;

% simplex parameters for fit procedure or simulation
simplexparameters2D;

% calculate the echodecay for the given parameters
echodecay2D;
```

### A.2.1. Parameters2D

```
% program parameters

SimFitauswahl='S'; % simulation (S) or fit (F)

Nkugel=35; % Parameter for the resolution on orientational sphere

% experimental parameters

vMW=180e9; % microwave frequency

taustart=200e-9; % start value of tau (corrected for pulse lengths !)
taustep=10e-9; % step width of tau
tausize=200; % number of tau steps

Bstart=58000; % start value of B
Bstep=60; % step value of B
Bsize=128; % length of B vector (best choose power of 2 for FFT !)

B0=63620;

T=[20]; % temperature in K

% parameters for spin system

% observer spin I: CuA of Cytochrome c Oxidase

gI=[2.000 2.0300 2.1800]; % g-value of I spin CuA
mI=3; % nuclear spin quantum number for multiplicity
intmI=[1 2 3 4 3 2 1]; % hyperfine intensities of binuclear Cu
AI=[23 25 38]; % hyperfine tensor of CuA spin
lw=200; % gaussian inhomogeneous lw of I spin system
```

```

lw=200;

relaxer spin S : cytochrome c heme

S=1/2; % spin quantum number
gS=[1.15 2.26 3.06]; % main g values of S
gangles=[0 0 0]*gr; % orientation of g-tensor of S with respect to I in rad

% dipolare coupling S-I

R=2 ; % distance in nm
phiD= 0*gr; % Polarangles (phi(D),theta(D) of D with respect to G(I)
thetaD=0*gr;

Tlfactor=[1]; % correction factor of T1

offset=0.0; % offset of unbound CuA
J=10e6; % exchange interaction in s-1

```

### A.2.2. Calculatespectra2D

```

[theta phi]=KUGEL(Nkugel); % Polar angles for molecules on sphere
Norientations=length(theta); % Number of molecules on sphere

% calculate geff, Aeff and lweff for CuA

geff=(sin(theta).*cos(phi)).^2*gI(1)+(sin(theta).*sin(phi)).^2*gI(2)+cos(theta).^2*gI(3);
Aeff=(sin(theta).*cos(phi)).^2*AI(1)+(sin(theta).*sin(phi)).^2*AI(2)+cos(theta).^2*AI(3);
Bz=vMW./(geff*betae); % Zeeman resonance fields

% initialize
phiselct=[];
thetaselct=[];
intselct=[]; % intensities
Beff=[];
kanal=[]; % spectral position
GeffI=[];

% loop for nuclear spin MI
for k1=1:length(intmI),
    MI=-mI+(k1-1);
    Bhfi=Aeff*MI/2; % hyperfine field
    BeffmI(k1,:)=Bz+Bhfi; % hyperfine resonance field
    spectrumI=hist(BeffmI(k1,:),B)*intmI(k1); % hyperfine histogram
    kanalI=round((BeffmI(k1,:)-Bstart)/Bstep);
    kanal=[kanal,kanalI];
    phiselct=[phiselct,phi];
    thetaselct=[thetaselct,theta];
    GeffI=[GeffI,geff];
    intselct=[intselct,intmI(k1)*ones(1,length(theta))];
    Beff=[Beff,BeffmI(k1,:)];
    spectrum=spectrum+spectrumI; % add hyperfine spectra
end

% inhomogeneous lw folding

Bhom=B-mean(B);
linie=exp(-(Bhom/lw).^2);
inhomlinie=linie/sum(linie);
finhom=fft(inhomlinie);

fspectrum=fft(spectrum).*finhom;
spectrum=real(fftshift(iffshift(fspectrum)));

```

### A.2.3. Simplexparameters2D

```

simplexruns=2000; % number of runs of the simplex routine
fitoptions=optimset('Display','Final','MaxIter',400); % display output of each iteration

```

```

fitstartvalues= [gangles thetaD phiD offset R J Tlfactor]; % start value for 1st simplex run
vub= [pi/2 pi/2 pi/2 pi/2 pi/2 0.2 2.5 1e7 2]; % upper boundary for fit parameters
vlb= [0 0 0 0 0 1.5 -1e7 0.5 ]; % lower boundary for fit parameters

lsize=10; % angle resolution in l rotation
lstep=pi/lsize;

wsize=length(thetaselect);

for k=1:lsize;

    theta((k-1)*wsize+1:k*wsize)=thetaselect'; % pack orientation parameters
    phi((k-1)*wsize+1:k*wsize)=phiselect';
    l((k-1)*wsize+1:k*wsize)=k*lstep*ones(wsize,1);
    int((k-1)*wsize+1:k*wsize)=intselect';
    kanalB((k-1)*wsize+1:k*wsize)=kanal';
    geffI((k-1)*wsize+1:k*wsize)=GeffI';

end

fitvalues=fitstartvalues; % for first loop

durchlauf=1; % counts number of simplex passes
bestsigma=1e20*ones(10,1); % initialize std vector
bestfitvalue=zeros(10,length(fitstartvalues)); % initialize bestfitvalue array (10
best results)

```

#### A.2.4. Echodecay2D

```

if SimFitauswahl=='S', % simulation of decay
    signalfit=simdecay2D(fitvalues,tau,TlS,geffI,GS,theta,phi,l,int,betae,Dipconst,B,kanalB,
    finhom);

elseif SimFitauswahl=='F', % doesn't work for HEdipolar2D!!!

end

```

#### A.2.5. Simdecay2D

```

function f=simdecay(fitvalues,tau,TlS,geffI,GS,theta,phi,l,int,betae,Dipconst,B,kanalB,finhom)

    % calculate dipolar coupling (A & B term) and echo decay function (Kev Salikov formula)

gangles=fitvalues(1:3);
thetaD=fitvalues(4);
phiD=fitvalues(5);
offset=fitvalues(6);
R=fitvalues(7);
J=fitvalues(8);
Tlfactor=fitvalues(9);

% parameters for the Kev Formula

tc=TlS/Tlfactor; % correlation time
km=1/tc; % corresponding rate
signal=zeros(length(B),length(tau));

GSM=Tensrot(gangles,GS); % rotate G-Tensor of S into I-spin axis system
DM=Dipolmol(thetaD, phiD); % calculate D tensor in I-spin axis system
for k=1:length(theta), % loop for all selected orientations of B0

    GSL=Tensrot([l(k),theta(k),phi(k)],GSM); % rotate GS in Lab system
    geffS(k)=sqrt(GSL(1,3)^2+GSL(2,3)^2+GSL(3,3)^2);
    wxz=GSL(1,3)*betae*B(kanalB(k));
    wyz=GSL(2,3)*betae*B(kanalB(k));
    wzz=GSL(3,3)*betae*B(kanalB(k));

    DL=Tensrot([l(k),theta(k),phi(k)],DM); % rotate Dipolar tensor in Lab system

```

```

Dxz=DL(1,3)*geffS(k)*geffI(k)*Dipconst;
Dyz=DL(2,3)*geffS(k)*geffI(k)*Dipconst;
Dzz=DL(3,3)*geffS(k)*geffI(k)*Dipconst;

dxz=Dxz/R^3;
dyz=Dyz/R^3;
dzz=Dzz/R^3;

Dm=((wzz+dzz/2+J)^2 +(wxz+dxz/2)^2 +(wyz+dyz/2)^2)^(1/2) - ((wzz-dzz/2-J)^2 +(wxz-dxz/2)^2
+(wyz-dyz/2)^2)^(1/2);
Dm=Dm*pi; % half dipolar splitting in rad s-1
intm=int(k);

rm=sqrt(km^2-Dm^2);

% Kev Salikov Formula

signal(kanalB(k),:)=signal(kanalB(k),:)+(1/rm^2*(km/2*(km+rm)*exp(-2*(km-
rm)*tau)+(km-rm)*exp(-2*(km+rm)*tau))-Dm^2*exp(-2*km*tau))*intm);

end

for kl=1:length(tau), % convolute with inhomogeneous line
    fsig=fft(signal(:,kl)).*finhom';
    signal(:,kl)=real(fftshift(ifft(fsig)));
end

signal=signal/max(max(signal)); % normalize signal

signal=(signal+offset)/(1+offset); % add offset and renormalize

f=signal;

```



### A.3. Staddiprelax

```

% new program for dipolar relaxation of statistical distributed spins
% with strong g-anisotropy of one spin species

% constants

Dipconst=1.298e7;           % constant for dipolare splitting from Gunnar
geff2=2;                   % second spin isotropic assumed
betae=1.39961e6;          % electronic beta factor Hz/G
gammae=2.8e6;              % electronic gamma factor for free electron spin

% experimental parameters

B0=180e9;
taustart=200e-9;          % tau start value
taustep=10e-9;            % tau step value
tausize=1000;             % size of tau vector
tau=taustart:taustep:(tausize-1)*taustep+taustart;           % tau vector

% spin operators

Iz=spinmatrix(1/2,'Sz');
Ip=spinmatrix(1/2,'Sp');
In=spinmatrix(1/2,'Sn');
Eins=spinmatrix(1/2,'ES');
Ix=spinmatrix(1/2,'Sx');
Iy=spinmatrix(1/2,'Sy');

% box parameters and concentrations

Xbox=60;                   % length of box in nm
Nfc=750;                   % concentration of fast relaxing spins in  $\mu\text{M}$ 
Nfnm=(6e26*Nfc/1e6/1e27); % Number of spins per  $\text{nm}^3$ 
Nf=round(Nfnm*Xbox^3);     % Number of spins in box
Rf=2;                      % radius of fast relaxing spin in nm

Nsc=750;                   % concentration of slow relaxing spins in  $\mu\text{M}$ 
Nsnm=(6e26*Nsc/1e6/1e27); % Number of spins per  $\text{nm}^3$ 
Ns=round(Nsnm*Xbox^3);    % Number of spins in box
Rs=2;                      % Radius of slow relaxing spin

% spin parameters and other parameters

Tlf=4000e-9;              % Tlf
km=1/Tlf;                 % flip rate
Rmin=Rs;                  % minimum R for calculation
Rmax=17;                  % maximum R for exact calculation

gx=1;
gy=2;
gz=3;
G1=[gx 0 0; 0 gy 0; 0 0 gz];

kstat=2000;               % number of statistical ensembles of spin distributions

% initialize variables

signal=zeros(1,length(tau)); % actual simulation echo decay signal
sigfar=zeros(1,length(tau));
sigtot=zeros(1,length(tau));
Nspos=zeros(3,Ns);
Nfpos=zeros(3,Nf);

[th, ph]=kugel(20);

for k1=1:length(th),

    GS1=rotfield(ph(k1)+pi/2,th(k1),G1); % molecule rotated
    geff1=abs(diff(real(eig(GS1(1,3)*Ix+GS1(2,3)*Iy+GS1(3,3)*Iz))));
    Rfar=Tlf*Nfnm*(pi*Dipconst*geff1*geff2/Rmax^3)^2;
    sigfar=sigfar+exp(-2*tau*Rfar);

end

sigfar=sigfar/length(th); % normalize echodecay for far apart spins

plot(2*tau,sigfar);

```

```

title(['decay for spins further than', num2str(Rmax)]);
drawnow;

for k1=1:kstat, % loop for statistical ensembles

    for k3=2:Ns, % loop for placing the slow relaxing spins (first is in center)
        accept=1;
        while accept==1,
            Nspos(:,k3)=rand(3,1)*Xbox-Xbox/2; % random position for slow spin
            distpos=Nspos(:,1:k3-1)-Nspos(:,k3)*ones(1,k3-1); % center around new spin
            Rdist=sqrt(sum(distpos.*distpos)); % distances to new one
            if min(Rdist)>2*Rs, accept=0; end % accept=0 for allowed position
        end
    end

    for k3=1:Nf, % loop for placing the fast relaxing spins (first is in center)
        accept=1;
        while accept==1,
            Nfpos(:,k3)=rand(3,1)*Xbox-Xbox/2; % random position for slow spin
            distpos1=Nspos-Nfpos(:,k3)*ones(1,Ns); % center slow spins around new spin
            Rdist1=sqrt(sum(distpos1.*distpos1)); % distances to slow spins
            if k3 > 1,
                distpos2=Nfpos(:,1:k3-1)-Nfpos(:,k3)*ones(1,k3-1); % center fast spins
                % around new spin
                Rdist2=sqrt(sum(distpos2.*distpos2)); % distances to other fast spins
            else
                Rdist2=3*Rf;
            end

            if (min(Rdist1)>(Rs+Rf) & min(Rdist2)>2*Rf), accept=0; end % accept=0 for
                % allowed position

        end
        R(k3)=norm(Nfpos(:,k3));
        cthdip(k3)=Nfpos(3,k3)/R(k3); % calculate cos(theta) dipolar
        sthdip(k3)=sqrt(1-(cthdip(k3))^2); % calculate sin(theta) dipolar
        if sthdip~=0,
            phdip(k3)=acos(Nfpos(1,k3)/sthdip(k3));
        else
            phdip(k3)=0;
        end
    end

    Nindex=find(R<Rmax & R>Rmin); % select the molecules in sphere

    if length(Nindex)>0,
        R=R(Nindex);
        cthdip=cthdip(Nindex); % contract the angles
        sthdip=sthdip(Nindex);
        phdip=phdip(Nindex);
    else
        D=[];
    end

    sig=ones(1,length(tau)); % starting echo decay for this loop

    for k2=1:length(Nindex),

        % dipolar splitting terms
        A=(1-3*cthdip(k2)^2)*kron(Iz,Iz);
        B=-(1-3*cthdip(k2)^2)/4*(kron(Ip,In)+kron(In,Ip));
        C=-3/2*sthdip(k2)*cthdip(k2)*exp(-i*phdip(k2))*(kron(Ip,Iz)+kron(Iz,Ip));
        D=-3/2*sthdip(k2)*cthdip(k2)*exp(i*phdip(k2))*(kron(In,Iz)+kron(Iz,In));
        E=-3/4*sthdip(k2)^2*exp(-2*i*phdip(k2))*kron(Ip,Ip);
        F=-3/4*sthdip(k2)^2*exp(2*i*phdip(k2))*kron(In,In);

        % choose arbitrary orientation of G-tensor of spin 1
        GS1=roten(rand(3,1)*pi,G1);

        geff1=abs(diff(real(eig(GS1(1,3)*Ix+GS1(2,3)*Iy+GS1(3,3)*Iz))));

        Dconst=pi*Dipconst*geff1*geff2/R(k2)^3; % effective dipolar splitting
        HD=(A+B+C+D+E+F)*Dconst; % dipolar Hamiltonian
        HZ=betae*B0*(GS1(1,3)*kron(Ix,Eins)+GS1(2,3)*kron(Iy,Eins)+GS1(3,3)*kron(Iz,Eins)+geff1*
        kron(Eins,Iz));

        H=HD+HZ;
        ew=sort(real(eig(H)));
    end
end

```

```

    Dm=ew(1)+ew(4)-ew(2)-ew(3); % dipolar splitting

    % calculate dipolar relaxation by Kev formula for all the coupled fast spins

    rm=sqrt(km^2-Dm^2);
    sigk=(1/rm^2*(km/2*((km+rm)*exp(-2*(km-rm)*tau)+(km-rm)*exp(-2*(km+rm)*tau))-
Dm^2*exp(-2*km*tau)));
    sig=sig.*sigk;
    end

    sig=sig/sig(1); % normalize signal for this loop to 1;

    signal=signal+sig; % add this loop signal to overall signal
    sigtot=sigal.*sigfar; % relaxation from spins outside Rmax
    sigtot=signal/signal(1); % normalize

    plot(2*tau, sigtot);
    title(num2str(k1));
    drawnow;
end

```

### A.3.1. Spinmatrix

```

function SM = spinmatrix(S,Op)
% S : Spinquantumnumber Op : Spinoperator ( ES, Sq, Sx, Sy, Sz, Sp, Sn ,T )

switch Op

case 'ES'
    nz=ones(1,2*S+1); % helpvector of length S
    SM=diag(nz,0); % S-Spinspace-matrix

case 'Sq'
    nz=ones(1,2*S+1); % helpvector of length S
    SM=S*(S+1)*diag(nz,0); % S-square Matrix

case 'Sz'
    nz=S:-1:-S;
    SM=diag(nz,0); % Sz-Spinmatrix for Spin S

case 'Sx'
    nz=zeros(1,2*S);
    for k=1:2*S,
        nz(k)=sqrt((2*S+1-k)*k);
    end;
    Sx1=diag(nz,1);
    Sx2=diag(nz,-1);
    SM=1/2*(Sx1+Sx2); % Sx-Spinmatrix for Spin S

case 'Sy'
    nz=zeros(1,2*S);
    for k=1:2*S,
        nz(k)=sqrt((2*S+1-k)*k);
    end;
    Sx1=diag(nz,1);
    Sx2=diag(nz,-1);
    SM=1/2*(Sx1*(-i)+Sx2*i); % Sy Spinmatrix for Spin S

case 'Sp'
    nz=zeros(1,2*S);
    for k=1:2*S,
        nz(k)=sqrt((2*S+1-k)*k);
    end;
    SM=diag(nz,1); % S+ Spinmatrix für Spin S

case 'Sn'
    nz=zeros(1,2*S);
    for k=1:2*S,
        nz(k)=sqrt((2*S+1-k)*k);
    end;
    SM=diag(nz,-1); % S- Spinmatrix for Spin S

case 'T'
    nz=ones(1,2*S);

```

```

    Sx1=diag(nz,1);
    Sx2=diag(nz,-1);
    SM=(Sx1+Sx2);           % Sx-Spinmatrix for Spin S
end;

```

### A.3.2. Rotfield

```

function M = rotfield(phi,theta,M),

    D= drehmat(phi,theta);      % rotation matrix from MAS to Labframe
    M=inv(D) * M * (D);        % A(lab)

```

#### A.3.2.1. Drehmat

```

function D=drehmat(phi,theta);
D(1,1)=cos(phi);
D(2,1)=sin(phi);
D(3,1)=0;
D(1,2)=-sin(phi)*cos(theta);
D(2,2)=cos(phi)*cos(theta);
D(3,2)=sin(theta);
D(1,3)=sin(theta)*sin(phi);
D(2,3)=-sin(theta)*cos(phi);
D(3,3)=cos(theta);

```

### A.3.3. Rottensor

```

function M= rottensor(Euler,M),

    D= rotmat(Euler);          % rotation matrix from MAS to Labframe
    M=inv(D) * M * D;         % A(lab)

```

#### A.3.3.1. Rotmat

```

% euler angle rotation matrix

function D = rotmat(Eulerangles)
a=Eulerangles(1);
b=Eulerangles(2);
c=Eulerangles(3);

D(1,1)=cos(c)*cos(a)-cos(b)*sin(a)*sin(c);
D(1,2)=-sin(c)*cos(a)-cos(b)*sin(a)*cos(c);
D(1,3)=sin(b)*sin(a);
D(2,1)=cos(c)*sin(a)+cos(b)*cos(a)*sin(c);
D(2,2)=-sin(c)*sin(a)+cos(b)*cos(a)*cos(c);
D(2,3)=-sin(b)*cos(a);
D(3,1)=sin(b)*sin(c);
D(3,2)=sin(b)*cos(c);
D(3,3)=cos(b);

```



## Appendix B - The IR Experiment at G-band Frequency

The G-band spectrometer has only one excitation channel, so that phase-cycling to eliminate unwanted echoes is not feasible. For this reason, in the IR experiment  $T$  has to be chosen much larger than  $\tau$ , as clarified by figure AB.1.

Because there were quite significant baseline drifts during an experiment, a background subtraction was always performed in the pulsed G-band experiments. Together with the integration window, a background integration window was determined at the beginning of the experiment. This is shown in figure AB.1 by the grey vertical lines. For the IR experiment the background integration window was placed directly before the pulses of the detection sequence, so that no problems with unwanted echoes would occur.

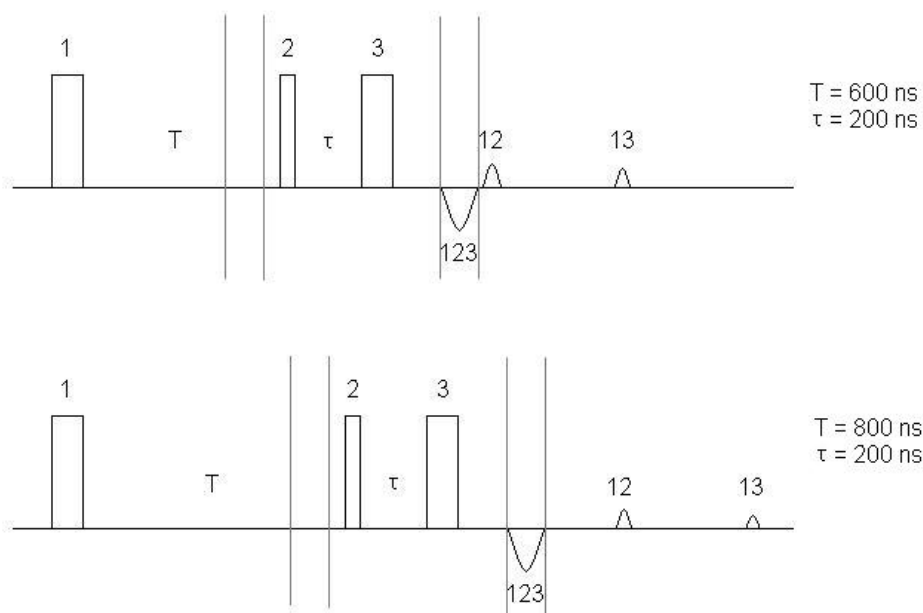


*Figure AB.1. The IR sequence as performed on our pulse G-band EPR spectrometer. The pulses are numbered, and the corresponding echoes are given by the numbers of the pulses that created them. The gray vertical lines represent the integration window (around the echo) and the window of background subtraction (before pulse 2). The integration windows were kept at a fixed distance from pulses 2 and 3 while  $T$  was stepped. The echoes appear at:  $T+\tau$  (echo 123),  $2T$  (echo 12) and  $2(T+\tau)$  (echo 13).*



## Literature

- Abragam, A. Principles of Nuclear Magnetism. New York, Clarendon Press Oxford (1961)
- Beinert, H. *Eur. J. Biochem.* **245**: 521 (1997)
- Beinert, H., Griffiths, D. E., Wharton, D. C. Sands, R. H. *J. Biol. Chem.* **237**: 2337 (1962)
- Berliner, L. J., Eaton, S. S. Eaton, G. R. Distance Measurements in Biological Systems by EPR. New York, Kluwer Academic/Plenum Publishers (2000)
- Bertini, I., Cavallaro, G. Rosato, A. *J. Biol. Inorg. Chem.* **10**: 613 (2005)
- Bickar, D., Bonaventura, C. Bonaventura, J. *J. Biol. Chem.* **259**: 10777 (1984)
- Blackburn, N. J., Barr, M. J., Woodruff, W. H., Oost, J. v. d. Vries, S. d. *Biochemistry* **33**: 10401 (1994)
- Bloembergen, N., Purcell, E. M. Pound, R. V. *Phys. Rev.* **73**: 679 (1948)
- Bloembergen, N., Shapiro, S., Pershan, P. S. Artman, J. O. *Phys. Rev.* **114**: 445 (1959)
- Bode, B. Personal communication to the author, May 2006.
- Brudvig, G. W., Blair, D. F. Chan, S. I. *J. Biol. Chem.* **259**: 11001 (1984)
- Brüggmann, O. (2003). Aufbau eines cw- / Puls-EPR Spektrometers bei 180 GHz. Fachbereich Chemische und Pharmazeutische Wissenschaften. Frankfurt am Main, Goethe Universität Frankfurt: 133.
- Brzezinski, P. Larsson, G. *Biochim. Biophys. Acta* **1605**: 1 (2003)
- Budker, V., Du, J.-L., Seiter, M., Eaton, G. R. Eaton, S. S. *Biophysical Journal* **68**: 2531 (1995)
- Bushnell, G. W., Louie, G. V. Brayer, G. D. *J. Mol. Biol.* **214**: 585 (1990)
- Carrington, A. McLachlan, A. D. Introduction to Magnetic Resonance, Harper&Row, John Weatherhill Inc. (1967)
- Crowley, P. Carrondo, M. A. *Proteins* **55**: 603 (2004)
- Cunha, C. A., Romao, M. J., Sadegi, S. J., Valetti, F., Gilardi, G. Soares, C. M. *J. Biol. Inorg. Chem.* **4**: 360 (1999)
- Cunningham, K. L., McNett, K. M., Pierce, R. A., Davis, K. A., Harris, H. H., Falck, D. M. McMillin, D. *J. Inorg. Chem.* **36**: 608 (1997)
- Davids, D. A. Wagner, P. E. *Phys. Rev. Lett.* **12**: 141 (1964)
- Drosou, V., Malatesta, F. Ludwig, B. *Eur. J. Biochem.* **269**: 2980 (2002a)
- Drosou, V., Reincke, B., Schneider, M. Ludwig, B. *Biochemistry* **41**: 10629 (2002b)
- Eaton, S. S., Harbridge, J., Rinard, G. A., Eaton, G. R. Weber, R. T. *Appl. Magn. Res.* **20**: 151 (2001)
- Ernst, R. R. Anderson, W. A. *Rev. Sci. Inst.* **37**: 93 (1966)
- Ernst, R. R., Bodenhausen, G. Wokaun, A. Principles of Nuclear Magnetic Resonance in One and Two Dimensions. New York, Clarendon Press Oxford (1987)
- Faxén, K., Gilderson, G., Ädelroth, P. Brzezinski, P. *Nature* **437**: 286 (2005)
- Fielding, A. J., Fox, S., Millhauser, G. L., Chattopadhyay, M., Kroneck, P. M. H., Fritz, G., Eaton, G. R. Eaton, S. S. *J. Mag. Res.* **179**: 92 (2006)
- Flöck, D. Helms, V. *Proteins* **47**: 75 (2002)
- Flöck, D. Helms, V. *Biophys. J.* **87**: 65 (2004)
- Goodman, G. Leigh, J. S. *Biochemistry* **24**: 2310 (1984)



- Gray, H. B. Winkler, J. R. *Quart. Rev. Biophys.* **36**: 341 (2003)
- Greenaway, F. T., Chan, S. H. P. Vincow, G. *Biochim. Biophys. Acta* **490**: 62 (1977)
- Grimaldi, S. (2002). Multidimensional Electron Paramagnetic Resonance Spectroscopy on Protein Bound Semiquinones. J.W. Goethe University. Frankfurt am Main, J.W. Goethe University.
- Grinberg, O. Y. Berliner, L. J. Very High Frequency (VHF) ESR/EPR, Kluwer Academic/Plenum Publishers (2004)
- Harrenga, A., Reincke, B., Rüterjans, H., Ludwig, B. Michel, H. *J. Mol. Biol.* **295**: 667 (2000)
- Hertel, M. M., Denysenkov, V. P., Bennati, M. Prisner, T. F. *Magn. Res. Chem.* **43**: 248 (2005)
- Hosler, J. P., Ferguson-Miller, S. Mills, D. A. *Annu. Rev. Biochem.* **75**: 165 (2006)
- Iwata, S., Ostermeier, C., Ludwig, B. Michel, H. *Nature* **376**: 660 (1995)
- Janzon, J. Personal communication to B.Ludwig, 2006.
- Jeschke, G. *Macromol. Rapid Commun.* **23**: 227 (2002)
- Jung, C., Lenzian, F., Schünemann, V., Richter, M., Böttger, L. H., Trautwein, A. X., Contzen, J., Galander, M., Ghosh, D. K. Barra, A.-L. *Magn. Reson. Chem.* **43**: 84 (2005)
- Käss, H., MacMillan, F., Ludwig, B. Prisner, T. F. *J. Phys. Chem. B* **104**: 5362 (2000)
- Kirilina, E. P., Grigoryev, I. A. Dzuba, S. A. *Journal of Chemical Physics* **121**: 12465 (2004)
- Kirilina, E. P., Prisner, T. F., Bennati, M., Endeward, B., Dzuba, S. A., Fuchs, M., Möbius, K. Schnegg, A. *Magn. Res. Chem.* **43**: 119 (2005)
- Kispert, L. D., Bowman, M. K., Norris, J. R. Brown, M. S. *J. Chem. Phys.* **76**: 26 (1982)
- Klauder, J. R. Anderson, P. W. *Phys. Rev.* **125**: 912 (1962)
- Kroneck, P. M. H., Antholine, W. A., Riester, J. Zumft, W. G. *FEBS Letters* **242**: 70 (1988)
- Kulik, L. V. Dzuba, S. A. *J. Struct. Chem.* **45**: 298 (2004)
- Kulik, L. V., Dzuba, S. A., Grigoryev, I. A. Tsvetkov, Y. D. *Chem. Phys. Lett.* **343**: 315 (2001)
- Kulik, L. V., Paschenko, S. V. Dzuba, S. A. *J. Magn. Res.* **159**: 237 (2002)
- Lakshmi, K. V., Poluektov, O. G., Reifler, M. J., Wagner, A. M., Thurnauer, M. J. Brudvig, G. W. *JACS* **125**: 5005 (2003)
- Lakshmi, K. V., Reifler, M. J., Brudvig, G. W., Poluektov, O. G., Wagner, A. M. Thurnauer, M. J. *J. Phys. Chem. B* **104**: 10445 (2000)
- Lange, C. Hunte, C. *Proc. Natl. Acad. Sci. USA* **99**: 2800 (2002)
- Lappalainen, P., Aasa, R., Malmström, B. G. Saraste, M. *J. Biol. Chem.* **268**: 26416 (1993)
- Larsen, R. G. Singel, D. J. *J. Chem. Phys.* **98**: 5134 (1992)
- Likhtenshtein, G. I. (2000). Depth of immersion of paramagnetic centers in biological systems. Biological Magnetic Resonance. Berliner, L. J., Eaton, S. S. Eaton, G. R. New York, Kluwer Academic/Plenum Publishers. **19**.
- Lyubenova, S. (2006). CW and Pulsed EPR Studies on Metalloproteins and Protein-Protein Complexes. Physical and Theoretical Chemistry. Frankfurt am Main, Goethe University Frankfurt.
- Lyubenova, S., Siddiqui, M. K., Penning de Vries, M. J. M., Ludwig, B. Prisner, T. F. Manuscript in preparation.
- MacMillan, F., Kannt, A., Behr, J., Prisner, T. F. Michel, H. *Biochemistry* **38**: 9179 (1999)
- Mailer, C. Taylor, C. P. *Can. J. Biochem.* **50**: 1048 (1972)

- Maly, T. (2004). New pulsed EPR methods for separating overlapping EPR signals and their application to mitochondrial complex I. Physical and Theoretical Chemistry. Frankfurt am Main, Goethe University Frankfurt: 234.
- Maneg, O., Ludwig, B. Malatesta, F. *J. Biol. Chem.* **278**: 46734 (2003)
- Maneg, O., Malatesta, F., Ludwig, B. Drosou, V. *Biochim. Biophys. Acta* **1655**: 274 (2004)
- Marcus, R. A. Sutin, N. *Biochim. Biophys. Acta* **811**: 265 (1985)
- Martin, R. E., Pannier, M., Diederich, F., Gramlich, V., Hubrich, M. Spiess, H. W. *Angew. Chem.* **110**: 2994 (1998)
- Mattila, K. Haltia, T. *Proteins* **59**: 708 (2005)
- Mchaourab, H. S., Pfenninger, S., Antholine, W. A., Felix, C. C., Hyde, J. S. Kroneck, P. M. H. *Biophys. J.* **64**: 1576 (1993)
- Messerschmidt, A., Huber, R., Poulos, T. Wieghardt, K. Handbook of Metalloproteins, John Wiley & Sons Ltd (2001)
- Milov, A. D., Ponomarev, A. B. Tsvetkov, Y. D. *Chem. Phys. Lett.* **110**: 67 (1984)
- Muresanu, L., Pristovsek, P., Löhr, F., Maneg, O., Mukrasch, M. D., Rüterjans, H., Ludwig, B. Lücke, C. *J. Biol. Chem.* **281**: 14503 (2006)
- Murphy, J. *Phys. Rev.* **145**: 241 (1966)
- Narr, E., Godt, A. Jeschke, G. *Angewandte Chemie Int. Ed.* **41**: 3907 (2002)
- Neese, F., Zumft, W. G., Antholine, W. E. Kroneck, P. M. H. *J. Am. Chem. Soc.* **118**: 8692 (1996)
- Nicholls, D. G. Ferguson, S. J. Bioenergetics 3, Academic Press (2002)
- Nocek, J. M., Zhou, J. S., De Forest, S., Priyadarshy, S., Beratan, D. N., Onuchic, J. N. Hoffman, B. *M. Chem. Rev.* **96**: 2459 (1996)
- Northrup, S. H., Boles, J. O. Reynolds, J. C. L. *Science* **241**: 67 (1988)
- Orbach, R. *Proc. Royal Soc. London A* **264**: 458 (1961)
- Orbach, R. Stapleton, H. J. (1972). Electron spin-lattice relaxation. Electron Paramagnetic Resonance. Geschwindt, S. New York, Plenum: 121.
- Pake, G. E. *J. Chem. Phys.* **16**: 327 (1948)
- Pelletier, H. Kraut, J. *Science* **258**: 1748 (1992)
- Pezeshk, A., Torres, J., Wilson, M. T. Symons, M. C. R. *J. Inorg. Biochem.* **83**: 115 (2001)
- Pfenninger, S., Antholine, W. A., Barr, M. E., Hyde, J. S., Kroneck, P. M. H. Zumft, W. G. *Biophysical Journal* **69**: 2761 (1995)
- Plackmeyer, J. Schiemann, O. Manuscript in preparation.
- Poole, C. P. J. Farach, H. A. Relaxation in Magnetic Resonance: Dielectric and Mössbauer Applications. New York/ London, Academic Press (1971)
- Prisner, T. *Adv. Magn. Opt. Res.* **20**: 245 (1997)
- Prisner, T. F., Rohrer, M. MacMillan, F. *Annu. Rev. Phys. Chem.* **52**: 279 (2001)
- Prudêncio, M. Ubbink, M. *J. Mol. Recogn.* **17**: 524 (2004)
- Randall, D. W., Gamelin, D. R., LaCroix, L. B. Solomon, E. I. *J. Biol. Inorg. Chem.* **5**: 16 (2000)
- Reincke, B., Pérez, C., Pristovsek, P., Lücke, C., Ludwig, C., Löhr, F., Rogov, V. V., Ludwig, B. Rüterjans, H. *Biochemistry* **40**: 12312 (2001)
- Reincke, B., Thöny-Meyer, L., Dannehl, C., Odenwald, A., Aidim, M., Witt, H., Rüterjans, H. Ludwig, B. *Biochim. Biophys. Acta* **1411**: 114 (1999)
- Rich, P. R. *Biochem. Soc. Trans.* **31**: 1095 (2003)

- Richter, O. M. Ludwig, B. *Rev. Physiol. Biochem. Pharm.* **147**: 47 (2003)
- Roberts, V. A. Pique, M. E. *J. Biol. Chem.* **274**: 38051 (1999)
- Rohrer, M., Brüggmann, O., Kinzer, B. Prisner, T. F. *Applied Magnetic Resonance* **21**: 257 (2001)
- Salikhov, K. M., Dzuba, S. A. Raitsimring, A. M. *J. Magn. Res.* **42**: 255 (1981)
- Saxena, S. Freed, J. H. *Chem. Phys. Lett.* **251**: 102 (1996)
- Saxena, S. Freed, J. H. *J. Chem. Phys.* **107**: 1317 (1997)
- Sazanov, L. Hinchliffe, P. *Science* **311**: 1430 (2006)
- Schägger, H. *Biochim. Biophys. Acta* **1555**: 154 (2002)
- Schnegg, A., Fuhs, M., Rohrer, M., Lubitz, W., Prisner, T. F. Möbius, K. *J. Phys. Chem. B* **106**: 9454 (2002)
- Scholes, C. P., Janakiraman, R., Taylor, H. King, T. E. *Biophys. J.* **45**: 1027 (1984)
- Schultz, B. E. Chan, S. I. *Annu. Rev. Biomol. Struct.* **30**: 23 (2001)
- Schweiger, A. Jeschke, G. Principles of Pulse Electron Paramagnetic Resonance. New York, Oxford (2001)
- Seiter, M., Budker, V., Du, J.-L., Eaton, G. R. Eaton, S. S. *Inorg. Chim. Acta* **273**: 354 (1998)
- Siddiqui, M. K. (2006). Association of Bacterial Respiratory Complexes. Biochemistry. Frankfurt am Main, Goethe University Frankfurt.
- Slutter, C. E., Gromov, I., Epel, B., Pecht, I., Richards, J. H. Goldfarb, D. *J. Am. Chem. Soc.* **123**: 5325 (2001)
- Stapleton, H. J., Allen, J. P., Flynn, C. P., Stinson, D. G. Kurtz, S. R. *Phys. Rev. Lett.* **45**: 1456 (1980)
- Stryer, L. Biochemistry. New York, W.H. Freeman and Company (1995)
- Tweedle, M. F., Wilson, L. J., García-Iñiguez, L., Babcock, G. T. Palmer, G. *J. Biol. Chem.* **253**: 8065 (1978)
- Ubbink, M., Ejdebäck, M., Karlsson, B. G. Bendall, D. S. *Structure* **6**: 323 (1998)
- Un, S., Brunel, L.-C., Brill, T. M., Zimmermann, J.-L. Rutherford, A. W. *Proc. Natl. Acad. Sci. USA* **91**: 5262 (1994)
- Vanneste, W. H. *Biochemistry* **5**: 838 (1966)
- Walker, F. A. *Coord. Chem. Rev.* **185-186**: 471 (1999)
- Weber, A. Personal communication.
- Weber, A., Schiemann, O., Bode, B. Prisner, T. F. *J. Magn. Res.* **157**: 277 (2002)
- Wendeloski, J. J., Matthew, J. B., Weber, P. C. Salemme, F. R. *Science* **238**: 794 (1987)
- Wienk, H., Maneg, O., Lücke, C., Pristovsek, P., Löhr, F., Ludwig, B. Rüterjans, H. *Biochemistry* **42**: 6005 (2003)
- Wikström, M. *Biochim. Biophys. Acta* **1655**: 241 (2004)
- Witt, H., Malatesta, F., Nicoletti, F., Brunori, M. Ludwig, B. *Eur. J. Biochem.* **251**: 367 (1998a)
- Witt, H., Malatesta, F., Nicoletti, F., Brunori, M. Ludwig, B. *J. Biol. Chem.* **273**: 5132 (1998b)
- Yoshikawa, S., Shinzawa-Itoh, K., Nakashima, R., Yaono, R., Yamashita, E., Inoue, N., Yao, M., Fei, M. J., Peters Libeu, C., Mizushima, T., Yamaguchi, H., Tomizaki, T. Tsukihara, T. *Science* **280**: 1723 (1998)
- Zecevic, A., Eaton, G. R., Eaton, S. S. Lindgren, M. *Mol. Phys.* **95**: 1255 (1998)



## Acknowledgments

I owe many thanks to my supervisor, Professor Thomas Prisner, for his continuous support and the many long, interesting discussions we had. I want to thank Sevdalina Lyubenova, with whom I worked together for most of my thesis, and who talked sense to me when I was in despair. Khalid Siddiqui was a great help by always providing the protein samples we needed, when we needed them, and his supervisor Professor Bernd Ludwig clarified many a biochemical problem. Jörn Plackmeyer made the metal-nitroxide samples and was always there with more material or advice. Thanks to the EPR groups in Antwerp, and especially Evi Vinck, who helped me with the W-band measurements that, unfortunately, didn't make it into the thesis.

Financial support from the Deutsche Forschungsgemeinschaft (SFB 472), the Center for Biomagnetic Resonance (BMRZ) in Frankfurt, and the Hermann Willkomm Stiftung is greatly acknowledged.

A big thank you, too, to all of you in AK Prisner who contributed in various ways to this thesis: by answering my questions both stupid and less stupid, discussions during group seminars or at other times, technical assistance during measurements, proofreading the thesis (Burkhard, Bela, Adrian, Dominik), and by generally creating an atmosphere worth working in.

Special thanks goes to the friends who were in one way or another involved with my thesis work: Bart v.O., Zhenya K., Alexander, Martin (for fxfilter and the eye in my spaghetti), Zhenya P., Florin, Iulia and Aránzazu I wish to thank for their tours of Antwerp and Madrid, respectively.

For the "corpore sano" part: thanks to Kurt Stenzel and his troupe of athletes, for what would a Sunday morning be without a two-hour run? Thanks especially to Heike, who corrected my German abstract.

Living in Frankfurt would not have been possible without the generous donation of furniture by several family members (on the condition of being mentioned in my Ph.D. thesis): Ron, Raymond and Beppie. As Salman Rushdie said about the Indian theory of relativity: "It's all about the relatives".

Lots of thanks to my "little" brother Bart for correcting my English, and for lessons about what one can not and cannot do.

I want to thank all of my family –Frits, Cobie, Bart, as well as Dennis, Quirijn and Karin, for their continuous support and belief in me. Wouldn't Freek have been proud of his little sister?



## Summary

An application of EPR spectroscopy that is becoming increasingly important is the measurement of distances between electron spins. Several EPR methods have been developed for this purpose, all based on measuring the dipolar coupling between two spins. Due to the specific nature of the sample, we applied dipolar relaxation enhancement measurements to study the geometry of a protein-protein complex. The paramagnetic centers in question had EPR spectra that were too broad and had such short relaxation time that they could not be studied using the more straightforward PELDOR technique.

EPR spectral resolution can be increased appreciably by measuring at a frequency higher than conventional X-band (9 GHz) frequency. The spectra of many paramagnetic species can only be resolved at frequencies higher than 90 GHz. For accurate measurement of the orientation of the vector between two dipolar coupled spins with respect to the  $g$ -tensors of the spins, high spectral resolution is required. We therefore performed our EPR measurements at G-band (180 GHz) frequency.

Dipolar relaxation measurements were applied to study the complex that is formed by the two electron-transfer proteins cytochrome  $c$  and cytochrome  $c$  oxidase (CcO) from the soil bacterium *Paracoccus denitrificans*. We were able to detect dipolar relaxation enhancement due to complex formation of soluble subunit II of *P.d.* CcO (CcO<sub>II</sub>) with two substrate cytochromes, which was practically absent in a mixture of CcO<sub>II</sub> with the negative control protein cytochrome  $c_1$ . This complex formation was characterized by a pronounced temperature dependence that could be simulated using a home-written computer program. The G-band EPR measurements could not be simulated with a single complex geometry. This provided evidence for the hypothesis that electron-transfer protein complexes are short-lived and highly dynamic; they do not seem to form one specific electron-transfer conformation, but rather move around on each other's binding surfaces and transfer an electron as soon as the distance between donor and acceptor is short enough.

As a test of our simulation program, we also applied dipolar relaxation measurements to specially synthesized organic molecules that contained a nitroxide radical and a metal center. The transverse relaxation of Cu<sup>2+</sup>-OEP-TPA was compared to the relaxation of Ni<sup>2+</sup>-OEP-TPA at temperatures between 20 and 120 K. In this temperature range, the nitroxide relaxation was enhanced due to the presence of Cu<sup>2+</sup>, but not by Ni<sup>2+</sup>. Similarly, relaxation enhancement was found in the nitroxide-Mn<sup>2+</sup> pair in Mn<sup>2+</sup>-terpyridine-TPA with respect to the terpyridine-TPA ligand. Due to the fast T<sub>2</sub> relaxation of the nitroxide radical at high temperatures, the measurements were all performed in the low-temperature regime where the T<sub>1</sub> relaxation rate of the metal ion was smaller than the dipolar coupling frequency. In this region, no structural information about the molecule can be deduced, since the dipolar relaxation enhancement is only determined by the T<sub>1</sub> of the metal ion.

The dipolar relaxation measurements we performed at high field indicated a difference in relaxation times between X-band and G-band frequencies. Extensive T<sub>1</sub>

measurements of different paramagnetic centers ( $\text{Cu}_A$ ,  $\text{Cu}^{2+}$ ) confirmed a strong dependence of  $T_1$  on magnetic field in the temperature range where the direct process is the dominating  $T_1$  relaxation process. This dependence is very strong (factor of  $10^3$  with respect to X-band), but does not follow the  $B_0^4$  dependence predicted in literature. The  $T_1$  relaxation of low-spin iron in cytochrome *c* at high magnetic field, estimated from dipolar relaxation data, is also in agreement with a larger contribution by the direct process (factor of  $10^4$ ).

Dipolar relaxation enhancement was found to be a technique that is useful for measuring distances between paramagnetic centers, but only for systems where several important conditions are met, such as: the system exists in one certain static geometry, and the relaxation rate of the fast-relaxing spin is faster than the dipolar coupling frequency within the accessible temperature range. Additionally, it is a great advantage for the analysis of dipolar relaxation data if the procedure of dividing the relaxation trace of the dipolar-coupled slow-relaxing spin by the relaxation trace of the slow-relaxing spin in absence of dipolar coupling can be applied.

Another useful application of dipolar relaxation enhancement measurements is the measurement of  $T_1$  relaxation of extremely fast-relaxing spins, or spins that are otherwise difficult to detect.





# Curriculum Vitae

## General

Name : Penning de Vries  
First names: Marloes Johanna Maria  
Nationality: Dutch  
Date of birth: March 26, 1980  
Place of birth: Wageningen, the Netherlands

## Education

High school:  
1992-1998 Scholengemeenschap Pantarijn, Wageningen, the Netherlands

University:  
1998-2001 BA Molecular Sciences Wageningen University, the Netherlands

Sep. 2001 - Feb. 2002 First master's thesis with the title: "The Use of ESR Spectral Parameters in Membrane Protein Research" at the Laboratory for Biophysics with Dr. M.A. Hemminga, Wageningen University, the Netherlands

Mar.-July 2002 Second master's thesis with the title: "High-Field EPR Studies of Quinone Spectral Properties" at the Service de Bioénergétique, with Dr. S. Un, CEA Saclay, France

Sep. 2002 MSc Degree in Molecular Sciences (Moleculaire Wetenschappen) at Wageningen University, the Netherlands

## Career

Sep.-Dec. 2002 Assistant in the practical course General and Physical Chemistry (Algemene en Fysische Chemie) at Wageningen University, the Netherlands

From Feb. 2003 PhD student in the Department for Chemical and Pharmaceutical Sciences with Prof. T.F. Prisner at the J.W. Goethe University Frankfurt am Main, Germany

From Feb. 2003 Assistant in the practical course General and Inorganic Chemistry for Scientists (Allgemeine und Anorganische Chemie für Naturwissenschaftler) at J.W. Goethe University Frankfurt am Main, Germany

### Publications

Oct. 2006 S. Lyubenova, M.K. Siddiqui, M.J.M. Penning de Vries, B. Ludwig, T.F. Prisner:  
"Protein-Protein Interactions Studied by EPR Relaxation Measurements: Cytochrome *c* and Cytochrome *c* Oxidase"  
*Submitted*

### Research Talks

June 30, 2005 „Measurement of dipolar relaxation enhancement at X- and G-Band frequencies to determine distances between proteins“ at the Specialized Colloque AMPERE, Leiden, the Netherlands

Sep. 27, 2005 „Binding of cytochrome *c* to cytochrome *c* oxidase: Distance measurements by pulsed EPR“ at the 27th Discussion Meeting of the GDCh Magnetic Resonance Division in Mainz, Germany

April 19, 2006 „Protein-protein interactions studied by EPR relaxation measurements: cytochrome *c* and cytochrome *c* oxidase“ as a progress report in DFG-SFB 472: Molecular Bioenergetics in Frankfurt am Main, Germany

### Research School

17-24 July, 2005 3rd European EPR Summer School in Wiesbaden, Germany

